CONTINUOUS CRYSTALLIZATION OF MULTICOMPONENT MATERIALS

Václav Svoboda

Department of Chemical and Process Engineering

Thesis submitted to the department of Chemical and Process Engineering at the University of Strathclyde in accordance with the requirements for the degree of Doctor of Philosophy.

December 2018

DECLARATION OF AUTHENTICITY AND AUTHOR'S RIGHTS

This thesis is the result of the author's original research. It has been composed by the author and has not been previously submitted for examination which has led to the award of a degree.

Signed:

Date:

ACKNOWLEDGMENTS

Firstly, I would like to thank my supervisor Prof. Jan Sefcik for all of his help and advice throughout this project along with his support and engagement in various collaborations. I would also like to thank my second supervisor Dr. Leo Lue, other members of the research group (Dr. John McGinty, Dr. Pól MacFhionnghaile, Dr. Okpeafoh Agimelen, Mairi Jaap), Bilal Ahmed, Dr. Cameron Brown, Dr. Iain Oswald, Dr. Lauren Connor and Prof. Joop ter Horst's research group (Andrew Dunn, Raghu Venkatramanan) for their contributions to this thesis and other work. Also, I would like to thank CMAC for providing a collaborative research environment, well-equipped facilities and many helpful experts, as well as the EPSRC for funding this work.

I very much appreciate both the opportunity to visit the group of Ass. Prof. Heidi Gruber-Woelfler at TU Graz, and the hospitality of the group during my time in Austria. Furthermore, the five-month industrial placement carried out at Eli Lilly in Indianapolis was a great experience and I would like to thank members of SMDD for all their support and making me feel part of the team.

Finally, I am grateful to my fellow DTC students and friends for their support during the last four years. My family, for providing me with the opportunity to study abroad, for their support before and during this thesis and their continuous encouragement. Thank you.

Parts of this thesis have been included in the following publications

1. Svoboda, V., MacFhionnghaile, P., McGinty, J., Connor, L.E., Oswald, I.D.H., Sefcik, J. Continuous Cocrystallization of Benzoic Acid and Isonicotinamide by Mixing-Induced Supersaturation: Exploring Opportunities between Reactive and Antisolvent Crystallization Concepts. Cryst. Growth Des. 17, 1902–1909 (2017).

2. Raza, S. A. Schacht, U., **Svoboda, V.**, Edwards, D.P., Florence, A.J., Pulham, C.R., Sefcik, J., Oswald, I.D.H. Rapid Continuous Antisolvent Crystallization of Multicomponent Systems. Cryst. Growth Des. 18, 210–218 (2018).

3. Svoboda, V., Venkatramanan, R., Jaap, M., Lue, L., ter Horst, J.T., Sefcik, J. Co-crystal Phase Diagram Measurement via Equilibration and Solution Addition. In preparation

Other Publications

4. MacFhionnghaile, P., **Svoboda, V.**, McGinty, J., Nordon, A. & Sefcik, J. Crystallization Diagram for Antisolvent Crystallization of Lactose: Using Design of Experiments To Investigate Continuous Mixing-Induced Supersaturation. Cryst. Growth Des. 17, 2611–2621 (2017).

5. Agimelen, O. S., **Svoboda, V.**, Ahmed, B., Cardona, J., Dziewierz, J., Brown, C.J., McGlone, T., Cleary, A., Tachtatzis, C., Michie, C., Florence, A.J., Andonovic, I., Mulholland, A.J., Sefcik, J. Multi-sensor inline measurements of crystal size and shape distributions during high shear wet milling of crystal slurries. Adv. Powder Technol. (2018). doi:10.1016/j.apt.2018.09.003

6. Dunn, A., **Svoboda, V.**, Sefick, J., ter Horst, J.T. Resolution Control in a Continuous Preferential Crystallization Process. In preparation

ABSTRACT

The challenges of developing continuous crystallization processes of multicomponent crystals are addressed within this thesis. Multicomponent crystals such as co-crystals and solid solutions, can be used to modify physical properties of active pharmaceuticals, agrochemicals and other materials. These can result in enhanced product properties such as higher solubility, faster dissolution, better stability or improved manufacturability in downstream processing through desirable morphology and better powder flowability. Continuous manufacturing is routinely used in many industries but is a new trend in the manufacture of pharmaceuticals driven by the potential to reduce plant footprint and intermediate inventory, improve yields, reduce lead time, implement real time monitoring and automation and make processes safer.

Compared to crystallization of single component crystals, additional component and solid phases introduce additional complexity in the phase diagram. Co-crystal phase diagram measurement in a series of solvents can be very time consuming compared to a solubility curve of a single component. A semi-empirical approach of modeling phase diagrams as well as new methods of measuring phase diagrams of multicomponent materials are presented to accelerate the time to obtain a phase diagram compared to traditional approaches. Transitions from small scale batch crystallization to continuous crystallization is also demonstrated here for co-crystals and solid solutions with high selectivity and reproducibility with respect to the solid phase produced.

TABLE OF CONTENTS

LIST OF FIGURES

LIST OF TABLES

CHAPTER 1

INTRODUCTION

1.1. CRYSTALLIZATION

Industrial crystallization is a common separation unit operation where pure crystalline solid is formed from solute molecules in liquid phase. Crystallization is used in the fine chemicals industry primarily for purification post synthesis. However, due to the importance of particle properties on product performance, this step can also be used for particle engineering purposes. For example, a process for crystallizing an API can be designed to control particle size and morphology to obtain the desired release profile in formulation or to improve filterability of the product slurry and powder flow.[1]

The driving force for crystallization from solution is supersaturation, which is related to the solubility and concentration of the solute.[2] This is represented on a phase diagram where the system moves from a liquid region to solid-liquid region. When concentration is higher than solubility, the solution becomes metastable and eventually crystals will nucleate and grow. Supersaturation can be generated in multiple ways: cooling, evaporation, addition of antisolvent, chemical reaction or any combination of these.

Many molecules have been shown to crystallize in multiple arrangements called polymorphs. While being identical chemically, the different crystal structure results in different physical properties of the solid phase. Solid state screening for potential solid phases is carried out thoroughly for all APIs as polymorph control is essential for delivering required product performance.[3,4] In crystallization, which polymorph nucleates is dependent on several factors. Ostwald's rule of stages describes the general tendency of the least stable polymorphs to crystallize first.[5] If left in suspension, the metastable polymorph will eventually

transform to the stable phase with the lowest solubility. This is called solvent mediated transformation. Along with impurity rejection and yield, controlling solid form is one of the main benchmarks of a crystallization process.

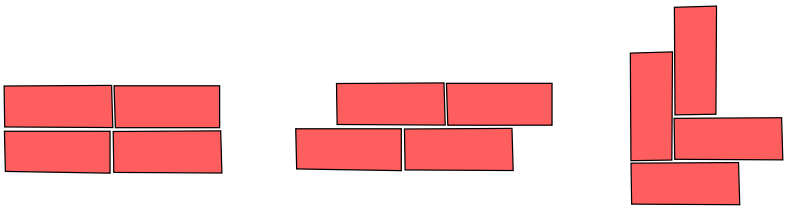

Figure 1.1. *Schematic of different arrangements of the same building block – polymorphs.*

Crystallizers can take many forms, but most are based on the classical stirred tank crystallizer in batch or continuous or plug flow crystallizers. When operated in continuous mode, stirred tank crystallizers are called MSMPRs (Mixed-Suspension Mixed-Product Removal).[6] They are often chained together in a cascade to reduce the concentration steps between stages and to approach plug flow-like residence time distribution. An example of a plug flow crystallizer is an oscillatory baffled crystallizer,[7] where oscillation of the fluid back and forth is used to decouple the effective flow rate through the crystallizer cross section from the residence time in the crystallizer. This is done in order to achieve long residence time for crystal growth while maintaining turbulent flow without requiring an extremely long crystallizer. In other cases, where nucleation driven crystallization is required, static mixers of various geometries have been used.[8]

1.2. MULTICOMPONENT CRYSTALS

Multicomponent crystalline systems have become more popular in recent years as a method of modifying physical properties of active pharmaceutical ingredients (APIs),[9,10] energetic materials[11,12] and other applications.[13] They are defined as crystalline materials consisting of multiple components in their lattice and include co-crystals, salts, solvates and solid solutions.[14] Unlike co-crystals and solvates, solid solutions can exist in a range of compositions showing miscibility in the solid phase. The majority of APIs are formulated as crystalline powders and the manufacturability and product performance can be influenced by their crystal structure, which may be modified by introducing a second component.[15] Crystal structure affects properties such as heat of fusion and melting point which in turn have a strong effect on the solubility and bioavailability in the formulated product. Crystal structure also has impact on particle morphology which influences product performance such as dissolution rate but also affects manufacturability through powder flow through unit operations and filtration performance. Introducing a new component which results in new solid phases, this means that the new phase diagram shape must be taken into consideration for crystallization process development.

Multicomponent crystal phase diagrams can have various shapes depending on the type of multicomponent crystal and if the stoichiometry is fixed. Figure 1.2 shows binary *T*-*x* phase diagrams for compounds A and B in three different scenarios: no solid-state interaction, formation of a co-crystal and formation of a fully miscible solid solution.

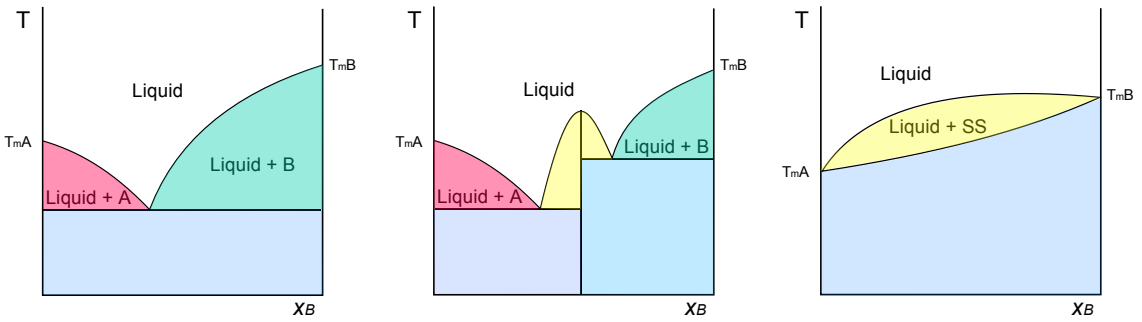

Figure 1.2. *Illustration of binary phase diagrams representing a mixture (left), a co-crystal (center) and solid solution (right) forming compounds.*

Figure 1.3 shows an illustration of a ternary phase diagram at constant temperature with two solutes A and B with a solvent. The phase diagram on the left represents a case where two components do not interact in the solid phase. The shape of the solubility lines will depend on the interaction of the solutes in liquid phase. In the illustration, the two solutes behave ideally and do not influence each other's solubilities, hence the solubility lines are straight.

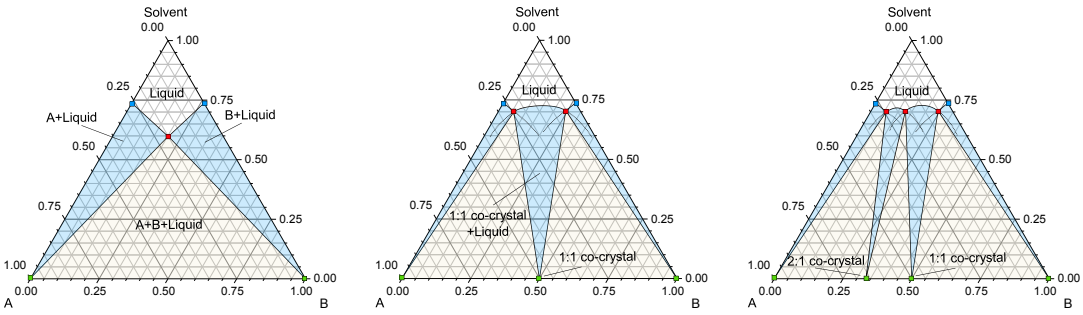

Figure 1.3. *Illustration of two solute and solvent phase diagram scenarios. No new solid phases (left), a 1:1 co-crystal (center) and 2:1 and 1:1 co-crystals (right).*

The middle phase diagram shows a scenario where a co-crystal phase in 1:1 ratio of A to B exists in equilibrium. The solubilities of components A and B are similar, and the co-crystal region is in the middle of the diagram. Therefore, the phase diagram is congruent. Dashed lines extend the solid-liquid lines past the

equilibrium regions. These show the solubility of their respective solid phases in metastable conditions. The rightmost phase diagram shows a scenario where co-crystals of 2:1 and 1:1 stoichiometries exist. Phase diagrams for salts would look similar, depending on the stoichiometry. Racemic compounds may also be treated as multicomponent crystals, with a phase diagram like the one shown for 1:1 co-crystal.

Phase diagram illustrations for other multicomponent systems are shown in Figure 1.4. The left phase diagram shows a scenario where component B forms a solvate. The right phase diagram shows a solid solution between A and B. The components are in this case perfectly miscible in the solid phase. Some tie-lines are also shown for illustration. The shape of the solid-liquid line depends on the crystal properties and liquid activity; however, it could be arched upwards or downwards.

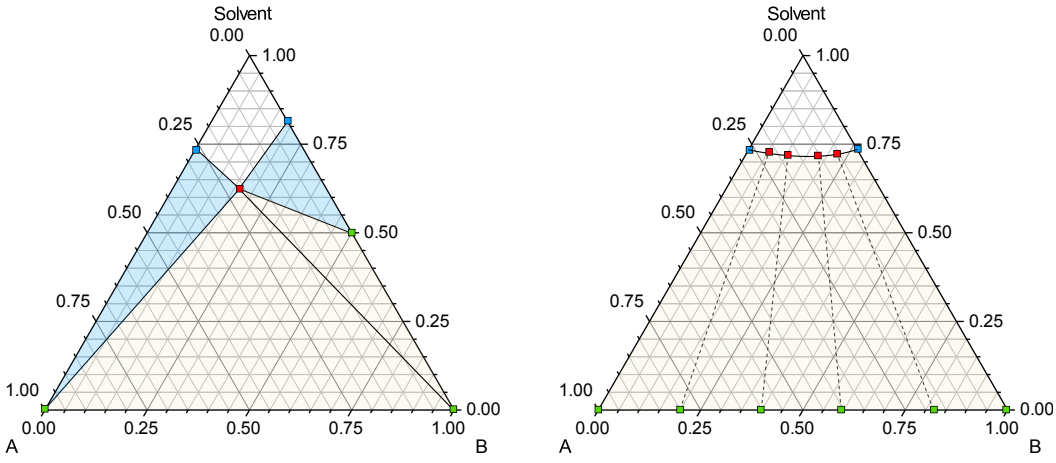

Figure 1.4. *Phase diagram illustrations for B solvate (left) and solid solution between A and B (right).*

It is clear that with additional components and solid phases, the phase diagrams become more complex and more important for process development where

selectivity of solid phase is critical. The measurement of such phase diagrams also introduces new challenges compared to single solute phase diagrams.

1.3. PHASE DIAGRAM MODELING AND MEASUREMENT

The solubility curve describes the boundary of liquid and solid-liquid regions of the phase diagram. Solubility is a thermodynamic property, different for each polymorph of the solute. The knowledge of the phase diagram is important when designing a crystallization process as it can be used to determine supersaturation and maximum yield. Solubility is often measured by equilibration methods where excess solute is suspended in a solvent to create a saturated solution. The concentration of the saturated solution is equal to the solubility and can be measured via High Performance Liquid Chromatography (HPLC), gravimetry or other methods. Temperature variation methods are also used to determine solubility by detecting when a solution becomes clear upon heating. This method has become popular with the introduction of equipment capable of automating this process for many samples at once.[16]

With multicomponent crystals, it is often not possible to apply the same practice in determining solubility. For example, if a co-crystal phase diagram is incongruent (asymmetrical), a co-crystal suspended in pure solvent will be metastable. Similarly, a solid solution may not be stable at every ratio. Moreover, for a solid solution the composition must be determined before solubility curve can be established as the composition of the starting solution used to prepare the solid solution may not be equivalent to the composition of the resulting solid solution. Knowledge of range of conditions under which a solid phase is stable is

also important in the case of a solvate. Binary phase diagrams are commonly determined by DSC (Differential Scanning Calorimetry) to map solid phases present. However, the stability of solid phases does not translate to phase diagrams with the introduction of a third component as solvent.

Phase diagrams for crystallization can also be modeled using solid-liquid equilibrium thermodynamics and activity coefficient models. There are many activity coefficient models available with continuous development in the area. Commonly used activity coefficient models include variations of UNIFAC,[17] UNIQUAC,[18] NRTL,[19] COSMO-RS,[20] SAFT[21] and others. While applications of activity coefficient models in vapor-liquid and liquid-liquid equilibria is well established, use in solid-liquid systems still leaves room for accuracy required for process development.

1.4. CONTINUOUS MANUFACTURING

Pharmaceuticals have been traditionally produced in mostly batch unit operations, however, in recent years there has been a lot of research and development activity in continuous manufacturing within the industry. All unit operations in the manufacturing chain from flow chemistry in synthesis through purification to continuous drug product manufacturing are being developed.[22–24] Along with some challenges, continuous manufacturing brings many potential benefits from technical to supply chain perspectives. Technical advantages include potentially better yields through process intensification, faster development cycle, operation at steady state rather than equilibrium, ease of automation and improved safety due to smaller process volume and

inventory.[25,26] Other economic advantages include, significantly reduced plant footprint, reduced lead time from raw materials to drug products and less inventory of intermediate.[27]

Furthermore, continuous manufacturing development has driven a lot of research in process understanding by implementing modeling for various unit operations[28] and process monitoring through process analytical technology (PAT).[29,30] These have applications in batch processes too, where model-based design and PAT allow for feedback control to limit batch to batch variability.[31–33] The CMAC Future Manufacturing Research Hub, where this research has been conducted, focuses on the acceleration of adoption of continuous manufacturing in collaboration with its industrial partners.

One of the challenges of continuous crystallization is fouling[34]. Continuous crystallizers, particularly plug flow and oscillatory crystallizers, will typically have a larger surface area to volume for the same throughput which helps with heat transfer but also provides more area for solute to nucleate and grow on. The buildup on of solute on crystallizer walls leads to more fouling reducing crystallizer performance in terms of heat transfer, particle quality and yield with the potential to result in a blockage. Fouling can be avoided or mitigated by operating at low levels of supersaturation. However, this means a longer plug flow crystallizer or more MSMPR stages must be employed for the same yield. Alternatively, corrective cycles may be used to remove encrustation.[35]

1.5. ANALYTICAL TECHNOLOGY

Verifying that a product meets specific criteria is a key aspect of every unit operation in the pharmaceutical industry with crystallization being no exception. Some key parameters which characterize a successful crystallization process are high chemical purity, target solid form, desired particle morphology and particle size distribution, all of which impact final product performance in patient and other manufacturing steps. There are also process parameters worth monitoring in a crystallization such as temperature, mother liquor composition and supersaturation which have an effect on the final product.

Traditional analytical techniques rely on offline measurements, where a process or product sample is removed and analyzed in a lab with significant time lag between sampling and result interpretation. Developments in process analytical technology have allowed for real time inline process monitoring. However, the accuracy of such techniques is in most cases limited compared to offline measurements which are still required for most unit operations by regulators. Nevertheless, inline monitoring can benefit both batch and continuous crystallization alike by providing better process understanding. In certain situations, real time data collection and processing allows for implementation of feedback control.

Both offline and inline tools have been used in this thesis to determine particle size and shape, solid composition and solid form, and liquid phase composition. Particle size measurements have been carried out by laser diffraction and microscopy with quantitative image analysis. Solid form has been determined by X-ray powder diffraction (XRPD), Differential Scanning Calorimetry (DSC) and

Raman or IR spectroscopy. DSC is a technique that monitors thermal events such as melting or solid form transformation during a temperature ramp, which vary between solid forms. XRPD is a very common technique in crystallography for identifying solid form. As the name suggests, XRPD works on the principle of diffraction and can be used to identify a solid form by looking at a diffraction pattern produced by the crystal lattice of the sample when subjected to X-ray radiation. Solid phase can also be identified using FTIR by looking at the absorbance profile of a solid sample where different functional groups and different bonding arrangements result in a change in response. Similarly, solid form can also be identified by Raman spectroscopy, which uses inelastic scattering of laser light. A main advantage is of this technique is that Raman can also be used inline with non-invasive probes to identify solid phase of suspended material in real time.

Liquid composition has been measured by Nuclear Magnetic Resonance (NMR), UV/vis spectroscopy and gravimetric analysis. NMR is used to determine molecular composition by subjecting a rotating sample to a magnetic field and measuring the resonant frequency. UV/vis spectroscopy works by monitoring the absorbance of a solution in the ultraviolet and visible light wavelengths due to electron transitions between energy levels. The signal intensity measured is proportional to the concentration of a species in solution.

1.6. MODEL COMPOUNDS

The co-crystal model system used for phase diagram measurement and process development was benzoic acid – isonicotinamide (BZA – INA). They are both small molecules with multiple hydrogen bonding sites. Only one polymorph of benzoic acid has been reported in the Cambridge Structural database (CSD), (ref code BENZAC).[36] However, isonicotinamide has several polymorphs (ref code EHOWIH01-06).[37–40] It also exists in multiple hydrate forms and forms several co-crystals.

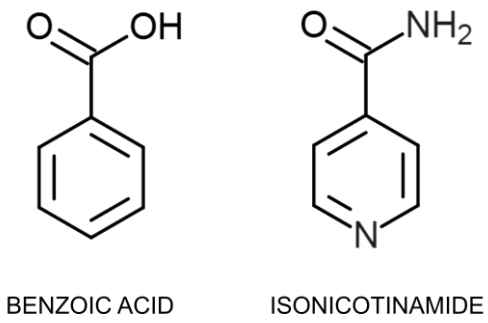

Figure 1.5. *Benzoic acid and isonicotinamide chemical structures.*

This co-crystal system of benzoic acid and isonicotinamide has been previously studied in literature, with two stoichiometries of the co-crystal observed: 2:1[41] and 1:1[42] and their structures solved. This model system has been used in Chapter 3 and Chapter 4.

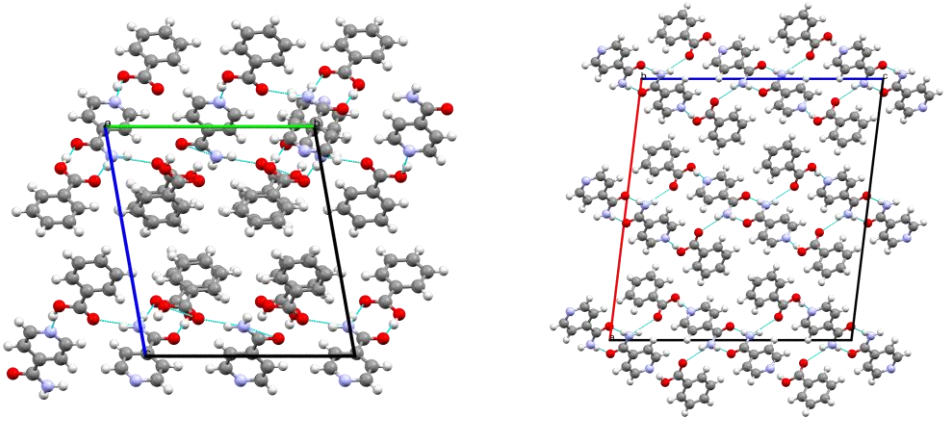

Figure 1.6. *Benzoic acid – isonicotinamide co-crystal structures. 2:1 (left) and 1:1 (right).*

The solid solution model system used involves pairs of the amino acids: L-Leucine, L-Valine and L-Isoleucine. The chemical structures of these amino acids, which exist in L and D enantiomers, are shown in Figure 1.7.

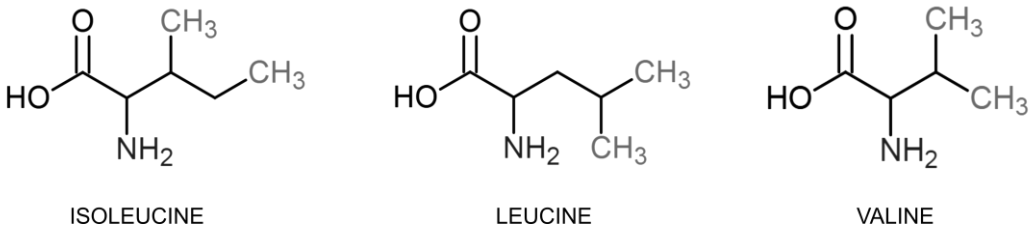

Figure 1.7. *Chemical structures of amino acids used for solid solutions.*

The structures of each solid solution pair have been solved in an associated journal publication and the structures are shown in Figure 1.8.[43] These model systems are the subject of Chapter 5.

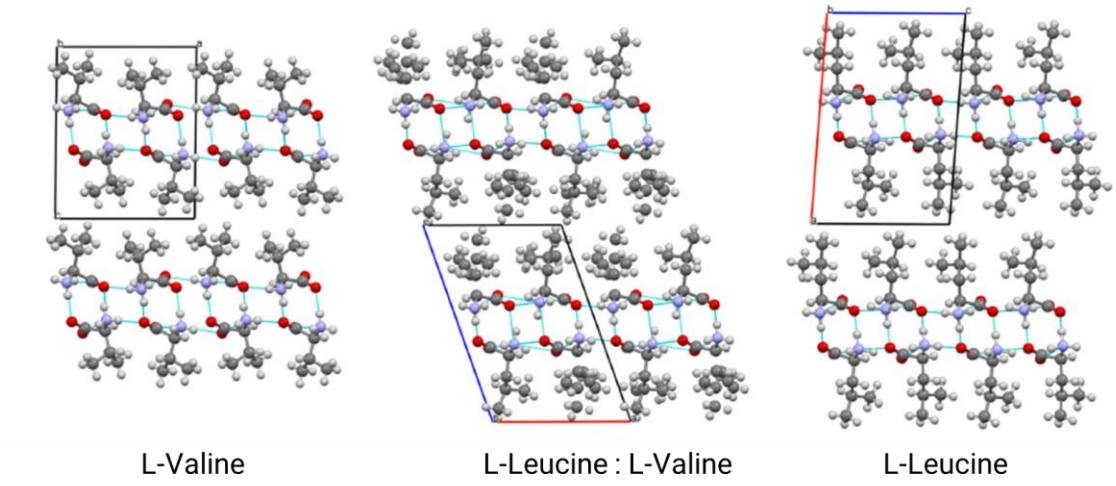

Figure 1.8. *Crystal structures of L-Valine, L-Leucine and the solid solution.*

Other molecules mentioned in Chapter 2 are Paracetamol, Lovastatin and 4-aminobenzoic acid, shown in Figure 1.9. These are not used in any multicomponent systems in this work, however, they are all pharmaceutically relevant compounds used to test semi-empirical methods to assist in phase diagram determination.

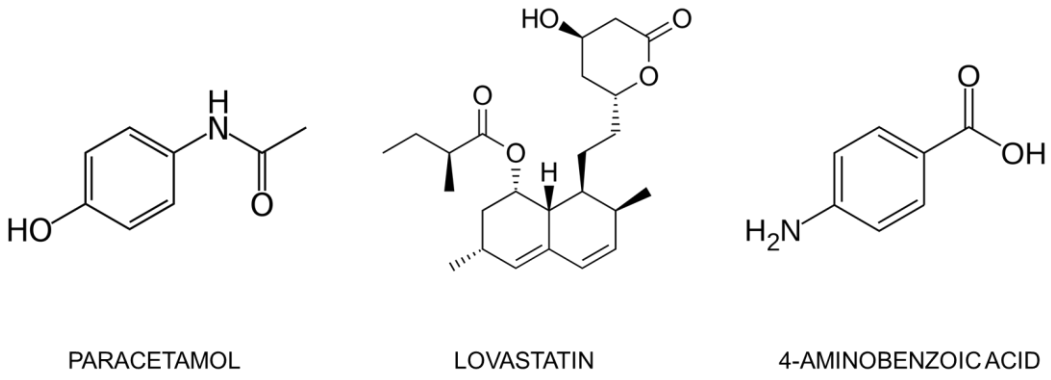

Figure 1.9. *Model compounds used for thermodynamic modeling in Chapter 2.*

1.7. GENERAL AIMS AND OBJECTIVES OF RESEARCH

Most research related to multicomponent crystals involves screening for new solid forms. This thesis covers aspects of developing a continuous crystallization process for multicomponent systems, from building phase diagrams to operating lab scale continuous crystallizers. In several aspects, crystallization and isolation of multicomponent crystals requires additional considerations compared to single component materials. Chapter 2 focuses on thermodynamic modelling approaches to assist experimental phase diagram determination by combining experimental measurements with models. The model has been applied to solubilities of additional polymorphs and solubilities of solutes in solvent mixtures. Chapter 3 presents novel measurement techniques to aid in experimental co-crystal phase diagram determination in less time compared to commonly used methods while retaining accuracy and to stress the importance of solid phase verification where multiple forms may appear. The simplification and reduction in experimental time is achieved by focusing on the eutectic points of the phase diagram and approximations instead of measuring the entire solid-liquid line. Chapter 4 shows continuous selective crystallization process development of a co-crystal involving benzoic acid and isonicotinamide which exists in 2:1 and 1:1 stoichiometries. Finally, Chapter 5 demonstrates a continuous crystallization process of solid solutions composed of pairs of amino acids: L-Valine, L-Leucine and L-Isoleucine.

CHAPTER 2

THERMODYNAMIC MODELLING FOR PHASE DIAGRAM DETERMINATION

2.1. INTRODUCTION

The determination of phase diagrams is an important step in any chemical process development involving multiple phases. However, determining phase diagrams experimentally can be very time and material consuming as the number of components and conditions increases. Phase diagrams can also be modeled through predictive models using thermodynamic laws of phase equilibria. Thermodynamic modeling of phase diagrams has been previously applied in a wide range of scientific areas and industrial applications including vapor-liquid separations,[44] crystallization[45] and liquid-liquid extraction.[46] However, this chapter will focus on the application of thermodynamic phase diagram modeling relevant to industrial crystallization of pharmaceuticals and similar compounds. Therefore, the main area of interest of this chapter is solid-liquid equilibrium between solvents and small organic molecules.

Many different (activity coefficient) models have been used to predict solid-liquid phase diagrams for organic molecules in solvents. Some examples of these models are UNIQUAC,[18] UNIFAC,[47] NRTL,[48] COMSO-RS,[49] SAFT[21] and many variations of these models such as modified UNIFAC,[17] NRTL-SAC,[19] COSMO-SAC,[50] PC-SAFT[51] and many others. Thermodynamic models have been applied to single solute – single solvent systems for several APIs and amino acids in various solvents over a range of temperatures. Dependence of solubility on pH has also been modeled by including a Debye-Hückel term[52] in the activity coefficient model.[53] Solutes in solvent mixtures have also been modeled. Solid-liquid phase equilibria are not yet commonly applied to multicomponent crystals,

however, a recent study shows successful application of PC-SAFT to a co-crystal system[54] to model the phase diagram and effects of pH.

Current activity coefficient models are useful in solvent screening when used to determine solubility, however, they seem to be unable to consistently provide the accuracy required for process development. This chapter focuses on utilizing existing experimental measurements to assist in further predictions with same components but different phases. By using related experimental data, the model accuracy should be improved. UNIQUAC was used for all parametrization and predictions as it requires fitting relatively few parameters. The first example uses measured solubility of stable polymorphs to parametrize an activity coefficient model and use the model to determine solubility of metastable polymorphs of the same compound. Solubilities of metastable forms are often difficult to measure due to their propensity to transform to the stable phase. The second example uses solubilities of a compound in single solvents to determine mixed solvent solubility. From several single solvent solubilities, it is possible to model the mixed solvent solubility of all combinations of solvents parametrized. This can save time in determining the shape of the solubility curve to assist in choosing a solvent-antisolvent pair or filtration wash solvent. The last component of this chapter provides examples of estimating the co-crystal solid-liquid line in a ternary phase diagram.

2.2. THERMODYNAMIC MODELING BACKGROUND

2.2.1. PHASE EQUILIBRIA

Phase equilibrium is an area of thermodynamics which deals with the equilibrium between different states of matter. A phase is defined as region with uniform physical properties. These include states of matter but also different solid states (polymorphs) or immiscible liquids. The number of degrees of freedom (*F*) is given by Gibbs phase rule:[55]

$$F = C - P + 2 \quad (1)$$

Where *C* is the number of components and *P* is the number of phases. Chemical potential is the partial derivative of the free energy as molecules of the given species are added to the system and is represented as *μ*. In equilibrium between two phases, the chemical potential of all species is equal in each phase. In this case, phases *α* and *β*.[56]

$$\mu_i^{\alpha} = \mu_i^{\beta} \quad (2)$$

2.2.2. SOLID-LIQUID EQUILIBRIUM

In the context of crystallization, solid-liquid equilibrium is of most interest. Knowing the solubility of a compound is key for determining supersaturation, the driving force of crystallization, and for process development. In certain cases, predicting liquid-liquid equilibrium may also be useful for understanding nucleation, however, that is not the focus of this chapter. As has been described in the previous section, in equilibrium the chemical potential of species is equal in present phases. For species *i*, in solid (*s*) and liquid (*l*) phases.[56]

$$\mu_i^s = \mu_i^l \tag{3}$$

$$\mu_i^{o,s}(T,P) = \mu_i^{o,l}(T,P) + RT \ln x_i \gamma_i \tag{4}$$

$$RT \ln x_i \gamma_i = \mu_i^{o,s} - \mu_i^{o,l}(T,P) \tag{5}$$

$$\ln x_i \gamma_i = \frac{\Delta G_i(T,P)}{RT} \tag{6}$$

Where x_i and γ_i are the mole fraction and activity coefficient of component *i* in the liquid phase at equilibrium. Therefore, x_i is the solubility of species *i*. μ^o is the chemical potential at reference conditions.

The Gibbs free energy of the phase transformation can written in terms of enthalpy and entropy changes.[55]

$$\Delta G_i = \Delta H_i - T\Delta S_i \tag{7}$$

The enthalpy of the phase transformation at temperature *T* is equal to the sum of the following:

1. Enthalpy of heating species *i* from temperature *T* to the melting point.
2. Enthalpy of fusion of species *i* at the melting point.
3. Enthalpy of supercooling liquid species *i* back to temperature *T*.

This sum is represented here:

$$\Delta H_i(T) = \int_T^{T_m} c_P^s \, dT + \Delta H_i(T_m) + \int_{T_m}^{T} c_P^l \, dT \tag{8}$$

Where the heat capacities of the solid and liquid phases are functions of temperature. The two heat capacities are often combined into a single term Δc_P.

$$\Delta c_P = c_P^l - c_P^s \tag{9}$$

This allows equation (8) to be simplified to:

$$\Delta H_i(T) = \Delta H_i(T_m) + \int_{T_m}^{T} \Delta c_P \, dT \tag{10}$$

When at the melting temperature, the Gibbs free energy of the phase transformation is zero, $\Delta G_i = 0$. Therefore, at the melting point:

$$\Delta S_i(T_m) = \frac{\Delta H_i(T_m)}{T_m} \tag{11}$$

Due to this relationship, the entropy of fusion at temperature *T* can be extrapolated as was done with heat of fusion:

$$\Delta S_i(T) = \frac{\Delta H_i(T_m)}{T_m} + \int_{T_m}^{T} \frac{\Delta c_P}{T} dT \tag{12}$$

The terms for $\Delta H_i(T)$ and $\Delta S_i(T)$ can be substituted back into equation (7) to find Gibbs free energy of the phase transformation at temperature T:

$$\Delta G_i(T) = \Delta H_i(T_m) + \int_{T_m}^{T} \Delta c_P \, dT - \frac{T\Delta H_i(T_m)}{T_m} - T\int_{T_m}^{T} \frac{\Delta c_P}{T} dT \tag{13}$$

This expression for Gibbs free energy can be related back to equilibrium composition of the liquid phase using equation (6):

$$\ln x_i\gamma_i = \frac{\Delta H_i(T_m)}{RT} - \frac{\Delta H_i(T_m)}{RT_m} + \frac{1}{RT}\int_{T_m}^{T} \Delta c_P \, dT - \frac{1}{R}\int_{T_m}^{T} \frac{\Delta c_P}{T} dT \tag{14}$$

If a functional form of Δc_P is known, this can be integrated. However, in order to simplify this further, some assumptions must be made. A common assumption is

that Δc_P is a constant term which allows us to integrate the integral terms without knowing the function of Δc_P and simplify the expression further:

$$\ln x_i\gamma_i = \frac{\Delta H_i(T_m)}{R}\left(\frac{1}{T_m} - \frac{1}{T}\right) - \frac{\Delta c_P}{R}\left(1 - \frac{T_m}{T} - \ln\frac{T}{T_m}\right) \quad (15)$$

This equation gives us the solubility x_i, related to the activity coefficient γ_i and measurable properties of the solid phase. The impact of crystal properties on the solubility is given by the parameters on the right-hand side of the equation. These include the heat of fusion ($\Delta H_i(T_m)$), melting temperature (T_m) and the difference in solid and liquid heat capacities (Δc_P). All of these properties can be measured by DSC for a given solid form. These parameters capture all information about the polymorph related to the solubility of the compound.

However, Δc_P term is often not used in thermodynamic models as its effect on solubility is deemed insignificant, especially when temperature T is close to the melting point.[57] However, in other cases, this can have a profound impact on the calculated equilibrium composition. Some studies show that approximating the term as equal to entropy of fusion yields improved results.[58]

$$\Delta c_P \approx \Delta S_i(T_m) = \frac{\Delta H_i(T_m)}{T_m} \quad (16)$$

In most cases, Δc_P is assumed to be zero and the expression simplifies further requiring only the heat of fusion and melting point of the solid phase. DSC is a relatively simple and accurate measurement, and it only needs to be carried out once for each solid phase to model the solubility at any condition.[47]

$$\ln x_i\gamma_i = \frac{\Delta H_i(T_m)}{R}\left(\frac{1}{T_m} - \frac{1}{T}\right) \quad (17)$$

Once the solid phase thermodynamic parameters have been measured, the other part of the model is the activity coefficient, γ_i. This term accounts for the non-ideality of the system in the liquid phase and comes from interactions of solute and solvent molecules. If the activity coefficient is equal to 1, the solute-solvent system follows ideal solubility. However, since choice of solvent clearly has a strong effect on solubility, this idealization rarely reflects reality. Therefore, an activity coefficient model must be used to predict solubility.

2.2.3. MULTICOMPONENT CRYSTAL SOLUBILITY

When phases with multiple components in a fixed composition are in equilibrium, it is not the individual chemical potentials of species that must be in equilibrium, but the stoichiometrically weighted sum of chemical potentials of all species in a phase.

$$\sum_i \nu_i^s \mu_i^s = \sum_i \nu_i^l \mu_i^l \quad (18)$$

Co-crystal solubility can be defined by a solubility product:

$$K_{sp} = \prod_i a_i^{\nu_i^l} = \prod_i (x_i\gamma_i)^{\nu_i^l} \quad (19)$$

Analogous to equation (6) for single components:

$$\ln \prod_i (x_i\gamma_i)^{\nu_i^l} = \ln \prod_i \left(x_i^{CC}\gamma_i\right)^{\nu_i^s} - \frac{\Delta G(T)}{RT} \quad (20)$$

Where ΔG is the Gibbs free energy of fusion and x_i^{CC} is the composition of the co-crystal. In a binary phase diagram, at the congruent melting composition (x^*) and melting temperature (T^*), $x_i^{CC} = x_i$ and $\Delta G = 0$. Therefore, the solubility product at this point can be described by:

$$\ln K_{sp} = \ln \prod_i \left(x_i^{CC} \gamma_i\right)^{v_i}$$

For 1:1 co-crystal in an ideal mixture at T*, K_{sp} = 1/4. For 2:1 co-crystal, K_{sp} = 2/9. The solubility product K_{sp} for an ideal solution (*i.e.* γ_A and γ_B are equal to 1) can be calculated using similarly to equation (17) for single component crystals by expanding ΔG and excluding the Δc_P term. For 1:1 co-crystal, this becomes:

$$K_{sp} = x_A x_B \approx \frac{1}{4} \exp\left[-\frac{\Delta H(T_m)}{R}\left(\frac{1}{T} - \frac{1}{T_m}\right)\right] \quad (21)$$

2.2.4. ACTIVITY COEFFICIENT MODELS

Activity coefficient models exist to account for the interactions between molecules in the liquid phase and correct for non-ideal behavior. Different models use very different approaches to do this, from computational chemistry through thermodynamic statistics to data driven approaches. Example activity coefficient models of each are described here. COSMO-RS[20] is a quantum chemistry-based activity coefficient model. It is an *ab initio* model which can be applied to any molecule without pre-existing knowledge. UNIFAC[59] on the other hand is an activity coefficient model which takes the functional groups present in a molecule with determined size to regress binary interaction parameters from various equilibrium data sets. A molecule can then be broken down into its functional groups to determine the activity coefficient using the regressed parameters. The

limitation is that all binary interaction parameters must be obtained for all possible pairs of functional groups of all species present. With large databases of equilibrium properties and digitization of data, it is inevitable that data driven approaches will be developed with machine learning algorithms to develop models for activity coefficient calculations given a range of molecular descriptors.

For this study, UNIQUAC (universal quasichemical) was chosen as the activity coefficient model of choice due to having relatively few adjustable parameters. This allows the model to be parametrized based on few data points without the risk of overfitting and to be used to predict activity coefficients at new conditions. UNIQUAC has several molecule specific parameters, *r*, *q* and *q'* as well as binary interaction parameters (τ_{ij}) as inputs. Compound specific parameters can also be calculated from existing approaches. UNIQUAC equations for binary mixtures are widely available in literature.[18] For the applications in this thesis, the version for more than two components in the liquid phase was used. Calculations of the UNIQUAC model are explained here. Required model input parameters are discussed below. The outputs of the model are the activity coefficients of each species present in the liquid phase.

Segmentation fraction ϕ for component *i*:

$$\phi_i = \frac{x_i r_i}{\sum_j x_j r_j} \tag{22}$$

Area fractions θ and θ' for component *i*:

$$\theta_i = \frac{x_i q_i}{\sum_j x_j q_j} \qquad \theta_i' = \frac{x_i q_i'}{\sum_j x_j q_j'} \tag{23}$$

The activity coefficient of component *i* is:[18]

$$\ln \gamma_i = \ln \frac{\phi_i}{x_i} + \left(\frac{z}{2}\right) q_i \ln \frac{\theta_i}{\phi_i} + l_i - \frac{\phi_i}{x_i} \sum_j x_j l_j - q_i' \ln \sum_j \theta_j' \tau_{ji} + q_i' - q_i' \sum_j \frac{\theta_j' \tau_{ij}}{\sum_k \theta_k' \tau_{kj}} \tag{24}$$

Where

$$l_j = \frac{z}{2}(r_j - q_j) - (r_j - 1) \tag{25}$$

Where *z* is typically set to 10. The binary interaction parameter dependence on temperature is captured by:

The binary interaction parameter τ_{ij} must be calculated from existing equilibrium data. For each pair, two parameters are required. For example, τ_{12} and τ_{21} for components 1 and 2. This can be from a solubility point or vapor-liquid data.

$$\tau_{ij} = \exp\left(-\frac{a_{ij}}{T}\right) \tag{26}$$

Component specific structural parameters, r_i, q_i and q_i' are related to the molecule size and surface area. These parameters can be calculated from the contribution of each functional group using UNIFAC *r* and *q* parameters. For most molecules, $q_i = q_i'$, except for water and alcohols, where values of q_i' are reported depending on the number of carbons.[18]

2.3. METHODOLOGY

2.3.1. UNIQUAC IMPLEMENTATION

UNIQUAC equations presented in thermodynamic background section have been implemented in a Python 2.7 environment. A python class for UNIQUAC

was created and implemented within a wider framework developed by Leo Lue[60] which calculates an activity coefficient for a given mixture at specified composition and temperature.

2.3.2. MODEL PARAMETER ESTIMATION

r, *q* and *q'* parameters for each molecule were calculated using functional group contributions from literature.[18,61] Solid phase properties (ΔH, T_m) were found in literature or measured using DSC (DSC214 Polyma, Netzsch), using a heating rate of 10 K/min.

Binary interaction parameters τ_{ij} for API-solvent in this case were obtained by fitting the model to existing data. For solvent-solvent binary interaction parameters (show in Table 2.8), values were obtained from literature from other equilibrium systems or fitted to existing data. The interaction parameters were collected and used differently depending on what data was available and the application. This semi-empirical approach is categorized into three parts:

1. Solubility of (metastable) polymorph modeling by parametrizing the model using known (stable) polymorph solubility data
2. Solubility of an API in solvent mixtures modeled by parametrizing the model using data from single solvent solubilities and solvent-solvent equilibrium data
3. Solubility modeling of a co-crystal in a ternary phase diagram estimated from measured eutectic point compositions

Each of these cases uses a combination of semi-empirical models fitted with related experimental data to bridge the gap between *ab initio* models and complete experimental determination.

2.3.3. POLYMORPH SOLUBILITY PREDICTION

Polymorphs of a compound have different solubilities. In a binary mixture, the polymorph with lower solubility is termed the stable form. Which form that is may change from solvent to solvent and across temperatures. Solubility of a metastable compound may be difficult to measure as solubility is a thermodynamic property and requires sufficient equilibration time, during which solvent mediated transformation may occur. If the activity coefficient model can be applied to work for one polymorph, the only difference in the solubility of other polymorphs is solid phase parameters (ΔH, T_m), easily measured by DSC for a single component. The Δc_P term was ignored.

This approach was applied to paracetamol and 4-aminobenzoic acid (4-ABA). Paracetamol has two forms, form I and form II. Solubility of both polymorphs in water is available[62] along with solid phase thermodynamic properties.[63,64] Interaction parameters were parametrized using the solubility of form I. The resulting activity coefficient model was applied to determine solubility of form II and compared with literature data. 4-aminobenzoic acid has two forms, α and β with solubility data and thermodynamic properties available in literature.[65,66] A very similar approach using UNIQUAC and NRTL was also found in literature in the work of Mirmehrabi *et al.*[67] after this work was carried out.

2.3.4. MIXED SOLVENT SOLUBILITY PREDICTION

Mixed solvent solubility curves have a wide range of shapes, often with local maxima.[68] These features are important to know to determine the supersaturation profile during antisolvent crystallization or when choosing a wash solvent. Measuring solubility in all potential binary solvent pairs with temperature dependence can be exponentially time-consuming. However, the approach used here only requires solubility in pure solvents, significantly reducing the experimental time.

This approach was applied to paracetamol form I, *α*-form of 4-amino benzoic acid and lovastatin. Interaction parameters for solute-solvent were parametrized from pure solvent solubility data. Solvent-solvent parameters were obtained from literature based on VLE data.

2.3.5. CO-CRYSTAL SOLUBILITY PREDICTION

The solid-liquid line of a 1:1 co-crystal of benzoic acid and isonicotinamide in ethanol was estimated. The measurement of the eutectic points of this phase diagram experimentally is the subject of Chapter 3. The solid-liquid line was calculated from these eutectic points by assuming a constant solubility product. The solubility product was calculated in three ways:

1. Based on ideal solubility
2. Averaged solubility product from eutectic points
3. Averaged solubility product from measured points for comparison

The heat of fusion and melting point of the 1:1 co-crystal were determined by DSC.

2.4. RESULTS

2.4.1. SINGLE COMPONENT CRYSTALS SOLUBILITY PREDICTION

Single component structural UNIQUAC parameters were calculated using the functional group contribution method.[61] Due to the complexity of lovastatin, there are several ways to divide it into functional groups. Functional groups for Lovastatin used were 4xCH_3, 5xCH_2, 7xCH, CH=C, CH=CH, OH, and 2x CH_2COO (one CHCOO was substituted for CH_2COO due to availability of *r* and *q* parameters). Similarly for paracetamol, due to the unavailability of parameters for ACNH, $ACNH_2$ was substituted instead as was done by Hojjati & Rohani.[69] 'A' in functional groups refers to groups attached to an aromatic ring. Values for *q'* were obtained from literature.[18] All *r*, *q* and *q'* values for solutes and solvents used here are shown in Table 2.1.

Table 2.1. *Structural UNIQUAC Parameters for Paracetamol and Relevant Solvents calculated from functional groups.*[61]

	r_i	q_i	q_i'
Paracetamol	5.7528	4.544	4.544
4-ABA	5.0178	4.04	4.04
Lovastatin	16.4628	13.271	13.271
Water	0.92	1.40	1.00
2-propanol	3.2491	3.124	0.89
Acetone	2.5735	2.336	2.336
Ethanol	2.5755	2.588	0.92

PARACETAMOL – PARAMETER FITTING

Thermodynamic solid properties of paracetamol from literature are shown in Table 2.2. Experimental values for Δc_P are not shown as they were assumed to be zero in the model.

Table 2.2. *Paracetamol Polymorph Thermodynamic Properties.*

Form	ΔH^{fus} *(kJ/mol)*	T_m *(K)*
I	27.1[63]	443.6[63]
II	26.9[64]	430.15[64]

Form I solubility data from literature in water,[62] 2-propanol and acetone[63] was used to fit UNIQUAC binary interaction parameters. The resulting fits are shown in Figure 2.1, Figure 2.2 and Figure 2.3 for solubilities in water, 2-propanol and acetone respectively. UNIQUAC parameters with good agreement were found for water and 2-propanol. The UNIQUAC fit in acetone was not able to find a solution with perfect agreement with the data. The parameters obtained are presented in Table 2.3.

Table 2.3. *UNIQUAC binary adjustable parameters obtained from fitting paracetamol form I solubility data.*

Paracetamol (*i*) - Solvent (*j*)	a_{ij} (K)	a_{ji} (K)
Water	320.217	-190.563
2-propanol	-313.309	546.977
Acetone	-249.084	390.274

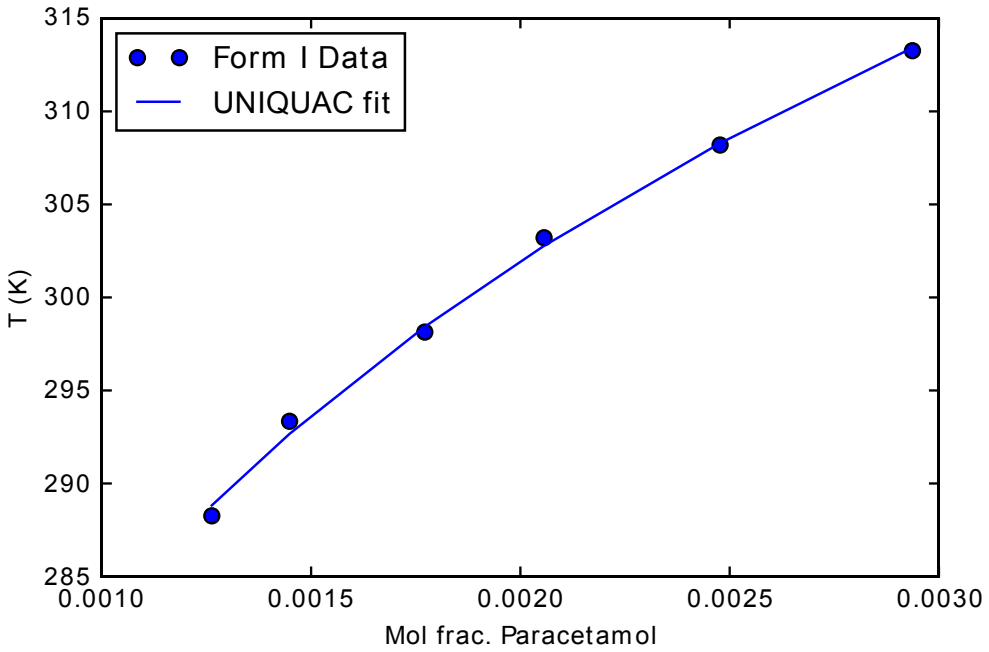

Figure 2.1. *UNIQUAC adjustable parameters fitted to Paracetamol form I solubility in water.*[62]

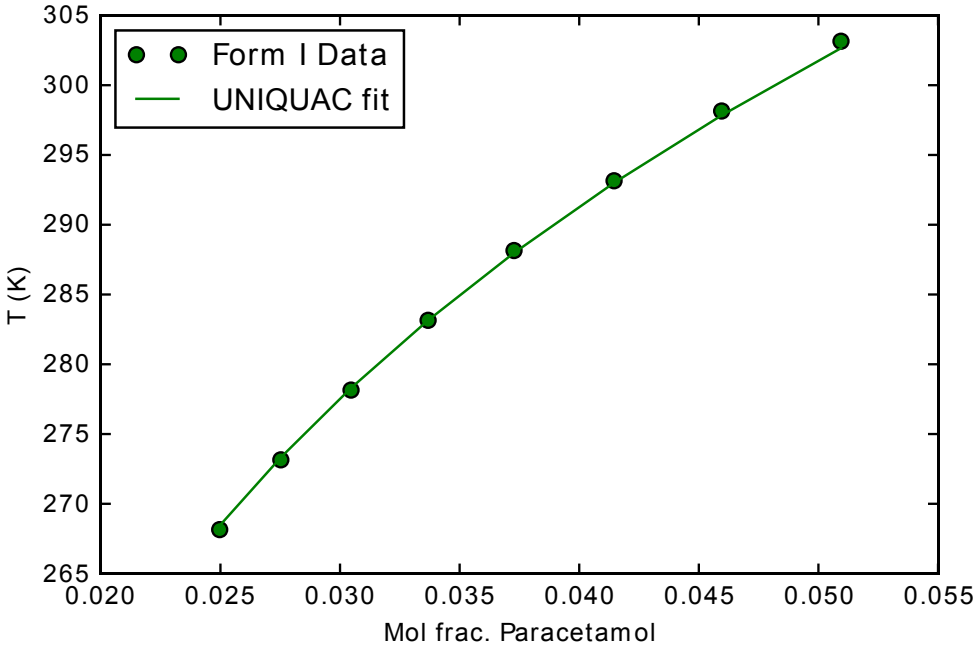

Figure 2.2. *UNIQUAC adjustable parameters fitted to Paracetamol form I solubility in 2-propanol.*[63]

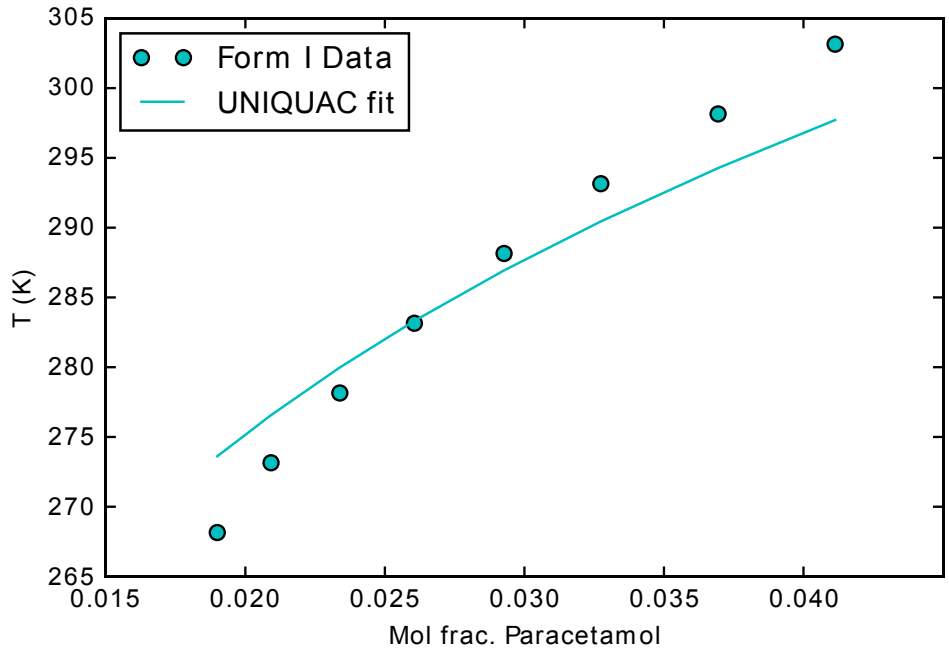

Figure 2.3. *UNIQUAC adjustable parameters fitted to Paracetamol form I solubility in acetone.*[63]

4-AMINOBENZOIC ACID – PARAMETER FITTING

Solubility data for 4-aminobenzoic acid in various solvents has been reported for its two polymorphs, alpha and beta.[65,66] The study by Gracin & Rasmuson[65] also outlines the thermodynamic properties of both solid phases. The heat of fusion of the beta form was approximated from the heat of fusion of the alpha form and the heat of transformation from beta to alpha.

Table 2.4. *4-ABA Polymorph Thermodynamic Properties.*[65]

Form	ΔH^{fus} *(kJ/mol)*	T_m *(K)*
α	24.1	460.4
β	26.6*	418

* Heat of fusion was determined by summing heat of transformation and heat of fusion of α.

Binary interaction parameters for 4-ABA were determined in two solvents, water and ethanol. The resulting fits are shown in Figure 2.4 and Figure 2.5 for water and ethanol respectively. The fit for solubility in water is agreeable, however, in ethanol the temperature dependence of solubility is not captured well outside of 290-295K. The new binary interaction parameters obtained are presented in Table 2.5.

Table 2.5. *UNIQUAC binary adjustable parameters obtained from fitting 4-ABA form α solubility data.*

4-ABA (*i*) - Solvent (*j*)	a_{ij} (K)	a_{ji} (K)
Water	189.924	-30.037
Ethanol	-313.398	552.205

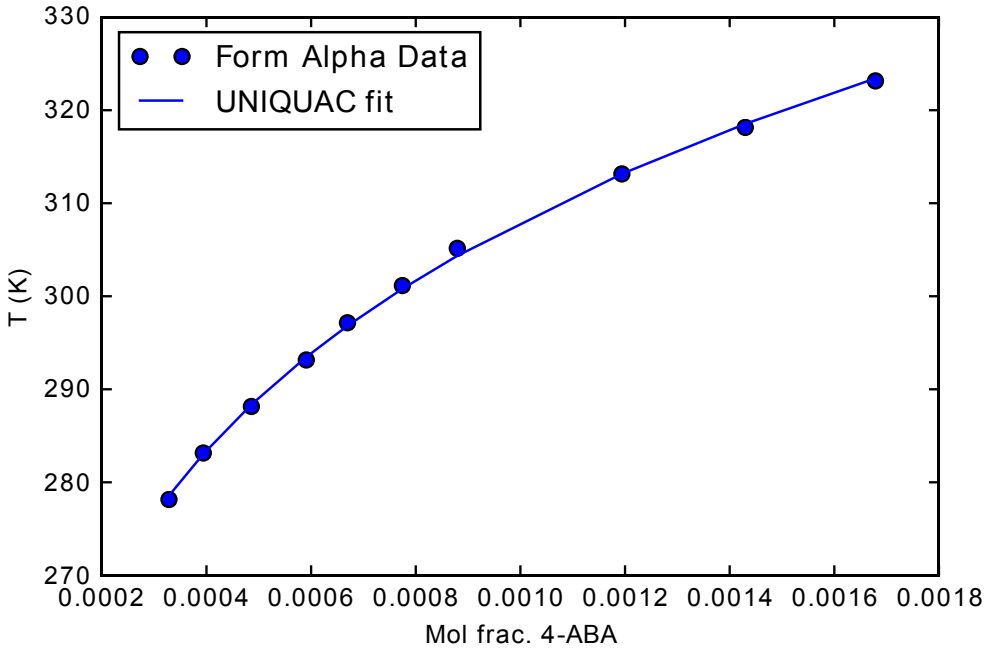

Figure 2.4. *UNIQUAC adjustable parameters fitted to 4-ABA form alpha solubility in water.*[65]

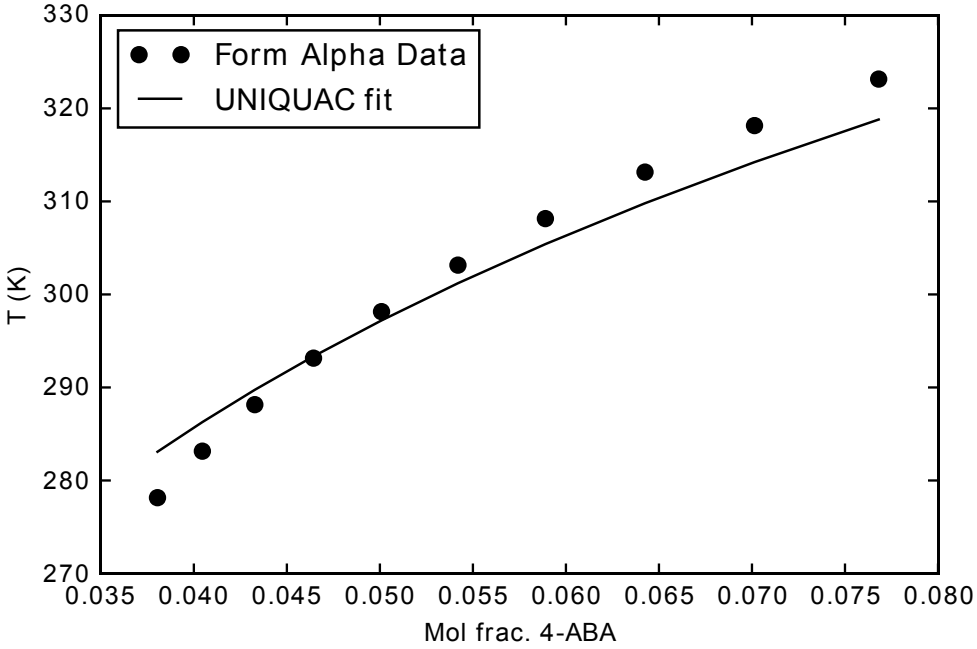

Figure 2.5. *UNIQUAC adjustable parameters fitted to 4-ABA form alpha solubility in ethanol.*[66]

The inability to fit some of these curves well may be caused by the inability of the activity coefficient model to capture the effect of solvent or by the omission of some solid phase parameters.

LOVASTATIN – PARAMETER FITTING

Lovastatin solubility data is available in the literature for several solvents.[70–72] Solubility in water and acetone-water mixtures at 25 °C was determined gravimetrically in-house by John McGinty and Andrew Manson after 24 hour equilibration.

Table 2.6. *Lovastatin thermodynamic properties.*[70]

ΔH^{fus} *(kJ/mol)*	T_m *(K)*
43.136	445.5

Solubility in water is practically negligible which makes obtaining lovastatin-water parameters uncertain. For the purpose of fitting parameters, solubility was set to an arbitrary low value. Acetone-lovastatin parameters were fitted to data from literature.[72] The resulting fit is shown in Figure 2.6. The new obtained interaction parameters are in Table 2.7.

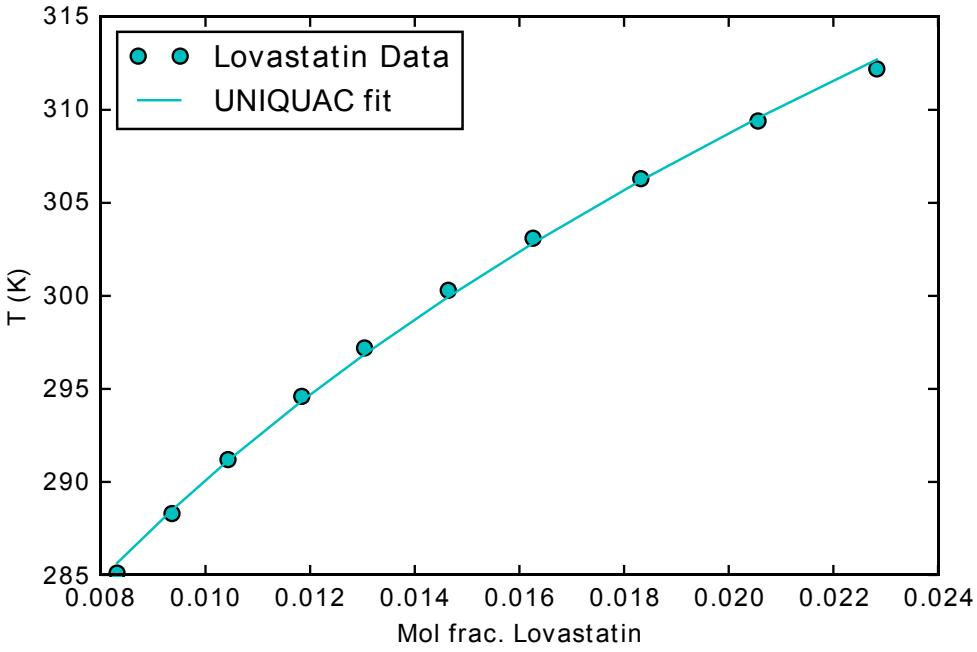

Figure 2.6. *UNIQUAC adjustable parameters fitted to lovastatin solubility in acetone.*[72]

Table 2.7. *UNIQUAC binary adjustable parameters obtained from fitting Lovastatin solubility data.*

Lovastatin (*i*) - Solvent (*j*)	a_{ij} (K)	a_{ji} (K)
Water*	18.859	101.358
Acetone	386.244	-187.486

*fitted to single arbitrary point as solubility in water is very low

POLYMORPH SOLUBILITY PREDICTION

With a UNIQUAC model parametrized using solubility data of one polymorph, the solubility of the other polymorph was predicted. Prediction of form II paracetamol solubility in water is shown in Figure 2.7.

Despite ignoring the Δc_P term for both polymorphs, the solubility prediction of form II is consistent with the data. Given the significant solubility difference between them, the activity model has successfully calculated activity coefficients at significantly different conditions from the fitted data.

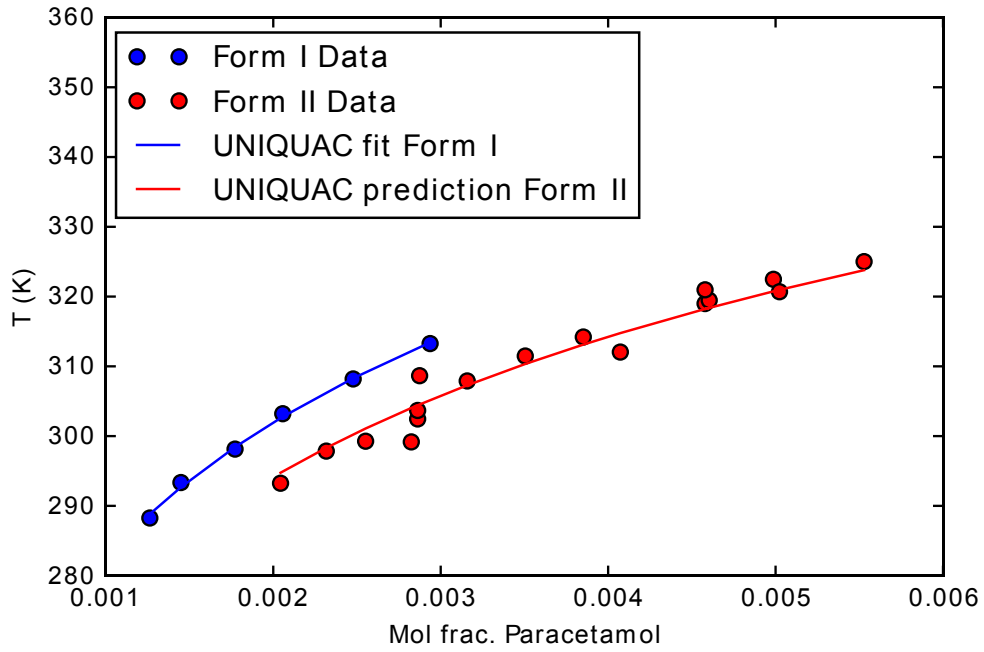

***Figure 2.7**. Paracetamol form II solubility in water[62] prediction using from obtained UNIQUAC parameters.*

Prediction of solubility of beta form of 4-ABA in water and ethanol is shown in Figure 2.8 and Figure 2.9 respectively. The solubility of beta form of 4-ABA is very similar to that of the alpha form in both water and ethanol. However, the prediction of beta solubility is not very consistent with the data. Since the measured

solubilities of both polymorphs are similar, the liquid phases in equilibrium with the solid phase would have similar composition and therefore similar activity coefficients. Since the solubility prediction does not agree with data, the thermodynamic properties of the solid phase used are not sufficient. This could be attributed either to the omitted Δc_P term or the fact that heat of fusion of beta form was approximated from heat of fusion of alpha and the heat of transformation from beta to alpha especially since the transformation occurs at significantly lower temperature below the melting point.

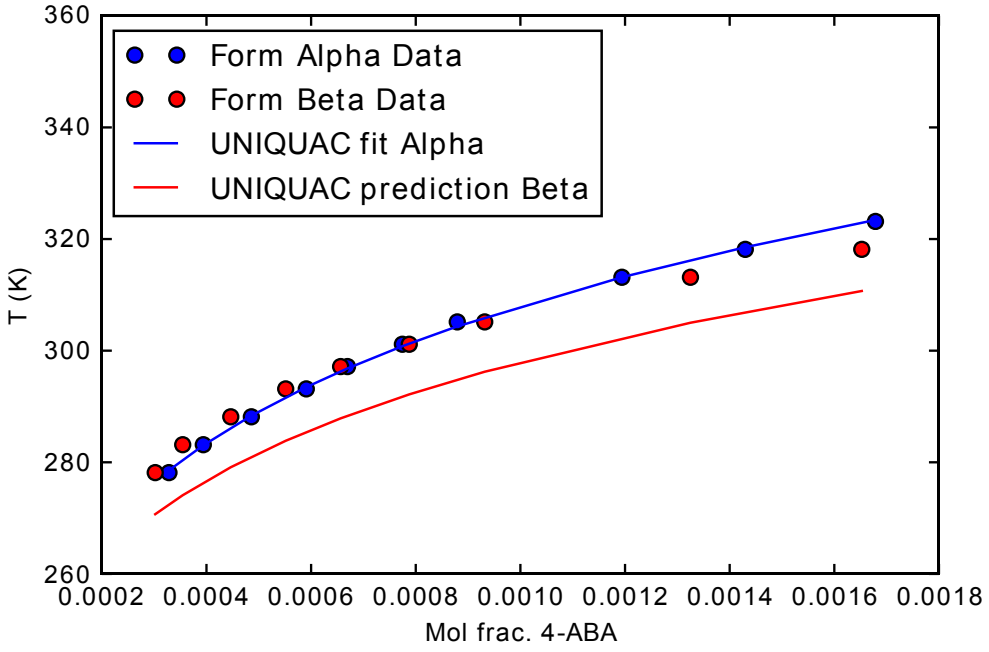

Figure 2.8. *4-ABA form β solubility in water[65] prediction using from obtained UNIQUAC parameters.*

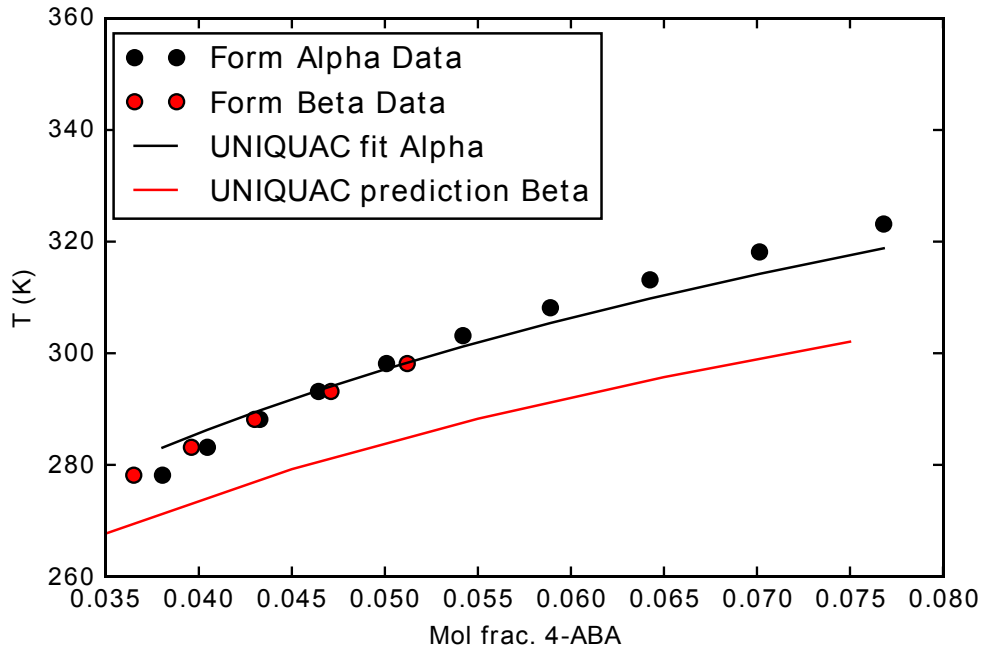

Figure 2.9. *4-ABA form β solubility in ethanol[66] prediction using from obtained UNIQUAC parameters.*

MIXED SOLVENT SOLUBILITY PREDICTION

Solvent-solvent parameters from literature used for predicting solubility in mixed solvents are shown in Table 2.8. For water – 2-propanol, two sets of parameters from different sources were tested. For case (1), parameters from Hojjati & Rohani[69] obtained from fitting VLE data were used. Parameters from case (2) come from a ternary system from Gironi & Lamberti.[73] All red curves in the figures in this chapter are predictions calculated using the UNIQUAC parameters presented.

Table 2.8. *Binary solvent-solvent parameters obtained from literature.*

Water (*i*) – Other solvent (*j*)	a_{ij}	a_{ji}
2-propanol (1)[69]	-46.45	316.3
2-propanol (2)[73]	251.9	158.5
Acetone[74]	-179.961	-81.561
Ethanol[75]*	8.811	79.030

*Parameters from Voutsas *et al*. calculated at 15 °C

Paracetamol solubility at 25 °C was predicted in water – 2-propanol solvent mixture of varying compositions. The results are shown in Figure 2.10 are overlaid with solubility data from Hojjati & Rohani.[76] The UNIQUAC parameters for paracetamol – solvent used for the predictions are the ones fitted in pure solvents. UNIQUAC (1) uses water – 2-propanol (1) parameters from Table 2.8, UNIQUAC (2) uses water – 2-propanol parameters (2).

Both UNIQUAC predictions fit well in pure solvents due to parameters being fit to pure solubility curves. The local solubility maximum in solvent mixture is also captured by both sets of parameters. The difference between the two curves shows the sensitivity of the prediction to which solvent – solvent parameters are used. The deviation from UNIQUAC fit by Hojjati & Rohani[69] is due to different paracetamol – solvent parameters as well as the neglected Δc_P term in this work.

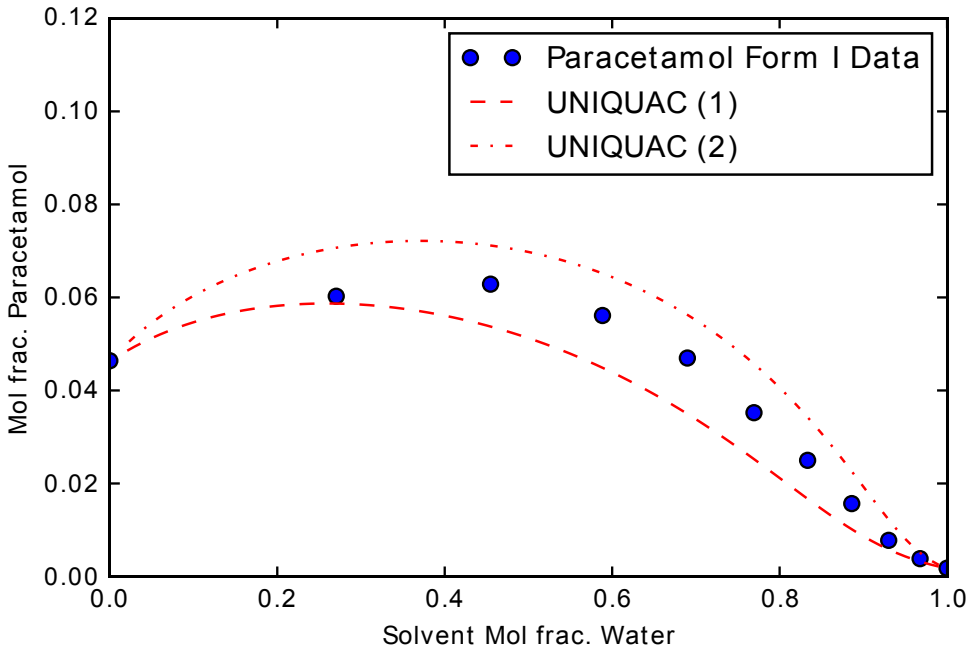

Figure 2.10. *Predicted mixed solvent solubility of Paracetamol in Water – 2-propanol and solubility data[76] at 25 °C. UNIQUAC (1) and UNIQUAC (2) use different water – 2-propanol interaction parameter.*

Similarly, solubility of paracetamol in acetone – water at 25 °C was predicted and compared to data from Granberg & Rasmuson.[68] Acetone – water binary parameters used are from DECHEMA database accessed from the study by Burman & Ström converted to a_{ij}.[74] The prediction results and literature data are shown in Figure 2.11.

Solubility in water rich solvent is captured well. However, as the solubility fit in pure acetone was poor, the solubility in acetone rich solvent is not captured well. While the solubility maximum is at the right solvent composition, the prediction does not follow the nearly five-fold increase in solubility from pure acetone.

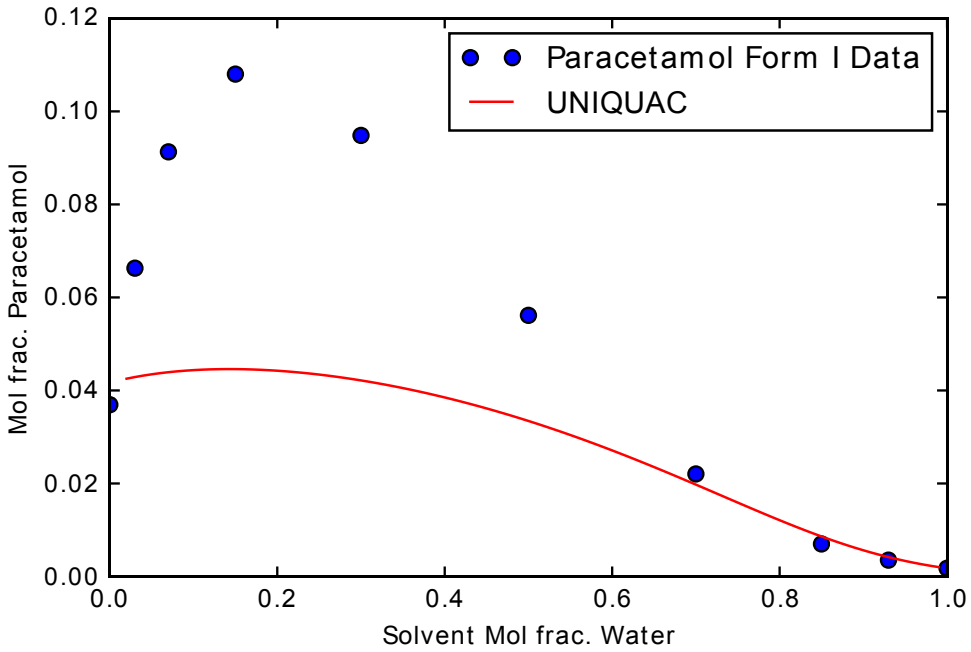

Figure 2.11. *Predicted mixed solvent solubility of Paracetamol in Water – Acetone and solubility data[68] at 25 °C.*

4-aminobenzoic acid solubility in ethanol – water mixtures at 15 °C is available in literature.[77] This was modeled using binary parameters determined here and ethanol – water parameters from Voutsas *et. al* calculated at 15 °C.[75] The resulting comparison is in Figure 2.12. Despite poor fit for solubility in pure ethanol, the mixed solvent solubility fits data well.

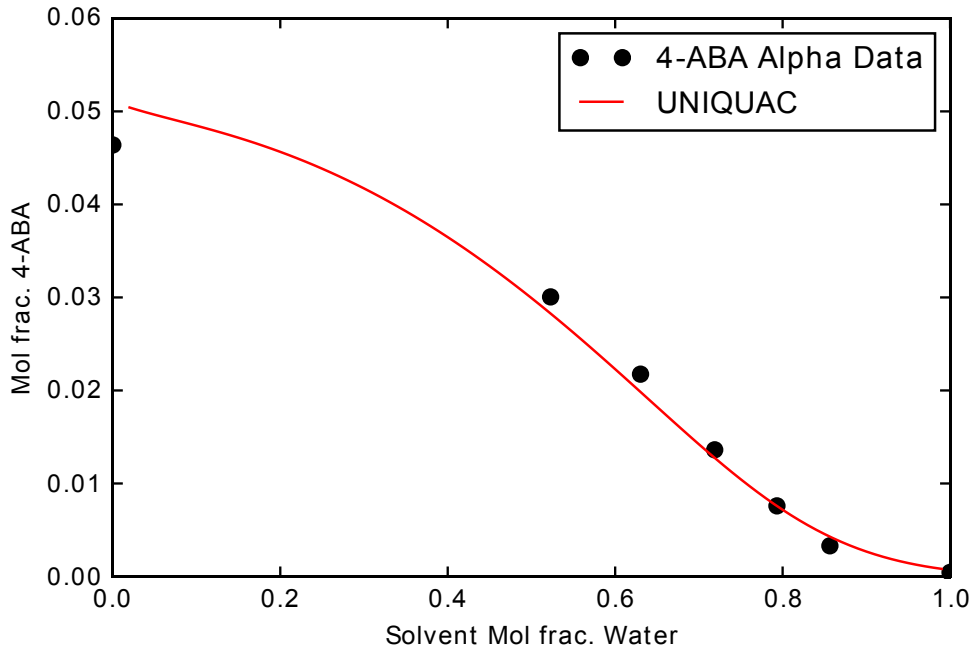

Figure 2.12. *Predicted mixed solvent solubility of 4-ABA in Water - Ethanol and solubility data[77] at 15 °C.*

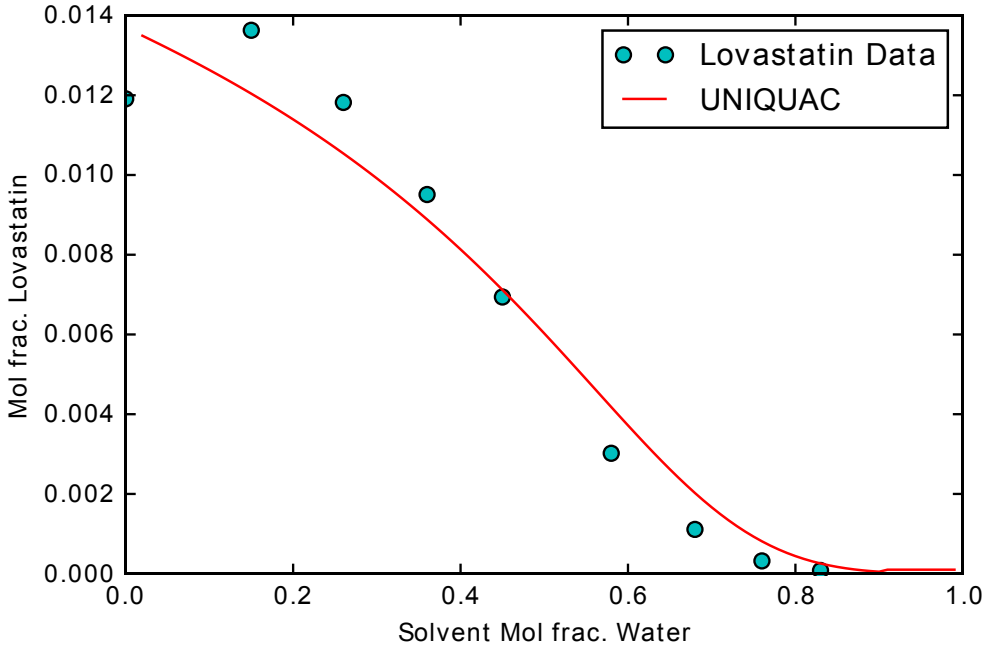

Figure 2.13. *Predicted mixed solvent solubility of Lovastatin in Water - Acetone and solubility data at 25 °C.*

Solubility of Lovastatin in acetone – water solvent mixtures at 25 °C was modeled using fitted parameters and the same acetone – water parameters as used in the paracetamol solubility prediction. The resulting fit is shown in Figure 2.13.

The prediction follows the data relatively well, however, the solubility maximum at 0.2 mol frac. water is not captured. There is also a difference in solubility in pure acetone due to a difference between literature and in-house measured solubility. Since the lovastatin – water parameters were fitted to an arbitrarily low solubility point, the fit in mixed solvent can vary as the solubility curve is sensitive to not only solvent – solvent parameters, but also lovastatin – solvent parameters. Fitting to a single point for any data set may cause several non-unique solutions resulting in parameters with varying accuracy.

While predicting solubility of polymorphs has the potential to be useful given reliable solid phase thermodynamic data, the solubility in mixed solvents is extremely sensitive to the solvent-solvent binary parameters chosen from various valid VLE data sets. This is demonstrated in Figure 2.10 but does not represent the worst case scenario.

2.4.2. CO-CRYSTAL SOLID-LIQUID LINE PREDICTION

The measurement of the eutectic points of the benzoic acid – isonicotinamide co-crystals in ethanol at 25 °C is presented in chapter 3. The thermodynamic properties of the 1:1 co-crystal as measured by DSC are presented in Table 2.9.

Table 2.9. *Thermodynamic properties of 1:1 benzoic acid – isonicotinamide co-crystal.*

ΔH^{fus} (kJ/mol)	T_m (K)
54.6	438.6

These thermodynamic properties have been used to calculate the ideal solubility product of the co-crystal at 25 °C. The value of the ideal solubility product was calculated to be $K_{sp}^{ideal} = 0.000217$. Another constant solubility product calculated from the two surrounding eutectic points from the equilibration method, which is the subject of Chapter 3, was averaged to be K_{sp} = 0.000106. Finally, a constant solubility product from all measured points along the solid-liquid curve was averaged leading to a solubility product of K_{sp} = 8.81x10^{-3}. The resulting solid-liquid curves for the 1:1 co-crystal are shown along with measured points and boundaries from equilibration method in Figure 2.14.

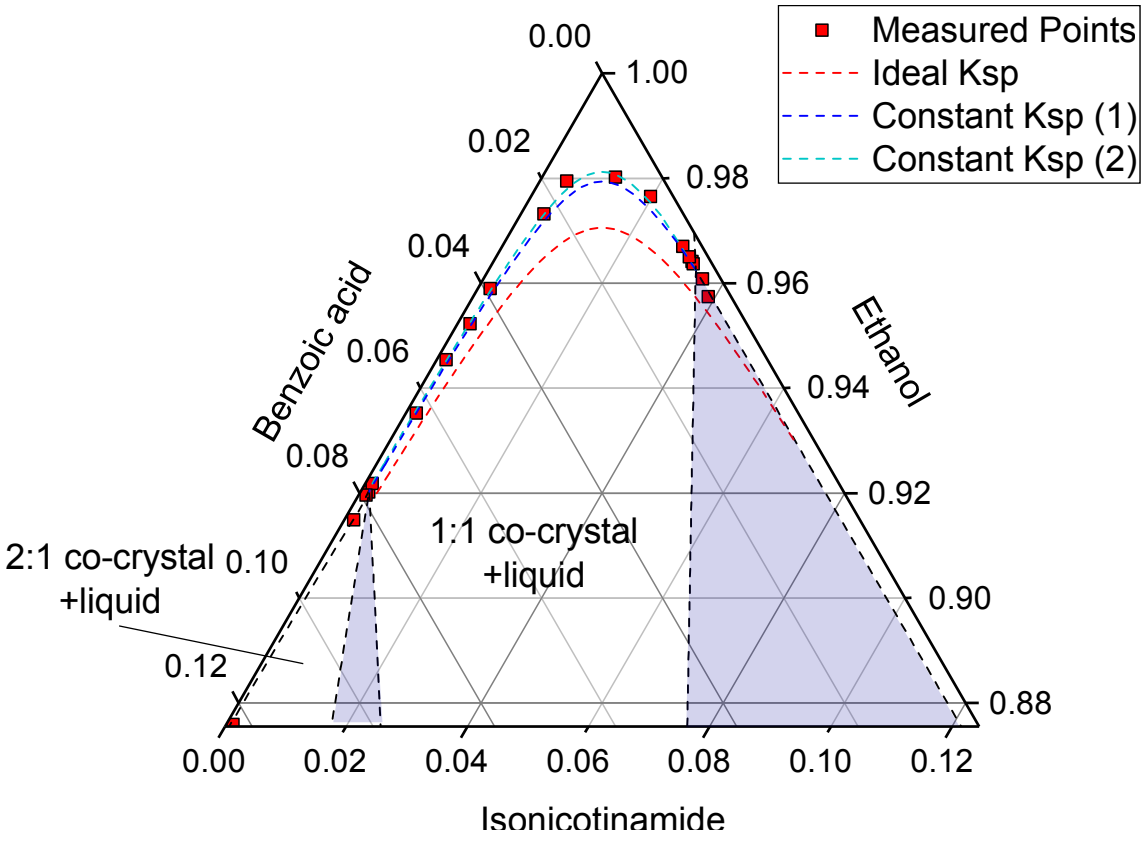

Figure 2.14. *The 1:1 co-crystal solubility line estimated by ideal solubility product (---), constant solubility product averaged from eutectic points (1) (---) and constant solubility product (2) averaged from measured points (---).*

The curve from the ideal solubility product severely overpredicts the solubility of the co-crystal. However, this is to be expected as the effect of solvent is not involved in the calculation. The constant solubility product calculated from the eutectic points provides a significant improvement over ideal solubility. Calculating an average solubility product from all measured liquid phase compositions provides negligible improvement, showing that the estimation of the solubility line just from eutectic points has been sufficient in this case. As the constant solubility product was adequate to estimate the solid-liquid line, a UNIQUAC model was not used. In co-crystal systems with highly non-ideal liquid phase interactions, it is possible that a constant solubility product calculated from the eutectic points will be insufficient to model the solid-liquid line and an activity coefficient model should be used.

2.5. CONCLUSIONS

Semi-empirical approaches have been presented for the determination of various solid-liquid equilibria: solubility of related polymorphs, solubility of compounds in mixed solvents and co-crystal solid-liquid lines. Several new UNIQUAC interaction parameters for pharmaceutically relevant compounds have been determined.

The use of an activity coefficient to model solubility of related polymorphs has been shown to be useful given accurate solid phase thermodynamic properties are available. Solubility in mixed solvents is highly sensitive to the solvent-solvent interaction parameters and has been predicted with reasonable accuracy for most solvent pairs with significant deviations in few cases. Extending parameters from binary mixtures to ternary systems can yield very different results depending on data used. Similarly to single component crystals, the solubility of co-crystals is poorly predicted by assuming ideal solubility.

2.6. CHAPTER 2 NOMENCLATURE

μ^s Chemical potential of solid phase

$\mu^{o,l}$ Chemical potential of liquid face – reference condition

ΔH Enthalpy change (phase transformation) [J/mol]

ΔH^{fus} Heat of fusion [J/mol]

Δc_P difference between liquid and solid heat capacities

ΔG Gibbs free energy change (phase transformation)

ΔS Entropy change (phase transformation)

T Temperature [K]

T_m Melting point [K]

γ Activity coefficient

x Mole fraction

x^{CC} Co-crystal molar composition

ν Stoichiometric ratio

K_{sp} Solubility product

r Surface area UNIQUAC parameter

q Volume UNIQUAC parameter

q' Additional UNIQUAC parameter for water and alcohols

a_{ij} UNIQUAC binary interaction parameter

CHAPTER 3

CO-CRYSTAL PHASE DIAGRAM MEASUREMENT METHODS

3.1. INTRODUCTION

Common approaches to measuring entire phase diagrams by equilibration involve creating a suspension and allowing it to equilibrate while seeding with all potential solid forms. At the end, solid phase is verified by X-ray Powder Diffraction (XRPD) and liquid phase composition determined by High Performance Liquid Chromatography (HPLC).[78,79] There are also calorimetric methods.[80,81] However, these methods can be very time consuming especially with more complex phase diagrams.

Instead of obtaining a full phase diagram, often only the co-crystal solubility is measured to assess potential benefits to a formulation. Co-crystal solubility methods often used apply concepts from single component crystals where the solid liquid phase boundary is measured but the solid phase in equilibrium is not verified at the end.[82] In the case of an incongruent phase diagram, the stable phase will eventually nucleate. As in polymorphic systems, the most stable form in the prepared composition may not be the one that is added or nucleated at the start. This creates a disadvantage for many temperature variation methods for measuring solubility that do not allow monitoring of solid phase throughout. Verifying the solid form is key to determining which solid phase was in equilibrium at the measurement.

This chapter proposes two new calibration-free methods to measure phase diagrams which focus on directly obtaining the eutectic points rather than the full solid-liquid line. By prioritizing the eutectic points, obtaining the location of phase diagram regions can be accelerated with minimum experiments. The solid-liquid line can then be estimated from the points measured using constant solubility

product or activity coefficients based on the measured data. The two methods were applied to measuring the phase diagram of benzoic acid and isonicotinamide in ethanol. This system has been previously studied and the phase diagram reported in literature.[41,83] Benzoic acid and isonicotinamide has been reported to form co-crystals in 2:1 and 1:1 stoichiometries.[41,42] The concepts in these methods can be applied to various isothermal phase diagrams, especially for other multicomponent systems such as solvates, chiral molecules[84] and quaternary systems.

3.2. EXPERIMENTAL

3.2.1. MATERIALS

Benzoic acid (≥99.5%) and isonicotinamide (99%) were supplied by Sigma-Aldrich (Gillingham, UK). Ethanol (99.96%) was supplied by VWR Chemicals (Fontenay-sous-Boius, France). Isonicotinamide supplied was determined to be the stable form II by XRPD.

For the benzoic acid and isonicotinamide co-crystal system, several pieces of information were already available before starting the phase diagram measurements. Pure component solubility benzoic acid in ethanol was available in literature.[85] For isonicotinamide, solubility at 25°C was measured by Mairi Jaap by allowing excess isonicotinamide to equilibrate with ethanol in a 20 mL and measuring the saturated liquid composition gravimetrically after evaporation. Co-crystal compositions and structures have also been previously published in literature.[41,42]

3.2.2. EQUILIBRATION METHOD

Various compositions of benzoic acid, isonicotinamide and ethanol were prepared in 8 ml vials with a magnetic stirrer bar. The solute composition was chosen to be in high excess to increase the probability of hitting the three-phase region while retaining sufficient mixing. The vials did not have to be seeded with the co-crystal for this system as both 2:1 and 1:1 co-crystals nucleate easily, however, for some co-crystal systems, seeding with all potential co-crystal forms is advisable. The vials were sealed and held at 25°C and 1000 RPM for two weeks using a Polar Bear Plus (Cambridge Reactor Design). Vials were weighed before and after the two-week period to check if evaporation of solvent occurred. After the equilibration period, solids were left to settle, and liquid was siphoned from the top and filtered through a 0.2 µm syringe filter into a clean vial. The remaining slurry was filtered using a Buchner funnel to recover solids for XRPD analysis. The combined concentration of both coformers of the liquid phase was determined gravimetrically after allowing all ethanol to evaporate. The residue was analyzed by NMR to determine the solute ratio.

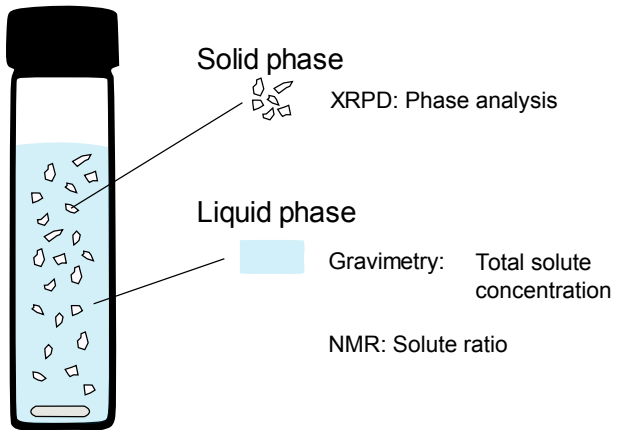

Figure 3.1. *Equilibration method.*

XRPD measurements were carried out from 4 to 35° 2θ with a 0.015° step size and 1 s step^{-1}. Samples were placed on a 28-well plate supported by 7.5 µm Kapton film. Data was collected on a Bruker D8 Advance II diffractometer, source radiation Cu $K_{\alpha1}$ λ = 1.540596 Å. Proton NMR was carried out using Bruker Advance 3 at 400 MHz with four scans on samples dissolved in deuterated methanol in 5 ml tubes.

Liquid phase composition in equilibrium with the determined solid phase(s) was determined by combining the NMR and gravimetry results. XRPD results then show which solid phase was in equilibrium with the calculated liquid composition. If two solid phases were found in XRPD, the liquid composition is at the eutectic. The phase diagram can be plotted if all three-phase regions were successfully targeted and all eutectic points were determined. All additional points in two-phase regions can be used to plot the solid-liquid line of the given region.

3.2.3. SOLUTION ADDITION METHOD

The solution addition method relies on using PAT tools for monitoring liquid and solid phases to detect phase boundaries while adding a solution and moving across a phase diagram. The experimental procedure for this method was carried out in a 100ml Easymax glass vessel (Mettler Toledo). Experimental setup is shown in Figure 3.2. The trajectory starting point composition was weighed out and allowed to equilibrate for several hours. Temperature was controlled at 25°C and agitation of 300-400 RPM. Depending on the direction of the trajectory, solution of isonicotinamide or benzoic acid was prepared in ethanol. The solution was loaded into a syringe and the mass was recorded. Solution was pumped into the vessel via PHD Ultra (Harvard Apparatus) syringe pump at a rate of 1.5-10.0

ml/hr for 4-15 hours. The syringe was weighed again at the end to obtain mass change over time. Liquid phase composition was monitored by UV, 6 mm Hellma ATR probe with Carl Zeiss MCS600 Spectrometer. The benzoic acid characteristic peak appears at around 230 nm, isonicotinamide around 270 nm. The raw UV data was processed using first derivative of the spectrum and the relevant peaks were used to plot concentration trends. The solid phase was monitored by Raman using a Kaiser Optical Systems RXN2 with the PhAT probe with a 250mm spacer and 6mm optic. The raw data was processed using 2nd derivative of the spectrum for baseline correction. Savitzky-Golay smoothing over 10 points and SNV offset correction were also applied. The resulting trends were also smoothed.

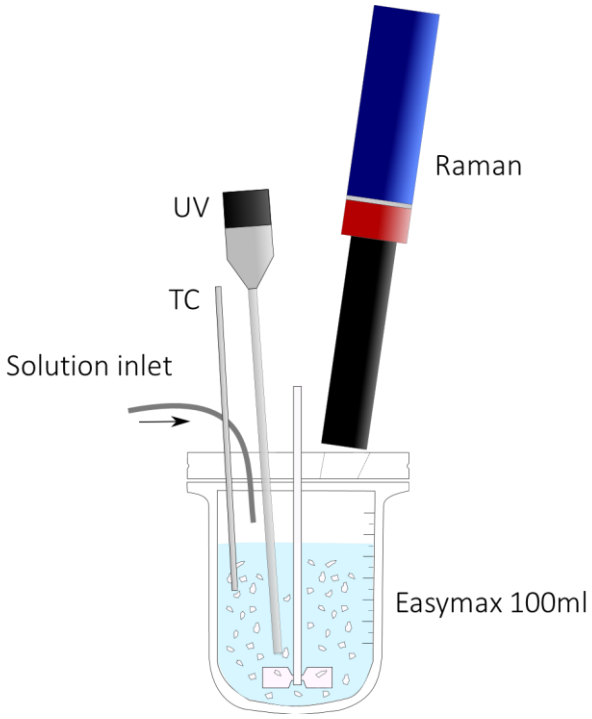

Figure 3.2. *Easymax and PAT setup for solution addition method.*

Both UV and Raman were used calibration free as they were used to detect change rather than absolute quantities. In the setup used, composition was changed by adding a solution to ensure uniform addition, however, if a suitable solid or slurry dosage system is available that can be used as well. The starting point can also be anywhere in the phase diagram with solid present. If the starting point is equilibrated in the three-phase region, no nucleation of new phases is necessary. However, if the starting point is in a two-phase region, there will be a slight lag as the stable phase builds supersaturation before nucleation. One could traverse the entire phase diagram in one trajectory, however, the distance of the trajectory depends on the volume change possible in the setup. With this setup, starting volume was around 50-60 ml with 30-45 ml added via the pump.

The rate of addition influences how close a system is to equilibrium during the experiment. If the addition rate is too fast, the growth and dissolution of present solids will not be able to keep up with the change in composition leading to large errors. For boundaries where a new solid phase must nucleate, pumping too fast will increase the lag time for nucleation. Several addition rates were investigated for trajectories which involve going from two-phase region to three-phase and again to two-phase. The nucleation is caused by the build-up of supersaturation for the co-crystal. In the absence of a stable solid phase, the liquid solubility follows a pseudo-equilibrium line until nucleation. If two addition rates produce different results, the pumping rate needs to be reduced. If they give similar results, the system is close to equilibrium independent of kinetics. Some variation is expected in the two to three-phase transition due to the stochastic nature of nucleation.

Figure 3.3 shows a schematic of an example co-crystal phase diagram with one solvent where 1:1 solid phase exists. Solubilities of pure coformers are represented as blue squares. The shaded regions of the phase diagram denote three-phase regions. Within these three-phase regions, two solid phases are present, but the liquid phase is always at the eutectic composition, denoted by red squares. When moving from a three-phase region in equilibrium to a two-phase region, no nucleation of a new form is necessary to stay near equilibrium, this depends only on growth and dissolution kinetics of the two solids. When starting at point A_1 in equilibrium, two solid phases are present: B and A:B co-crystal. The overall composition is shifted towards A_2 by adding slightly undersaturated solution of A. On that trajectory, between A_1 and A_2, liquid composition is at the eutectic and therefore constant. Only the ratio of solids is changing: crystals of B are dissolving while the A:B co-crystals are growing. The expected trends for both Raman and UV signals are depicted in Figure 3.4 on the left. After crossing the phase boundary A_2, liquid phase composition will change as overall composition is changed along the A:B co-crystal solid-liquid phase boundary. Also, all B crystals will disappear at this point and only the co-crystal is the only present solid phase.

When moving from a two-phase region to a three-phase, crossing the phase boundary depends on nucleation of a new solid phase as well as growth/dissolution of the present solid. Point B_1 is the starting composition in a two-phase region with only liquid and solid B present. By adding a solution of A, the composition shifts towards B_2. While inside this region, liquid composition changes along the solubility curve. The trend of Raman peaks corresponding to

A:B co-crystal will be flat at this point as no co-crystal is present. The expected idealized trend for Raman and UV is shown in Figure 3.4 on the right. Upon crossing of the phase boundary B_2, liquid phase will continue to follow the dashed pseudo-equilibrium solubility line and supersaturation for the co-crystal phase will increase. When the co-crystal nucleates liquid phase will return to the eutectic composition and remain constant while moving through the three-phase region. Raman peaks corresponding to A:B co-crystal will become more visible as the amount of co-crystal in equilibrium composition increases.

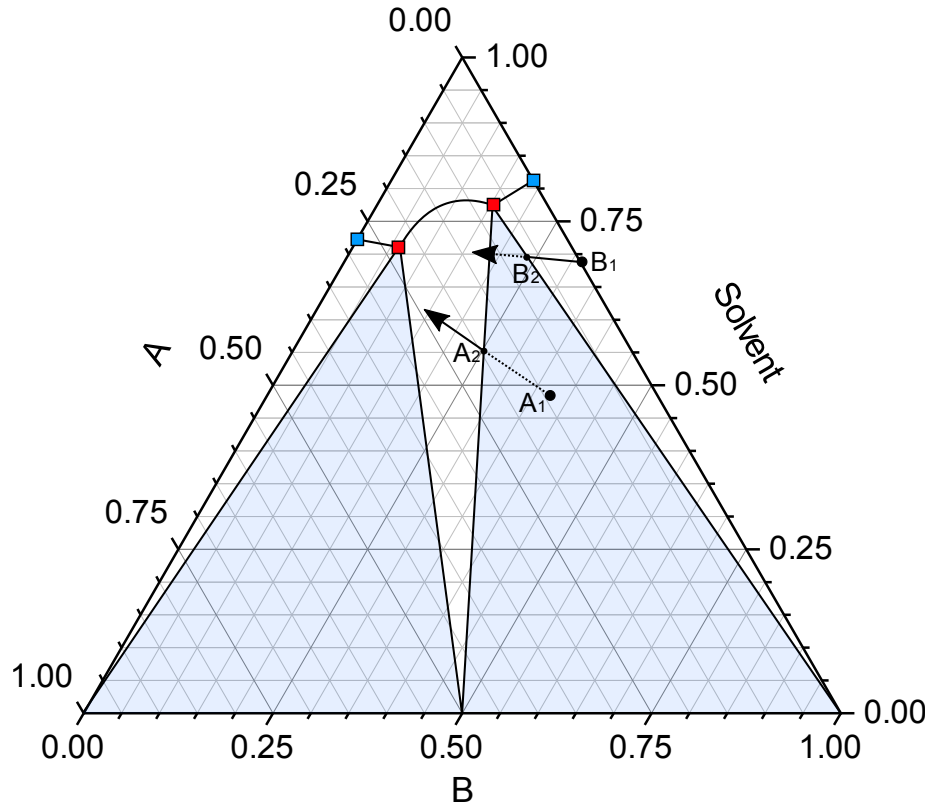

Figure 3.3. *Solution addition method illustration.*

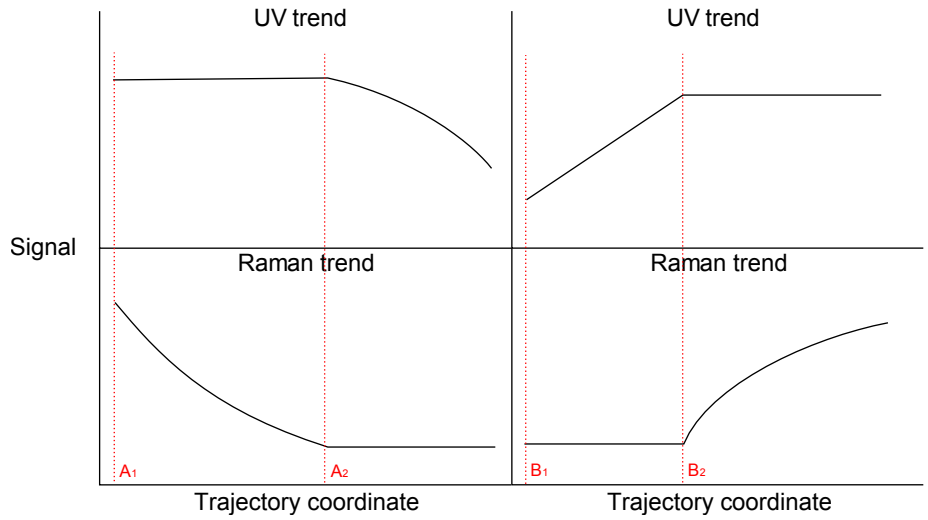

Figure 3.4. *Expected trends from UV and Raman. Shows three to two-phase region transition (left) and two to three-phase region transition (right).*

From the detected solid-solid-liquid phase boundaries, eutectic points can be triangulated by connecting the boundary points to composition of pure solids. The eutectic point location is derived from the intersection point of two lines from adjacent phase boundaries.

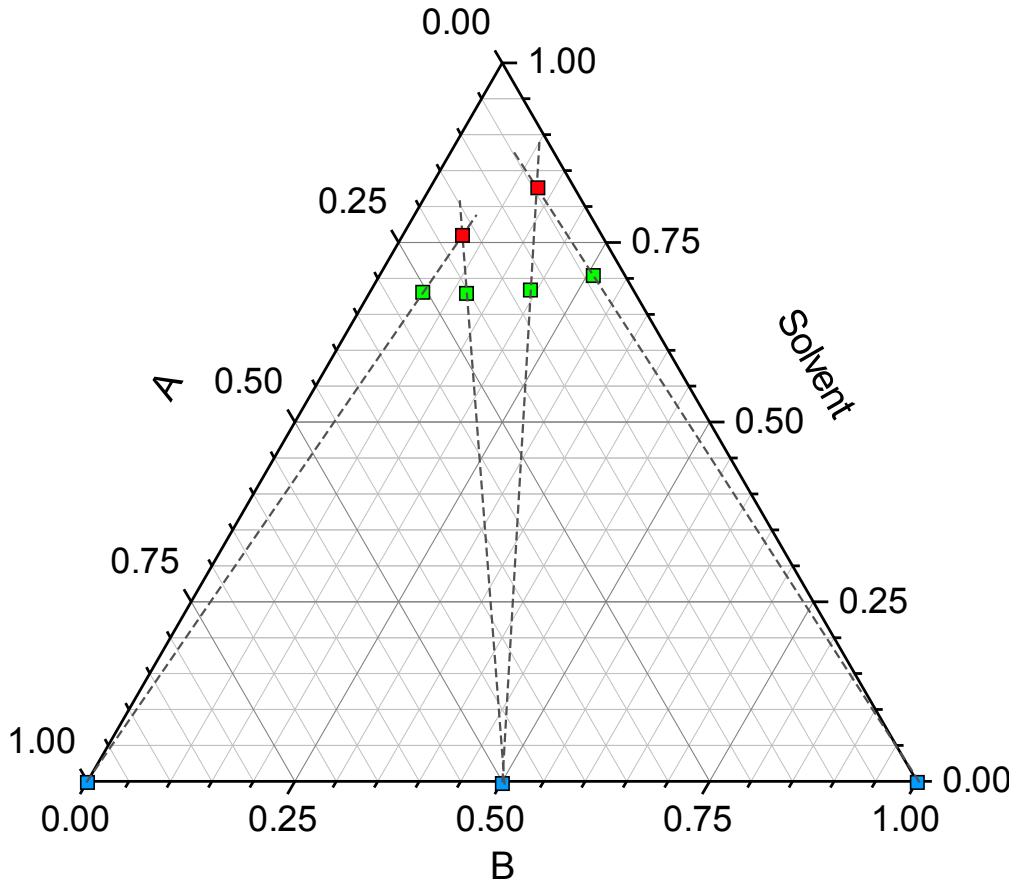

Figure 3.5. *Triangulation to obtain eutectic points from phase boundaries.*

Figure 3.5 shows an illustrative example of this methodology on a simple 1:1 co-crystal system between A and B. Green squares indicate phase boundaries as an example of the kind of data points obtained from the solution addition method. Three blue squares at the base of the ternary plot show compositions of the pure solid phases and the 1:1 co-crystal. The region phase boundary lies along the length of the line connecting the solid phase point and the detected boundary point. The eutectic points are illustrated by red squares where the two adjacent dashed lines intersect.

3.2.4. ESTIMATION OF SOLID-LIQUID LINE FROM EUTECTIC POINTS

The solid-liquid lines can be either measured experimentally using the equilibration method described in section 3.2.2. or approximated from the obtained eutectic points. The comparison of various methods to estimate the solid-liquid line can be found in Chapter 2.

3.3. RESULTS

3.3.1. EQUILIBRATION METHOD

All overall vial compositions equilibrated are shown as circles in Figure 3.6. This is split into solid and liquid phases. The solid phase as identified by XRPD is depicted by shading of the circle. In the cases where multiple solid phases were present in the sample, that circle is shaded with both colors irrespectively of the ratio of the two phases. The corresponding liquid phase as measured by gravimetry and NMR are depicted as squares. If liquid points from starting compositions with multiple solid phases converge, they were deemed as eutectic points, shaded blue. Other liquid points along the two-phase boundary are red.

After determining the location of eutectic points, any missing gaps in the liquidus line were filled in by additional measurements for comparison to constant solubility product estimation, subject of section 2.4.2. in Chapter 2. The liquid points in pure co-crystal regions were connected to the co-crystal composition to create dashed tie-lines.

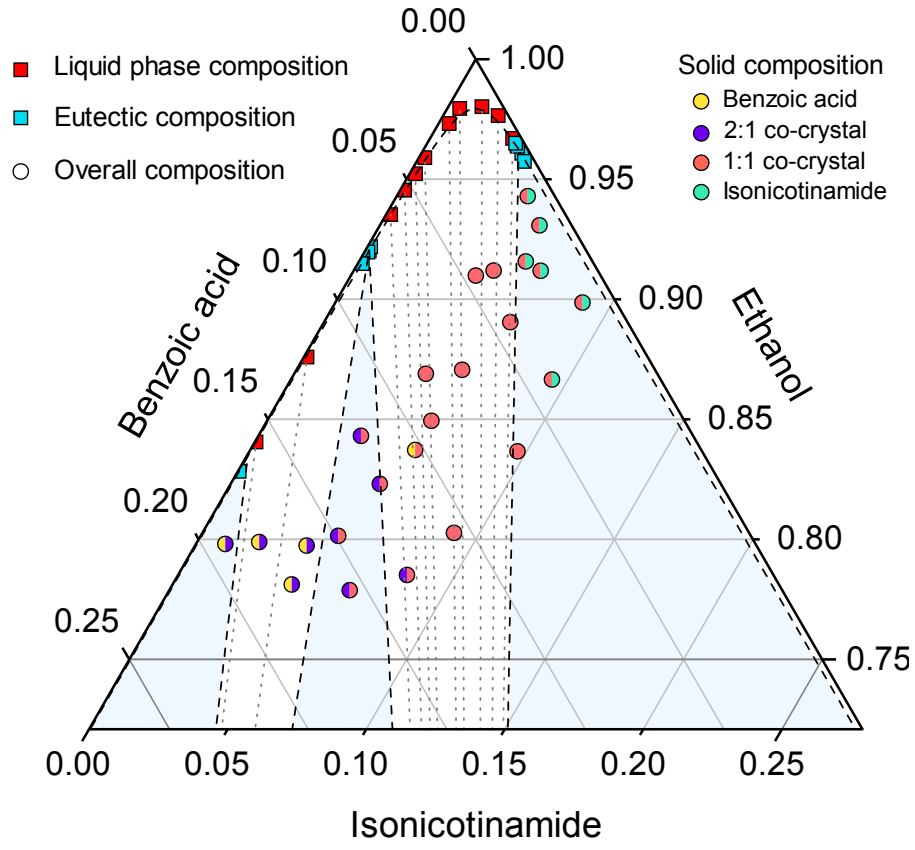

Figure 3.6. *Equilibration results and starting composition.*

Phase boundaries were plotted to connect solid phase composition to the averaged eutectic points. The solid-liquid boundary was estimated using constant solubility product. The solubility product was taken from the two eutectic points surrounding a solid-liquid boundary and averaged. The solid-liquid boundary for the solid coformers was plotted as a straight line between the pure solubility and the eutectic. In this case, the solid benzoic acid and isonicotinamide regions along the sides of the phase diagram are very narrow due to the relatively high stability of the co-crystals. Therefore, the linear approximation of the solid-liquid line for pure solids is probably very close to the actual curve. However, when designing

a co-crystallization process, knowing the shape of this curve is not critical for an optimum solution.

The solid-liquid line estimated from constant solubility product is very close to the actual solid-liquid line measured by this method. In cases where the solubility of the co-crystal deviates from ideality significantly, more sophisticated approaches may be required. Phase diagram measurements using this equilibration method will most likely result in few points in the two-phase solid-liquid region which will assist in drawing the co-crystal solubility line.

The eutectic points from each of the three phase regions are generally closely clustered together showing good agreement. However, there are some unexpected results from solid phase verification. For example, two points in the 1:1 region show traces of benzoic acid and 2:1 co-crystal. Similarly, all points in the 2:1 region show traces of benzoic acid on XRPD. This is most likely due to lack of washing of samples after filtration and high solubility of benzoic acid in ethanol. Washing was avoided to avoid phase transformation but not washing can also introduce introduction of new solid phases upon drying by crystallizing of solute during evaporation of ethanol from saturated solution.

In the 1:1 co-crystal solid-liquid region shown in Figure 3.6, the tie-lines pass through or very close to the overall composition satisfying the mass balance. However, in the 2:1 region the two tie-lines both pass on the left side of the overall composition. This does not indicate that the overall composition lies in the three-phase region however. To be in the BZA-2:1 co-crystal three-phase region, the tie-lines would have to be on the right of the overall composition. Also, the liquid

phase composition does not converge to a eutectic for all of the points with both 2:1 co-crystal and benzoic acid identified in solid phase. The liquid composition relies on NMR to determine the ratio of the two solutes. As the solid-liquid line of the 2:1 co-crystal is extremely close to the benzoic acid – ethanol line, the concentration of isonicotinamide is very low. The error from NMR measurement is exaggerated by this very low ratio of isonicotinamide to benzoic acid leading to higher error in liquid phase composition points along the 2:1 co-crystal solubility curve compared to the 1:1 co-crystal. When applying this method to chiral systems, HPLC with a chiral column may be used.

3.3.2. SOLUTION ADDITION METHOD

Early experiments identified issues with reaching far sides of the phase diagram at extreme composition limits, for example going from benzoic acid – 2:1 co-crystal three-phase region to the two-phase benzoic acid solid-liquid region. The volume change required to traverse to the left while already on the very left side of the diagram increases dramatically. A similar issue occurs on the isonicotinamide side of the phase diagram. Even though the isonicotinamide solid-liquid region is wider than for benzoic acid, the lower solubility of isonicotinamide means composition change requires a larger volume change if only solution is to be added. Composition could be changed by adding both solid and liquid, however, by adding solution composition of uniformity is guaranteed and automation becomes easier. The solution for determining these phase boundaries was to start with slurries of single component solids and add the coformer solution at very slow rate until nucleation of co-crystal phase is detected.

This approach simplifies finding the starting points for the four outer phase boundaries, *i.e.* in regions where only one pure solid phase is present. Starting here, each trajectory can pass through two phase boundaries: first the nucleation of the co-crystal and the second after leaving the three-phase region going into co-crystal solid-liquid region. For the middle two phase boundaries, the starting point may require some trial and error as the phase diagram may be asymmetrical.

First experiments to see the effect of rate of addition were carried out at 10 ml/hr. However, the dissolution and especially the growth of solid phases in the three-phase region was limiting the ability of the liquid phase to stay in equilibrium. The addition rate adequate for keeping near equilibrium to obtain the phase boundary is therefore related to the growth and dissolution kinetics of the solid phases present.

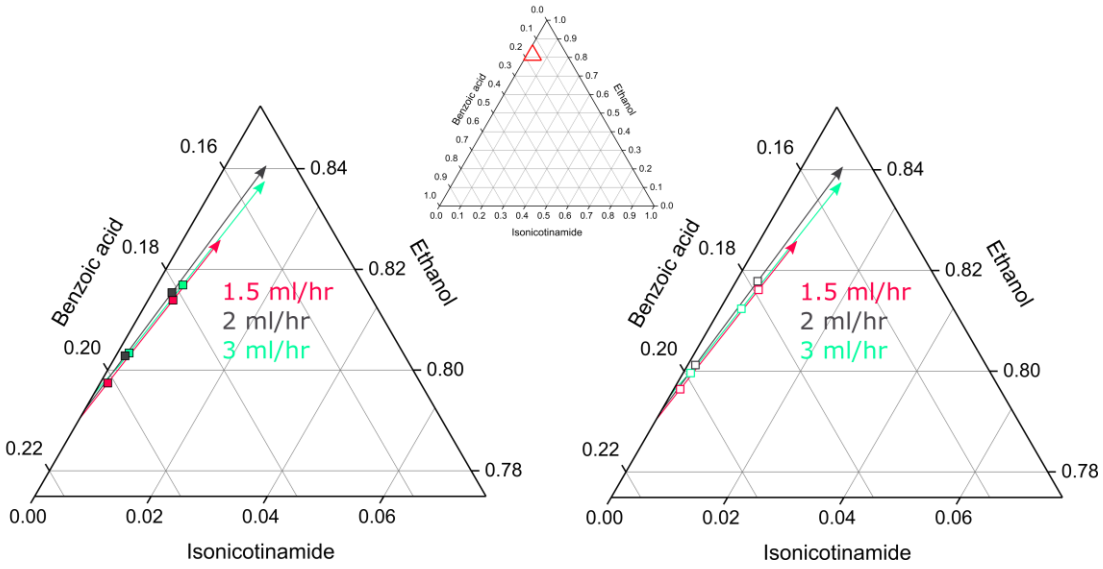

Figure 3.7. *Addition rate comparison. Boundary detection from UV (left) and Raman (right).*

Addition rates of 1.5-3 ml/hr were shown to produce similar results and therefore close to equilibrium. Resulting phase boundaries at three different solution addition rates are shown in Figure 3.7 as squares. The trajectories include a two to three-phase boundary in the first cluster of points as well as a three to two-phase boundary in the second cluster.

Once suitable addition rates and starting points were identified, remaining trajectories shown in Figure 3.8 were carried out to determine all phase boundaries. The composition change inside the 100 ml vessel is shown by the black trajectory lines. Phase boundaries detected by Raman by the appearance or disappearance of certain solid phases are shown by blue squares. Similarly, phase boundaries detected by UV by change in concentrations are illustrated by yellow squares. In most cases, the phase boundary detection points are very close for UV and Raman such that the Raman blue squares and the UV boundary squares overlap. Some repeats were carried out for most trajectories at slightly different starting positions to improve accuracy for the triangulation of eutectic points.

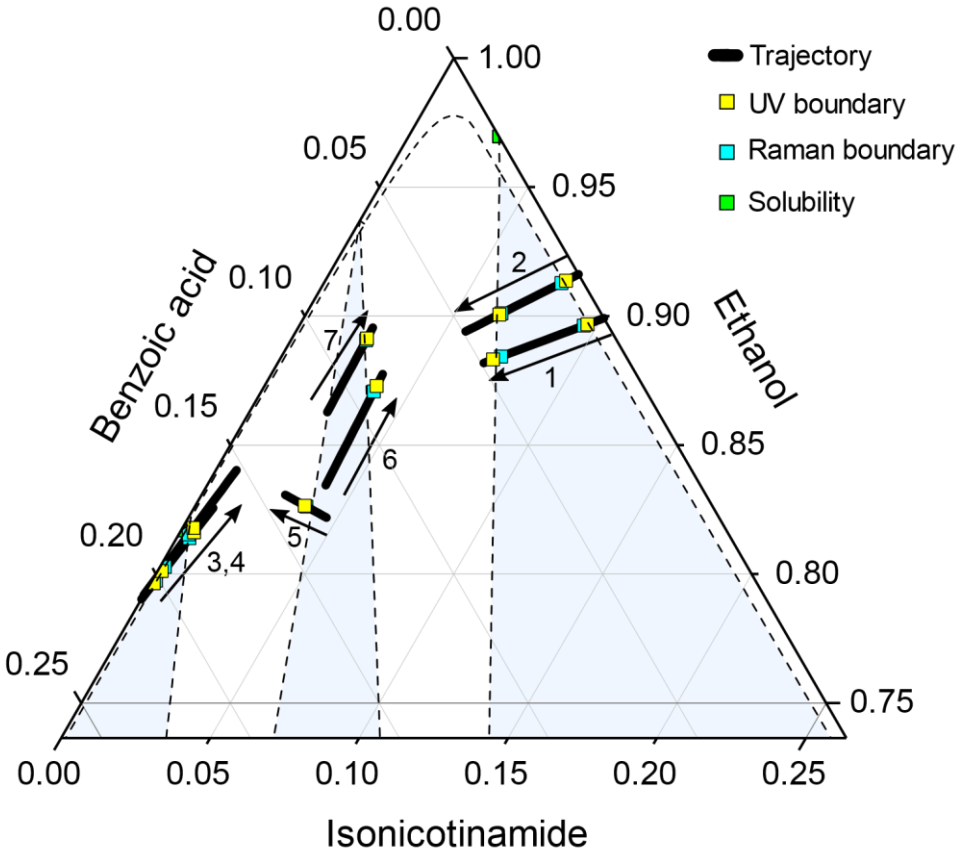

Figure 3.8. *Phase diagram showing all trajectories and the corresponding phase boundaries as detected by UV and Raman. Most Raman points are directly under UV points.*

Phase boundaries were drawn by connecting solid phase compositions with the phase boundary points and extending them until they meet at the eutectic point as described in experimental section 3.2.3., Figure 3.5. If the co-crystal composition was not known, this method could also be extended to find that as well. The phase boundaries detected by both methods coincide well with each other in all cases. In cases where duplicates were carried out, consistency is also achieved. The eutectic point between 2:1 and 1:1 solubility lines lies on the benzoic acid – ethanol line as that was the best fit for boundaries detected from trajectories 5, 6 and 7.

Accuracy of this method depends on PAT detection limits, rate of addition and the proximity of the phase boundary detection point to the eutectic. If the phase boundary is crossed far away from the eutectic, any error in detection limits is leveraged by the triangulation method. On the other hand, sufficient slurry density is required for Raman signal and high surface area for fast growth and dissolution. Solid-liquid lines were drawn assuming constant solubility product which was averaged from the eutectic points, just as was done in the equilibration method.

Figure 3.9 shows example UV and Raman trends over the course of solution addition in trajectory 2 as it shows both two to three-phase and three to two-phase region transitions.

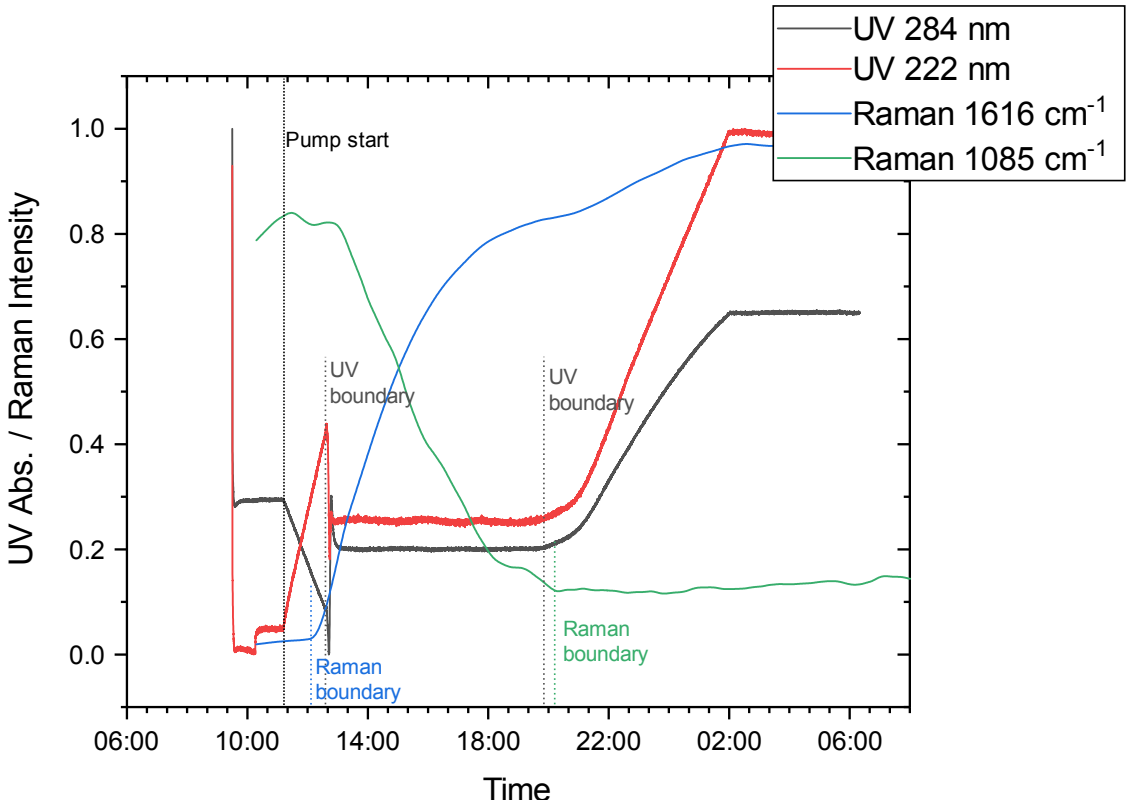

Figure 3.9. *Example UV and Raman trends during solution addition from trajectory 2. UV 222 nm corresponds to benzoic acid spectrum derivative peak, 284 nm corresponds to an isonicotinamide peak. Raman 1616 cm^{-1} corresponds to 1:1 co-crystal solid and Raman 1085 cm^{-1} corresponds to isonicotinamide solid.*

The flat UV line before pump start corresponds to the monitored section of the equilibration period. After solution addition started, UV signal changes along the solubility curve of isonicotinamide while Raman is relatively stable in this section. After some time, the Raman curve corresponding to the 1:1 co-crystal begins to rise indicating that the co-crystal has nucleated. This is labelled as the first Raman boundary. Shortly after, UV changes sharply due to the nucleation indicating a phase boundary as well. For several hours after the first boundary, the UV signal is steady because the system is in the three-phase region and liquid composition is at the eutectic. During this time, the 1:1 co-crystal is growing as demonstrated by the rising corresponding Raman peak while solid isonicotinamide is dissolving, also shown by negative trend in the corresponding Raman peak. When the UV begins to change again, the liquid phase is no longer at the eutectic composition because the system composition is now in the two-phase co-crystal region indicating a phase boundary was crossed. Similarly, when Raman peak corresponding to solid isonicotinamide begins to level off the trend suggests that all isonicotinamide has dissolved and transformed to co-crystal.

3.3.3. COMPARISON WITH LITERATURE

There is good agreement between the results obtained by the two methods. The phase boundaries and eutectic points are shown in Figure 3.10. Equilibration method is shown in black, solution addition method in red. The diagram on the right shows a magnified version of the tip focusing on the position of the eutectic points.

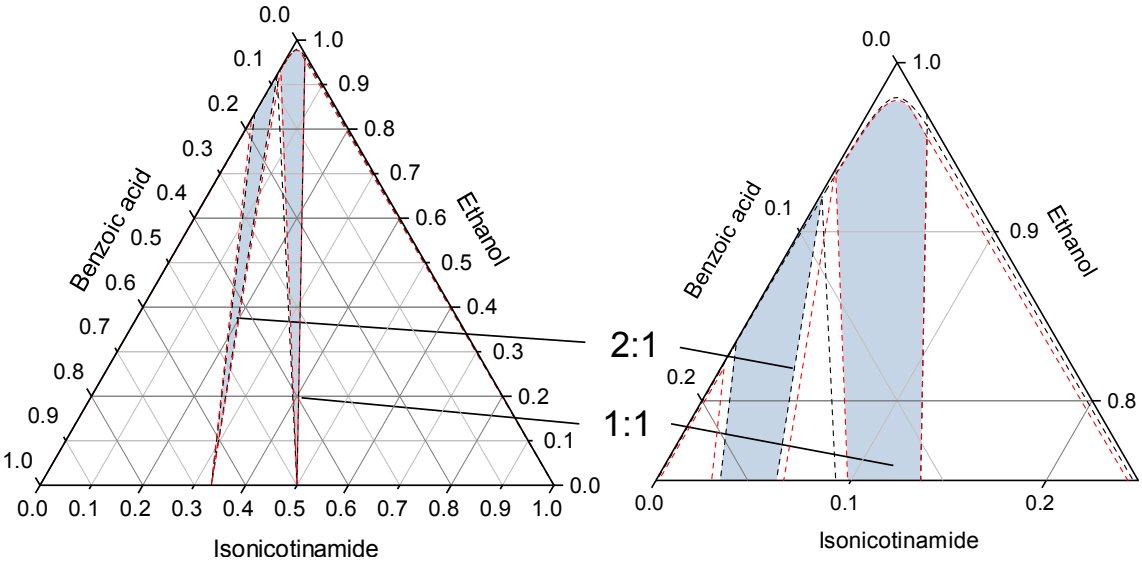

Figure 3.10. *Comparison between equilibration method (black) and solution addition method (red).*

Literature sources with this phase diagram report a similar location of the 1:1 co-crystal region, however, the 2:1 region is either very narrow or missing.[41,83] This may be caused by a composition sweep in the measurement plan passing below or just at the 2:1-1:1 eutectic.

3.4. CONCLUSIONS

The two methods for obtaining eutectic points of a co-crystal phase diagram have been demonstrated on benzoic acid and isonicotinamide in ethanol. While experimentally the equilibration method is similar to what is routinely done in literature, the focus on eutectic points rather than solid-liquid line should accelerate selecting the best solvent in process development. The solution addition method employs a novel approach to phase diagram determination that is easy to automate for rapid screening. It has also been shown that either Raman or UV can be utilized independently for boundary detection, therefore, a smaller setup requiring less material could be used. With some modification, these

methods may be applicable to other multicomponent systems such as those involving solvates, solid solutions, salts and chiral molecules.

The solid-liquid line estimation from constant solubility product has been consistent with the measured data in this case, allowing the construction of the complete phase diagram. In the case of less ideal systems, activity coefficient models may be utilized. The combination of all available experimental data with thermodynamic models can accelerate the process of determining an accurate phase diagram and guide future measurements.

CHAPTER 4

CONTINUOUS CO-CRYSTALLIZATION

4.1. INTRODUCTION

Several methods for manufacturing co-crystals have been previously reported including both dry powder processes and solvent based processes, typically in batch processing mode. Dry powder processes are mechanochemistry based and utilize grinding at room temperature[86] or cryo-temperatures,[87] polymer assisted grinding,[88] high shear granulation[89] or hot melt extrusion.[90] Co-crystals from solution-based processes have been reported from evaporative and cooling[91], antisolvent[92] or reactive crystallization.[93] Cooling co-crystallization has previously been implemented in continuous platforms[94,95] and with co-crystal stoichiometry control.[95] Co-crystallization using antisolvent has been previously studied in batch processes,[92] but not using continuous methods. Antisolvent crystallization of single component materials has been shown to be adaptable to continuous manufacturing and scale up in a number of processes.[96–98] Reactive co-crystallization mentioned in the work of Rodríguez-Hornedo *et al.*[93] does not involve a chemical reaction as such but a solution-based formation of a multicomponent solid phase from a mixture of two solutions undersaturated with respect to individual components using the same solvent.

Processes which rely on mixing to induce supersaturation such as reactive and antisolvent crystallizations, are well amenable to scale-up under continuous conditions.[99] Since mixing can have strong impact on generation of supersaturation profile and subsequent nucleation, especially under kinetically controlled conditions,[100] well-controlled mixing is essential for a control over final crystal properties, such as solid form and particle size distribution.

Antisolvent and reactive crystallization approaches can be combined in order to design a process where supersaturation is induced by mixing and is determined by the position in a quaternary phase diagram involving two crystal coformers and two solvents. Depending on the shape of the phase diagram, which often shows a highly unsymmetrical nature,[101] the co-crystal would be the thermodynamically most stable phase under some conditions. However, sometimes it may not be readily crystallized due to kinetic limitations (slow nucleation or growth) even if thermodynamically favored. Munshi and co-workers pointed out opportunities to use mixed solvents in controlling solid phase outcomes in cooling co-crystallization.[102] Solvent selection, a key design choice in crystallization, becomes more challenging in multicomponent systems. The key parameter of co-crystallization process design is the supersaturation with respect to the co-crystal phase, rather than the supersaturations of the individual coformers. While having four components increases the complexity of mapping the phase diagram, it also allows for more options how to access solid phase regions which might not be easily accessible at a fixed solvent composition. For example, it may be possible to start with a solution of both coformers undersaturated in one solvent and add a second solvent to induce supersaturation, as in antisolvent crystallization. Alternatively, one can start with one coformer undersaturated in a given solvent mixture, and the other coformer undersaturated in the same solvent mixture and generate supersaturation by mixing these two solutions together, as in reactive crystallization. These decisions will be driven by the shape of the phase diagram and the nature of the target solid phase.

This chapter combines antisolvent and reactive crystallization concepts to develop a continuous co-crystallization process to produce benzoic acid (BZA)−isonicotinamide (INA) co-crystals. In this study, benchtop screening crystallization experiments were scaled to run in a continuous process. A Design of Experiments was carried out for the benchtop screening to better understand the effects of different process conditions on the crystallization of the two cocrystal phases. DoE screening was done in order to cut down the time and number of experiments to find suitable continuous crystallization conditions to selectively produce either 1:1 or 2:1 cocrystals by continuous crystallization.

4.2. METHODOLOGY

4.2.1. MIXING INDUCED SUPERSATURATION CONCEPT

Mixing induced supersaturation in crystallization leverages some inherent properties of continuous manufacturing that in this case allow for a structurally pure solid by reaching a specific region of a phase diagram through rapid intensified mixing. The figures below demonstrate different modes of inducing supersaturation through mixing of two solutions. Figure 4.1 shows how antisolvent crystallization may be used to induce supersaturation for a co-crystal. The left phase diagram shows the phase regions in a solvent, where all solid phases have a relatively high solubility, indicated by the large liquid phase region. On the right is a phase diagram where the solvent has been replaced by antisolvent, a solvent where all solid phases are poorly soluble. Both coformers and the co-crystal show similar behavior in this case and both phase diagrams

are congruent. A co-crystal can be crystallized by starting in the middle of the phase diagram on the left, close to the co-crystal solid-liquid line and adding antisolvent. If the decrease in solubility is more substantial than the dilution effect, the co-crystal phase will become supersaturated. This mimics antisolvent crystallization process of a single component solid. The challenge is finding a solvent system, where the solubility of all solid phases, including the co-crystal, behave in the same way in the solvent/antisolvent pair. This method also requires the knowledge of the quaternary phase diagram, which makes solvent pair screening a time-consuming task.

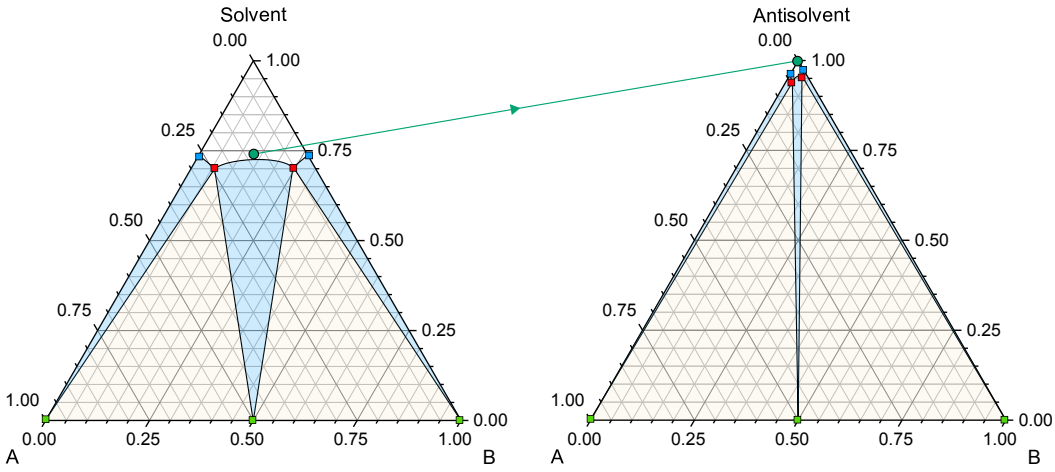

Figure 4.1. *Antisolvent co-crystallization.*

Another approach for generating supersaturation by mixing two solutions is reactive crystallization. This process is illustrated on an example phase diagram in Figure 4.2. In reactive crystallization, two undersaturated solutions, each containing a single coformer in the same solvent mixture, are mixed to supersaturate with respect to a desired co-crystal solid. This is shown by the tie-line between two green points as it passes through the solid-liquid region

containing co-crystal solid. This approach is straightforward but relies on the co-crystal phase having relatively low solubility compared to the coformers in the chosen solvent which may not always be the case. The co-crystallization yield is also determined by the ratio of solubilities of the coformers to the co-crystal.

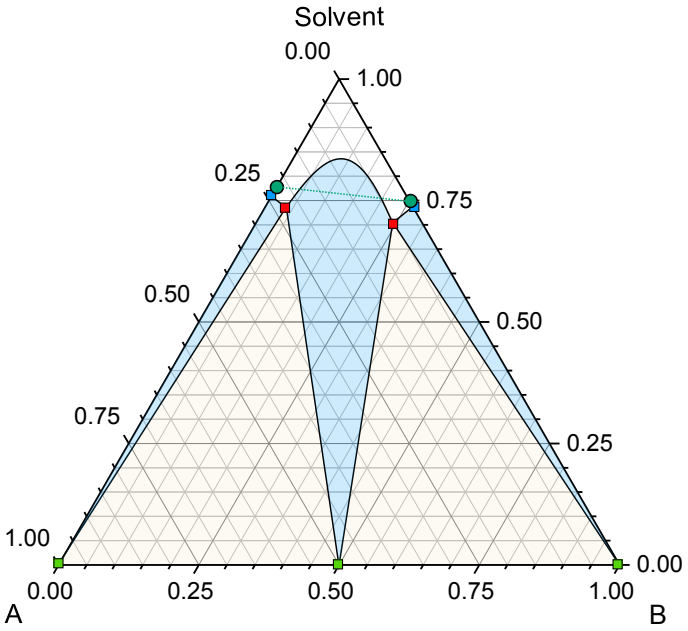

Figure 4.2. *Reactive co-crystallization.*

For co-crystal systems, where it is challenging to find a suitable solvent system for either antisolvent or reactive crystallization to achieve the target co-crystal with desired yield, it is possible to combine the two methods. Figure 4.3 illustrates such an approach, where each coformer comes from a different solvent. This allows for many more potential solvent pairs than reactive or antisolvent methods alone and for greater flexibility in reaching the desired phase diagram region. In the example shown, each coformer has the opposite solubility trend for either solvent. Coformer A has low solubility in Solvent 1, but high in Solvent 2. Coformer B has the reverse relationship, high solubility in Solvent 1 and low in Solvent 2.

This results in incongruent phase diagrams in pure solvents and allows for the system to reach a relatively high concentration with respect to each coformer. This asymmetry allows for a higher chance of reaching the desired co-crystal region, if it is stable in the selected solvent mixture.

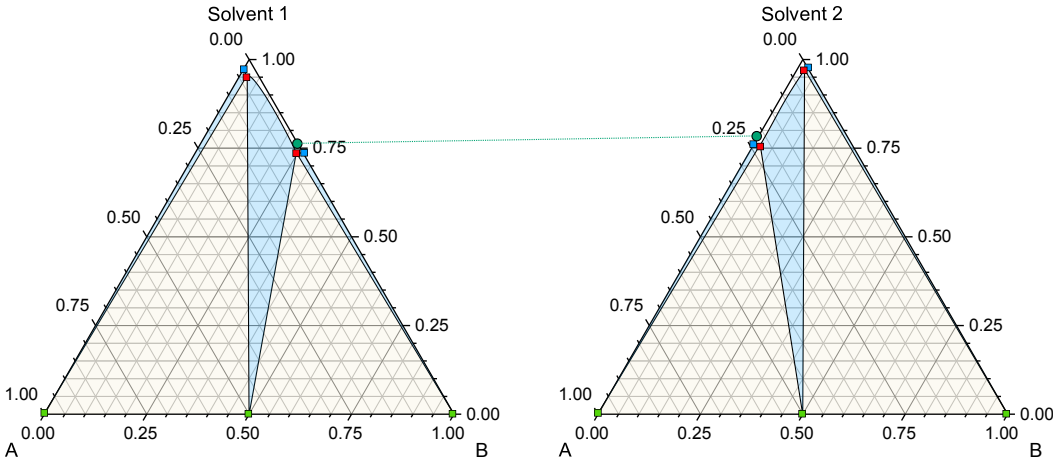

Figure 4.3. *Combined reactive and antisolvent co-crystallization.*

The example approach above can be tested by knowing only the pure component solubilities in single solvents. While the quaternary space between the two solution starting points may be unknown, the high concentration of coformers ensures a high probability that the target region lies between them.

4.3. EXPERIMENTAL

4.3.1. MATERIALS

Benzoic acid (≥99.5%), isonicotinamide (99%), and ethanol (≥99.8%) were supplied by Sigma-Aldrich (Gillingham, UK). Deionized water was produced using an in-house Millipore Milli-Q system.

4.3.2. BATCH SCREENING

Two sets of screening experiments were carried out. The first was an initial screening and the second was a systematic full factorial Design of Experiments (DoE) approach used for mapping of a limited region of the quaternary phase diagram (BZA, INA, Water, Ethanol) in order to identify suitable operating conditions for continuous crystallization. For both sets of screening experiments, an aqueous solution of isonicotinamide was added to an ethanolic solution of benzoic acid in a 20 mL vial, illustrated in Figure 4.4. These solvents were chosen based on pure component solubilities from chapter 3. Solutions were mixed at various ratios to obtain the total of 10 g of solution and agitated using magnetic stirrer bar for 10 minutes past observed nucleation. All experiments were carried out at 25°C.

For the initial screen, solutions of isonicotinamide in water and benzoic acid in ethanol were prepared at concentrations of 68.1 g/kg water and 213 g/kg ethanol, respectively, and mixed in ratios of 2:1, 1:1, 1:2, 1:4 and 1:9 by mass. The solid product obtained was filtered using 0.2 μm PTFE filter without washing, dried at 40°C for 24 hours and analyzed by X-ray powder diffraction (see solid characterization section). The design space for DoE was selected based on

information from the initial screen. The experimental plan was created using MODDE (Umetrics) in a 2-level full factorial design. The experimental worksheet, model fitting and results analysis was all carried out in MODDE. Data were fitted using Partial Least Squares (PLS). The three variable parameters chosen for the DoE were: BZA-Ethanol solution concentration, INA-Water solution concentration, and the mass ratio of the two solutions mixed. Values of these three parameters combined determine the final composition of the mixture and thus the position on the phase diagram. The responses measured were induction time, solid yield, solid phases present and resulting slurry flow properties. Induction time was estimated as time after mixing until first particles were visually observed. Solid yield was taken as a percentage of total solute that was recovered as solids by filtration 10 minutes after the estimated induction time while agitating. Slurry flow was assessed by a rating system where a number was assigned on a scale from 1 to 5: 1 for an easily flowing mixture and 5 for a slurry too thick to flow with gravity. Solid phase was determined by XRPD (see solid characterization section). Based on this DoE, conditions to produce 2:1 co-crystal were selected. Although the initial DoE was aimed to find suitable conditions for crystallization of both co-crystal forms, conditions leading to crystallization of 1:1 co-crystal resulted in solid loadings which would be too high for a continuous operation. Based on results from the initial DoE, a set of further experiments was carried out in an expanded design space to find suitable conditions for crystallization of 2:1 co-crystal. These experiments were carried out at lower solution concentrations and resulting solid phases, induction times and slurry flow ratings were determined in the same way as in the initial DoE runs.

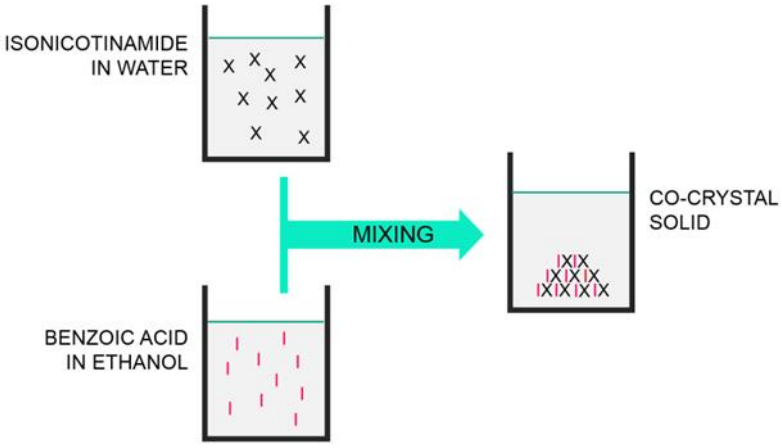

Figure 4.4. *Solvent system used for mixing-induced co-crystallization.*

4.3.3. SOLUBILITY MEASUREMENT

Solubility of the 2:1 co-crystal has been determined by a solvent addition method in the Crystalline Reactor System (Technobis), similar to a previously published procedure.[16] Unlike temperature variation or gravimetric methods, solvent addition relies on slow dilution of a suspension with a solvent (mixture) of a given composition under isothermal conditions until complete dissolution occurs, when a clear point can be detected. Solvent was added at a constant rate using PHD Ultra syringe pumps (Harvard Apparatus) to the Crystalline vials. The solubility measurement setup is shown in Figure 4.5.

Figure 4.5. *Technobis Crystalline and syringe pumps for solubility determination using the solvent addition method.*

Multiple addition rates were tested (0.5 ml/hr and 0.75 ml/hr) to verify that dissolution kinetics have a negligible effect on the result at the addition rates used. Clear point was determined using both transmissivity measurement and images from the Crystalline camera. Image analysis produced more consistent results, which is in line with previous findings from Reus *et al*.[16] A study was also carried out to monitor the solid state transformation of the co-crystal in order to check phase stability in the same setup. Suspensions with concentrations as used for the start of solubility measurements were held for varying amount of time from 1 to 5 hours, after which the remaining solid was filtered, dried and analyzed by XRPD.

4.3.4. CONTINUOUS CRYSTALLIZATION

Continuous crystallization runs were performed using a concentric capillary mixer (Figure 4.6) as well as the Ehrfeld modular micro-reactor system equipped with Valve Mixer 30 module (Figure 4.7).

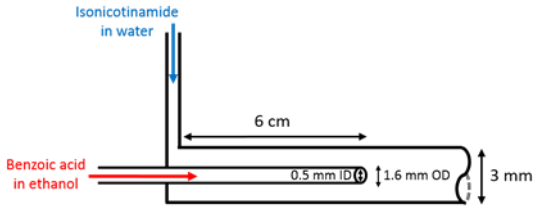

Figure 4.6. *Concentric capillary mixer diagram with dimensions indicated.*

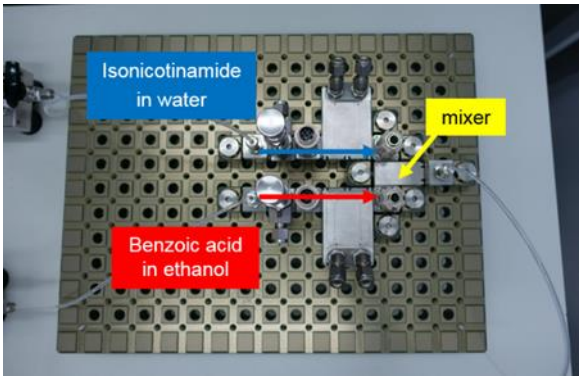

Figure 4.7. *Ehrfeld modular micro-reaction system fitted with valve assisted mixer 30.*

The BZA-Ethanol solution was supplied to the concentric capillary mixer through the inner PEEK capillary, while the INA-Water solution was fed to the outer glass tube as shown in Figure 4.6. The capillary has internal and outer diameters of 0.51 mm and 1.59 mm respectively. The outer glass tube has an internal diameter of 3 mm. The capillary stream entered the outer tube stream 6 cm from the T-junction. The feed solutions were pumped using Bronkhorst Mini CORI-FLOW system coupled with gear pumps allowing for accurate control of mass flow rates. The resulting slurry from the mixer was sampled 0.7 m from the mixing point at the start and end of experiments. Collected slurry was filtered after a holding period in a Buchner funnel with a 0.45 µm filter paper and dried overnight at 40°C. The slurry holding time without agitation was 10 minutes for 2:1 co-crystal runs,

and 18 minutes for 1:1 co-crystal run. A camera was used for visual analysis of any fouling in the glass tube. Temperature of both streams was measured throughout experiments and it varied less than 2°C from 25°C. The total mass flow rates through the capillary mixer were 20, 40 and 60 g/min in 50:50 (w/w) ratio for producing the 2:1 co-crystal and 115 g/min at a 15:100 (w/w) ratio of benzoic acid solution flow rate to isonicotinamide solution flow rate for the 1:1 co-crystal. The relationship between solution concentration and final solid composition depends on the shape of the solid-liquid tie-lines, *i.e.* 50:50 ratio in solution does not necessarily produce the 1:1 co-crystal as is the case here. To demonstrate the transferability of the process to a commercial platform, the Ehrfeld modular micro-reaction system, shown in Figure 4.7, was used at the total mass flow rate of 20 g/min for producing the 2:1 co-crystal.

4.3.5. SOLID CHARACTERIZATION

Filtered and dried crystalline powder from the screening and continuous experiments was analyzed by X-ray Powder Diffraction (XRPD) and IR spectroscopy. Samples from continuous runs were further analyzed by Differential Scanning Calorimetry (DSC) paired with Thermogravimetric Analysis (TGA), and microscope image analysis for particle size measurement. Solids from continuous runs targeted to produce the 2:1 co-crystal were also analyzed by NMR. XRPD fingerprinting was performed on a sample placed in a 28 well plate, supported by Kapton film (7.5 μm thickness). Data were collected on a Bruker AXS D8 Advance transmission diffractometer equipped with θ/θ geometry, primary monochromatic radiation (Cu K$\alpha 1$ λ = 1.54056 Å), a Braun 1D position sensitive detector, and an automated multiposition x–y sample stage. Data were

collected from 4 to 35° 2θ with a 0.015° 2θ step size and 1 s step^{-1} count time. FT-IR measurements were taken using Bruker Tensor II, using 32 scans with 4 cm^{-1} resolution from 450 to 4000 cm^{-1} with diamond tip ATR sampling plate. DSC/TGA data was obtained from Netszch STA 449 F1 Jupiter. Measurements for DSC/TGA were taken from 20 to 180 °C with a ramp of 10°C/min. For Particle Size Distribution (PSD), image analysis was carried out on dry powder using Malvern Morphologi G3 using low pressure dispersion and 2.5x optics. ^{1}H and ^{13}C NMR analysis was carried out using Bruker Advance 3 at 400 MHz by dissolving the solid product in deuterated DMSO in 5 mm NMR vials.

4.4. RESULTS

4.4.1. MIXING-INDUCED SUPERSATURATION

A case study on benzoic acid – isonicotinamide co-crystallization presented here explores the space between reactive and antisolvent crystallization concepts in generating mixing-induced supersaturation to target specific solid phases of co-crystals. Phase diagrams for the system investigated here in various solvents have been previously measured.[41]

An initial screen was used to determine design space boundaries and was followed by a detailed DoE driven screen to map a design space corresponding to a region of interest in the phase diagram. XRPD from the initial screen has shown that the method of mixing solutions of isonicotinamide in water and benzoic acid in ethanol can produce both 2:1 and 1:1 co-crystals. DoE responses were chosen as key outcomes relevant for development of a continuous crystallization process. High solid loadings at the end of experiments limited

solution concentrations from above, as too high solid loadings could lead to downstream blockages. On the other hand, long induction times limited solution concentrations from below, as relatively rapid nucleation is desirable. Due to the probabilistic nature of primary nucleation, induction time estimates from batch experiments are only intended to give an approximate guide, nevertheless there was a good consistency among repeated experiments.

Table 4.1. *Design of Experiments sheet showing the investigated variables in blue and responses in green.*

Run Order	Solution ratio w/w	BZA Concentration g/kg solvent	INA Concentration g/kg solvent	Yield %	Cocrystal Phase	Slurry Flowability (1-5)	Induction time (s)
1	0.25	109.4	48.5	35.84	1.5*	4	4
2	1	109.4	48.5	18.50	2	2	260
3	0.25	164.1	48.5	43.97	1.5*	5	4
4	0.625	136.8	67.9	40.98	2	5	8
5	0.25	109.4	87.3	40.39	1	4	7
6	0.25	164.1	87.3	56.05	1	4	4
7	0.625	136.8	67.9	53.56	1.5*	5	9
8	1	164.1	87.3	44.31	2	4	10
9	1	109.4	87.3	28.53	2	3	29
10	1	164.1	48.5	37.92	2	3	15
11	0.625	136.8	67.9	37.92	2	5	15

*1.5 Co-crystal phase refers to a mixture of 2:1 and 1:1 co-crystals

Despite not necessarily providing direct information on phase stability under thermodynamic equilibrium conditions, the DoE mapping provided a rapid way to find potentially suitable crystallization conditions while also giving indication about kinetics. Contour plots displayed in Figure 4.8 show responses at a fixed solution ratio where at higher concentrations of starting solutions the yield is higher, slurry

flow rating diminishes due to higher solid loading and induction time decreases due to higher supersaturation.

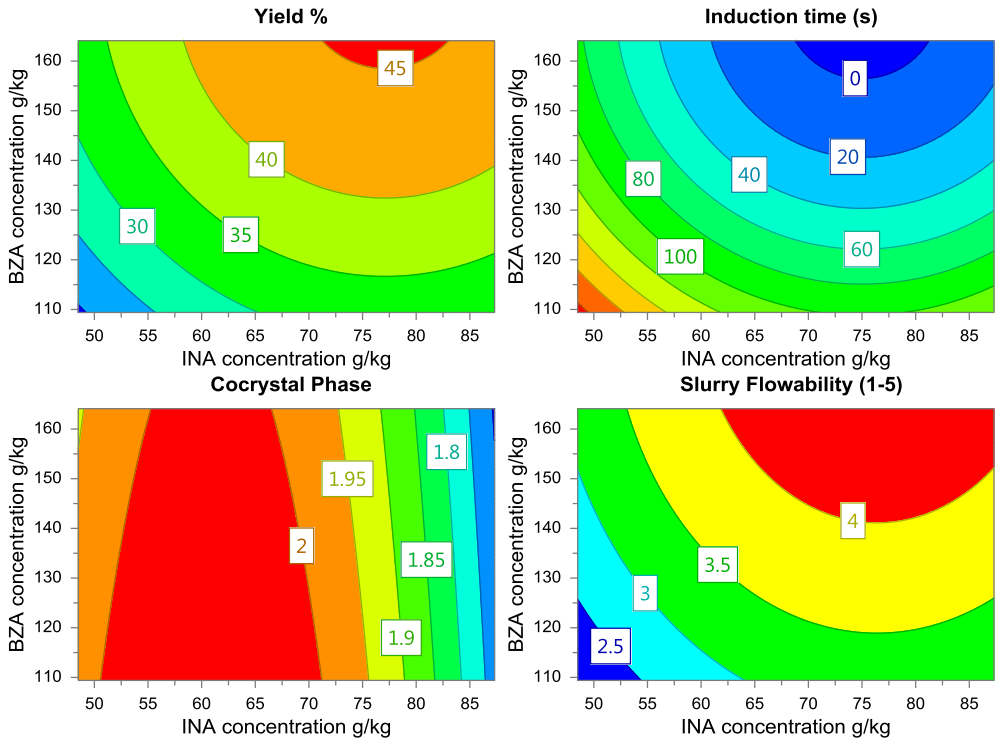

Figure 4.8. *Contour plot showing responses from the Design of Experiments at a fixed solution ratio of 50:50 (w/w).*

The co-crystal phase formed is primarily dependent on the solution flow ratio rather than the solution concentrations within the design space investigated. After targeting the desired phase by adjusting the solution flow ratio, slurry flow ratings of 2-3 were deemed as acceptable for a continuous crystallizer. The induction time model prediction is the least reliable as can be expected for a probabilistic process. The design space selected was large enough to find suitable conditions for the crystallization of the 2:1 co-crystal, while the conditions to crystallize the 1:1 co-crystal phase had to be extrapolated and subsequently validated. The extrapolation was done by choosing various concentrations of initial solutions

outside of the original design space and analysing the same response parameters. The conditions from the DoE chosen as most suitable to produce the 2:1 co-crystal are 50/50 w/w solution flow ratio, with the solution concentrations of 109.4 g BZA/kg ethanol and 48.5 g INA/kg water. For the 1:1 co-crystal the optimal conditions were the solution flow ratio of 15:100 w/w (benzoic acid solution to isonicotinamide solution) with the solution concentrations of 30 g BZA/kg ethanol and 40 g INA/kg Water.

4.4.2. SOLUBILITY

During the phase stability test, the 2:1 co-crystal began to transform to the 1:1 co-crystal over time at the crystallizer outlet conditions. Transformation commenced between 158 to 264 minutes in an isothermal stirred environment as detected by XRPD, see Figure 4.9.

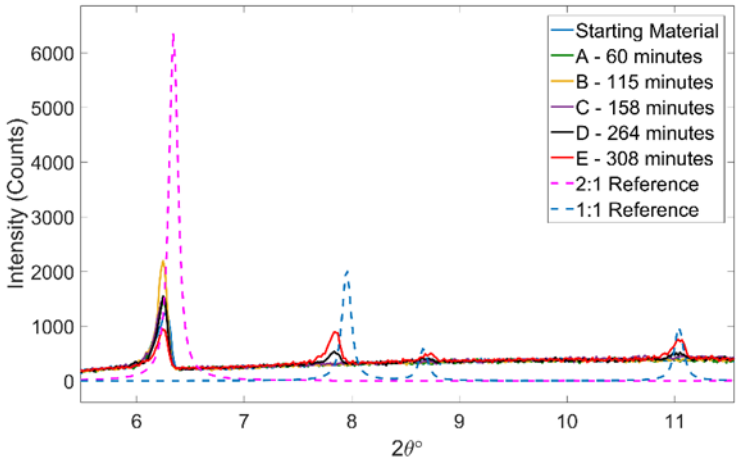

Figure 4.9. *XRPD from suspension stability study of 2:1 co-crystal in 48.8% ethanol – water (w/w).*

This makes solubility determination more difficult as the 2:1 solid form is not thermodynamically stable at the chosen process conditions. However, the solid-

liquid equilibrium of the metastable solid phase was determined for the purpose of thermodynamic yield calculations. The solubility test was timed to avoid any significant transformation. Solubility measurements were carried out in 48.8% (w/w) ethanol/water mixture, which is the same as the solvent mixture at the continuous mixer outlet during crystallization of 2:1 co-crystal. The results from six experiments suggest the solubility to be 0.0446 g/ml solvent with a high level of reproducibility based on clear points from image analysis. The spread of various measurements is illustrated in Figure 4.10.

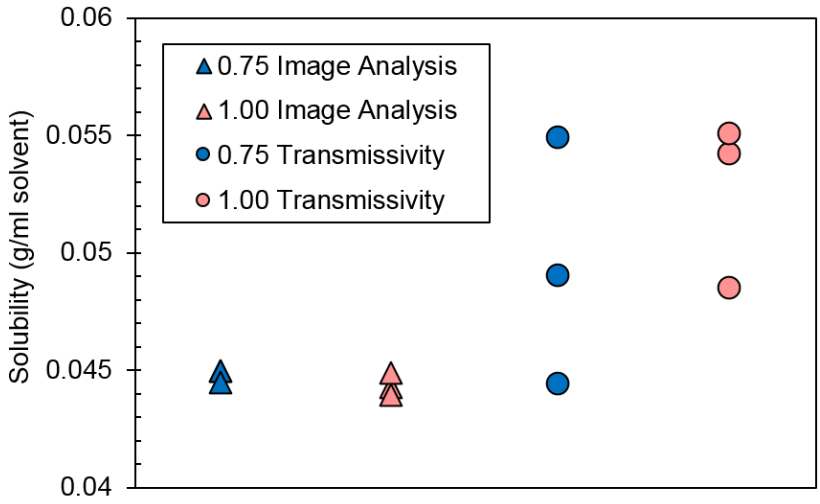

Figure 4.10. *Solubility of 2:1 co-crystal in 48.8% ethanol – water (w/w) at 25 °C. Results are shown based on clear point analysis from both images and transmissivity.*

The high spread of clear point measurements based on transmission may be attributed to the limited ability to detect solids by transmission measurements at low concentrations, especially for thin needles. The different solvent addition rates show comparable results, therefore, the result is not dependent on the kinetics of crystal dissolution. The findings about the 2:1 co-crystal metastability point out that the outlet composition of the crystallizer slurry is either in the 1:1

co-crystal or a mixture of the 1:1 and 2:1 co-crystal regions on the phase diagram. The solubility of the 2:1 co-crystal has been previously reported between 0.0367 g/ml and 0.0482 g/ml for 50% water/ethanol mixture by using two methods.[103] However, the measurements reported therein have a high variability and the gravimetry method implemented did not seem to account for a possibility of a phase transformation. Therefore, it is possible that in some cases the solubility of the 1:1 co-crystal or a mixture of both co-crystal phases could have been measured. A recent study by Munshi *et al*.[102] shows the ternary phase diagram at 50% ethanol/water, although it was not reported whether this was 50% by mass or by volume. As we have shown, solvent mediated transformation may occur in this system under conditions studied in this and previous works, and this may perhaps also help to explain the unusual shape of the phase diagram reported.

4.4.3. CONTINUOUS CRYSTALLIZATION

Moving from benchtop vial-based screening to a continuous platform introduces new process parameters and challenges. The overall flow rate was found to have a strong impact on the mixing regime and thus final particle properties. Three different overall flow rates were examined with the aim of producing the 2:1 co-crystal: 60 g/min, 40 g/min and 20 g/min at 50:50 ratio (w/w) of solution streams. The continuous runs revealed fouling and subsequent blockages to be a challenge, however blockage issues decreased with lower flowrates. Antifouling measures such as low power sonication used in Chapter 5 could be used to mitigate this issue.[104] The solid output was 0.507 g/min, 0.342 g/min and 0.0259 g/min for overall flowrates of 60 g/min, 40 g/min and 20 g/min, respectively. The L_{50} of particles obtained at overall flow rates of 60 g/min, 40 g/min and 20 g/min

was 361 μm, 317 μm and 238 μm, respectively. Despite producing the desired solid form (Figure 4.12) from all conditions, mixing performance drastically reduced at the overall flow rate of 20 g/min resulting in a lower solid yield. The low velocity difference between the capillary jet and the outer flow did not provide sufficient mixing to rapidly achieve the desired supersaturation. The same process at the overall flow rate of 20 g/min resulted in 0.0484 g/min solid output in the Ehrfeld platform. Clearly, mixing conditions influence nucleation kinetics of co-crystal as the solid yield and resulting particle size distribution (Figure 4.17) varies with overall flowrate although the overall solution composition is the same in all cases. In order to achieve a higher yield in the crystallization process, increasing of residence time downstream from the mixing point combined with additional cooling stages should be considered. Further process optimization would benefit from more detailed knowledge of the relevant phase diagram and additional experiments in an expanded design space.

A continuous crystallization was also carried out to produce the 1:1 co-crystal, using flow rates of 15 g/min of benzoic acid solution through the capillary and 100 g/min of isonicotinamide solution through the outer tube. For this experiment the solutions were less concentrated to avoid blocking due to potentially high solid loading of the resulting slurry. The induction time at these concentrations was relatively long compared to the 2:1 co-crystal experiments and particles were not immediately visible in the mixer outlet. The solid output after holding the slurry for 18 minutes was 0.0726 g/min.

4.4.4. SOLID CHARACTERIZATION

Solid state characterization techniques were selected in order to establish solid phase identity and purity. Crystal unit cell parameters were previously documented for both co-crystal phases which makes powder X-ray diffraction suitable for phase verification. The co-crystal phases also have unique melting points verifiable by DSC. NMR was also used to independently verify the stoichiometry of coformers in the crystalline sample. The morphological differences in crystals for the 2:1 and 1:1 forms were minor. The needle shaped morphology of both co-crystal forms can be seen in Figure 4.11. Results from Malvern Morphologi G3 are shown in Figure 4.17 and Figure 4.18. Similar aspect ratio distributions were found for both co-crystal forms. Analysis by XRPD on the dry samples from the capillary mixer is shown in Figure 4.12. Lines A, B and C are samples from continuous runs designed to produce the 2:1 co-crystal. Simulated patterns are generated from unit cell data available from the Cambridge Structural Database under structure labels: BUDWEC[42] and MOVTOH[41] for the 1:1 and 2:1 co-crystals respectively. Comparison with D – the simulated pattern suggests that a pure 2:1 co-crystal phase has been produced by all runs. Similarly, line E shows pure 1:1 co-crystal by comparison to the 1:1 co-crystal simulated pattern – line F. This is further supported by results from DSC and TGA shown in Figure 4.13. DSC for the 2:1 co-crystal samples shows a sharp thermal event previously reported at 142 – 143°C for the 2:1 co-crystal[105]. The TGA curves also show a decrease in mass from 148-150°C onwards indicating sample decomposition. Similarly, DSC for 1:1 sample shows a unique endotherm above 160 °C, at the expected melting point of the 1:1 co-crystal[105] with

subsequent decomposition. XRPD on samples from the Ehrfeld platform are in Figure 4.15.

For additional confirmation, the samples were analyzed using ATR-IR. The absorbance spectra are in Figure 4.14. The figures show a spectrum for each starting material as well as samples from continuous experiments. The co-crystal phases have well-defined unique spectra and it is possible to distinguish the 2:1 and 1:1 co-crystals using IR spectrometry.

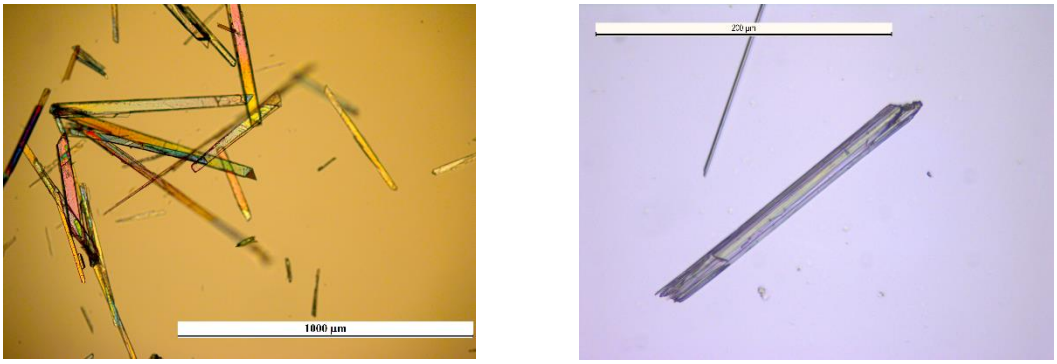

Figure 4.11. *Optical microscope images: 2:1 co-crystal (Left) and 1:1 co-crystal (Right).*

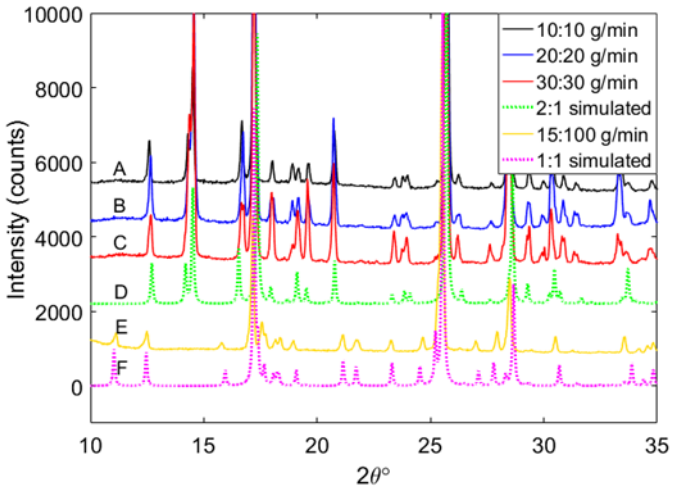

Figure 4.12. *XRPD for samples from all continuous runs from concentric capillary mixer together with calculated patterns.*

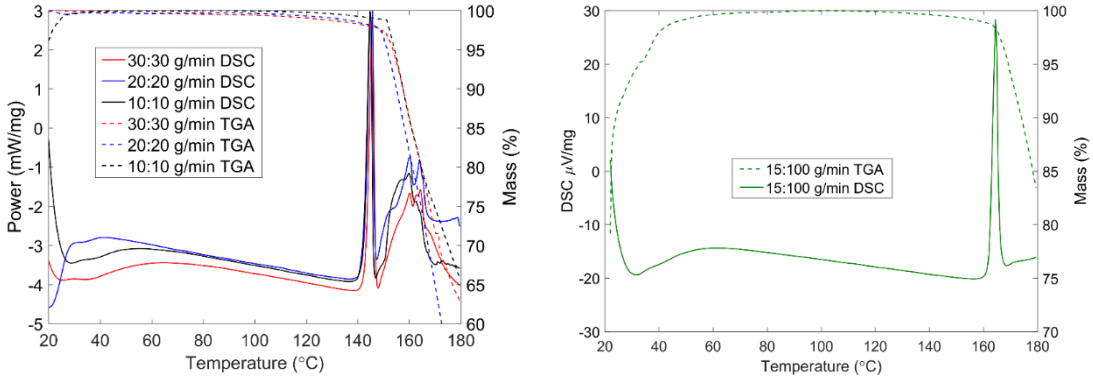

Figure 4.13. *DSC/TGA for samples for 2:1 (left) and 1:1 (right) co-crystal from continuous runs.*

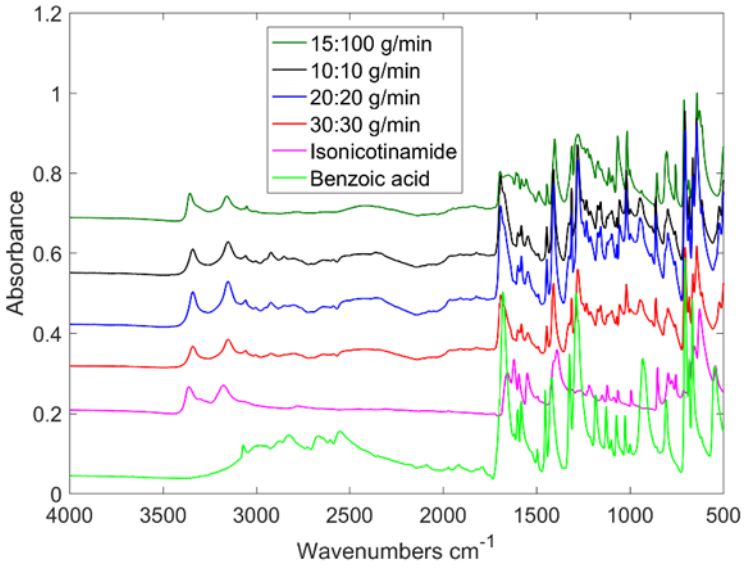

Figure 4.14. *ATR-IR spectra for starting material and samples from continuous runs.*

NMR analyses on solid samples dissolved in deuterated DMSO from each continuous run confirmed (within 2% error) a 2:1 ratio for each sample from the continuous runs aimed to produce 2:1 co-crystal. A sample of NMR results showing chemical shifts is shown in Figure 4.16. Continuous experiments using 40 g/min and 60 g/min flow rates produced particles of very similar particle size and shape characteristics as shown in Figure 4.17. In the same figure, results

from 20 g/min continuous experiment show significantly smaller particles at much lower solid yield. The aspect ratios for the particles from 20 g/min run are more needle-like with a narrower distribution.

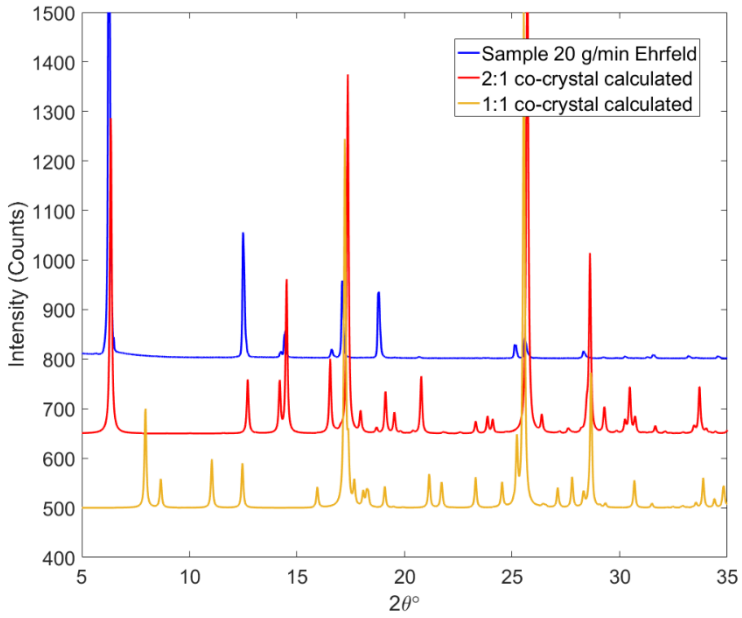

Figure 4.15. *XRPD from continuous run utilizing the Ehrfeld MMRS to produce 2:1 co-crystal.*

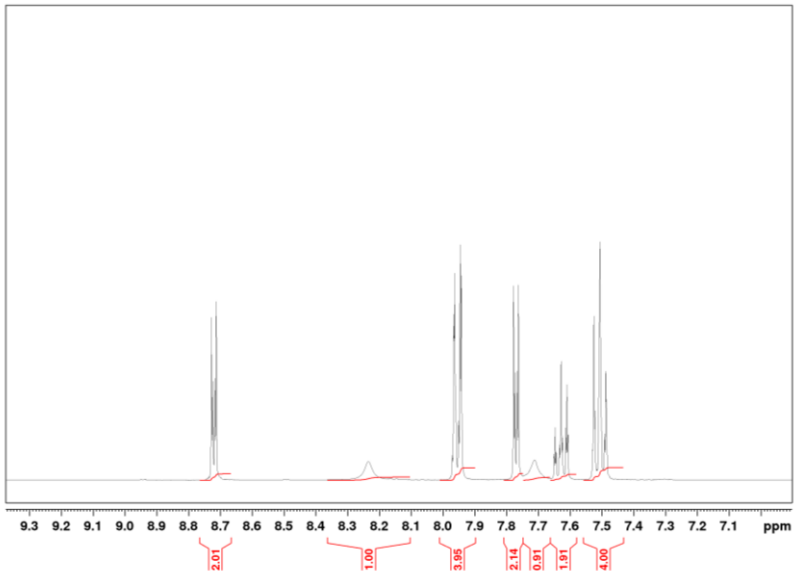

Figure 4.16. *Sample NMR chemical shifts of 2:1 co-crystal.*

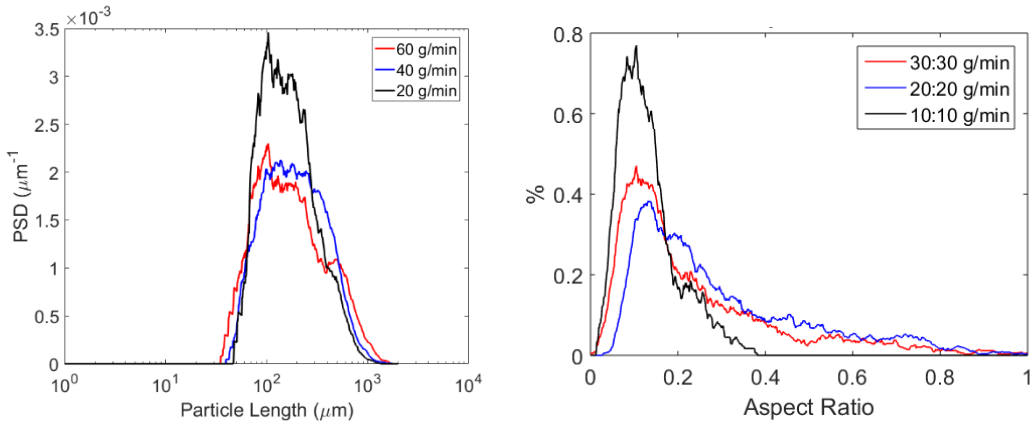

Figure 4.17. *Number weighted particle length distribution of 2:1 co-crystals measured using Malvern Morphologi (left) and number weighted aspect ratio distribution (right).*

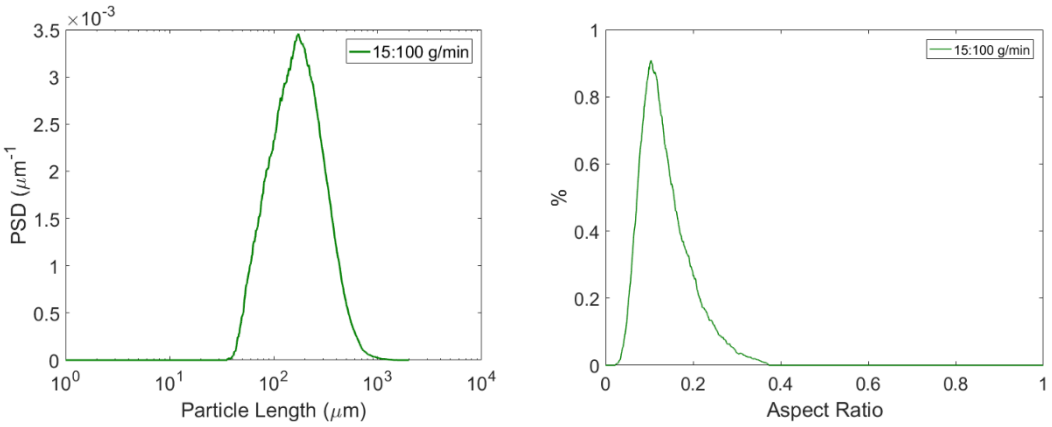

Figure 4.18. *Number weighted particle length distribution of 1:1 co-crystals measured using Malvern Morphologi (left) and number weighted aspect ratio distribution (right).*

The results from all utilized analytical methods show that both 2:1 and 1:1 pure forms of the co-crystal can be produced using the combined approach method based on mixing-induced supersaturation in a continuous crystallization process. The combined antisolvent and reactive crystallization approach allows for additional flexibility in reaching specific phase regions in multicomponent systems using multiple solvents.

4.5. CONCLUSIONS

Design of Experiments was used to find conditions suitable for formation of 2:1 and 1:1 co-crystals of benzoic acid and isonicotinamide by mixing ethanolic solutions of benzoic acid and aqueous solutions of isonicotinamide in isothermal conditions. The input parameters were the two solution concentrations and the mass ratio of the two solutions, while the output variables were the solid form produced, solid yield, induction time and slurry flow rating. Optimal conditions were then identified for both 2:1 and 1:1 co-crystal formation and continuous crystallization experiments were performed at several total flow rates. Both solid forms were selectively produced in continuous crystallization as confirmed by XPRD, IR, DSC and NMR. Mixing conditions were found to influence the solid yield and particle size distribution of crystal produced although not the solid form.

The combined antisolvent and reactive crystallization approach can be a useful tool for reaching solid phases that are otherwise difficult to access through mixing-induced supersaturation. Under conditions of thermodynamic control, it may be possible to reach certain regions of phase diagrams that would be not accessible by other approaches due to non-ideal shapes of some phase diagrams. Under conditions of kinetic control, it may be possible to influence nucleation kinetics through the initial mixing of two solutions which would depend on compositions of both solutions as well as mixing conditions applied.

CHAPTER 5

CONTINUOUS CRYSTALLIZATION OF SOLID SOLUTIONS

5.1. INTRODUCTION

Solid solutions are a unique type of a multicomponent crystal (MCC) that can exist in a range of stoichiometric ratios. This allows for engineering of a material with the optimum composition for the given application. Alloys, a type of solid solution, have been used to modify electrical and physical properties of metals by precisely varying the ratio of its constituents. Similarly, inorganic[106] and organic solid solutions have been engineered to provide the best performance in solar cells.[107] Potential applications of solid solutions are similar to those of co-crystals with the ability to fine tune stoichiometry for optimum performance, however, solid solutions of APIs are still an emerging area of research.[108] Solid solutions of organic molecules have been previously crystallized from solution using antisolvent crystallization[109] after synthesis of the target molecule and its impurity.

Amino acids are crucial for maintenance of health and are used extensively in foods, supplements and medicines and as such their solid-state properties and structures have been thoroughly investigated under a range of conditions.[110–116] Very few studies have investigated the amino acids in terms of the production of MCCs and fully characterized the solid forms the despite the importance of these materials. A search of the Cambridge Structural Database[117] has shown that typically structural studies have been limited to the crystallization of D- and L-enantiomers together; a view supported by a recent review of crystal structures of amino acids by Görbitz.[118] The relatively low number of observations of structurally characterized amino acid MMCs has largely been attributed to the inefficient packing that would result if single enantiomer systems were crystallized together.[119–125] However there have been a number of publications that have

shown solid solutions exist. For example, Kamei *et al*. investigated the solid-liquid equilibria in L-isoleucine with L-alanine[126] and L-norleucine[127] and discovered that solid solutions of the systems exist through the identification of changes to the c-axis length on substitution of norleucine into the system by monitoring the (1 0 0) reflection using synchrotron radiation. With respect to the systems discussed herein Koolman and Rousseau investigated the addition of small amounts of leucine and valine to isoleucine crystallizations and related the effects of these impurities on the morphology and size of the isoleucine to possible substitution mechanisms in the crystal structure.[128] It was also shown via XRPD and HPLC methods that solid solutions of L-valine, isoleucine, leucine can be formed although limited structural data were provided where the crystal structures of the solid solutions were assumed to be the same as those of the pure amino acids.[129] Very recently, a further study of L-isoleucine and L-valine solid solutions by Isakov *et al*. has detailed the phase behavior of this system in water and identified a new crystal structure associated with this complex.[130] Again, chromatographic and diffraction techniques were used to identify the species involved.

Similarly to the work in chapter 4, this work introduces the idea of a nucleator, a crystallizer to produce the desired solid form and be used on its own or seed a following growth dominated continuous crystallizer. This chapter describes the application of a novel continuous antisolvent crystallization approach to rapid production of tunable solid solutions of hydrophobic amino acids, comprising L-leucine, L-isoleucine and L-valine. The antisolvent approach provides an

alternative to other crystallization routes, e.g., ball-milling, liquid-assisted grinding and slurry methods, to achieve required multi-component solid phases.

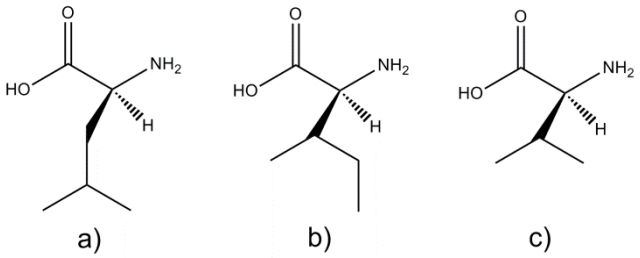

Figure 5.1. *Molecular form of (a) L-leucine (b) L-isoleucine (c) L-valine.*

This chapter is based on previously published work[43] consisting of the continuous crystallization aspect and the characterization of the solid solutions. The focus in this chapter is on the process development originally started by Ulrich Schacht while all crystallographic work has been carried out by the Oswald group at the University of Strathclyde.

5.2. EXPERIMENTAL

5.2.1. MATERIALS

The amino acids L-leucine, L-valine and L-isoleucine (≥98%) were supplied from Sigma Aldrich (Gillingham, UK). 2-propanol was supplied from Fisher Scientific. Deionized water was produced using the in-house Millipore Milli-Q system.

5.2.2. SOLUBILITY AND PHASE DIAGRAMS

Most amino acids show sharp decrease in solubility when increasing 2-propanol solvent fraction,[131] making it a good antisolvent. The ternary phase diagram for all pairs of amino acids (L-valine and L-leucine, L-valine and L-isoleucine, L-leucine and L-isoleucine) in water has also been previously published.[132,133]

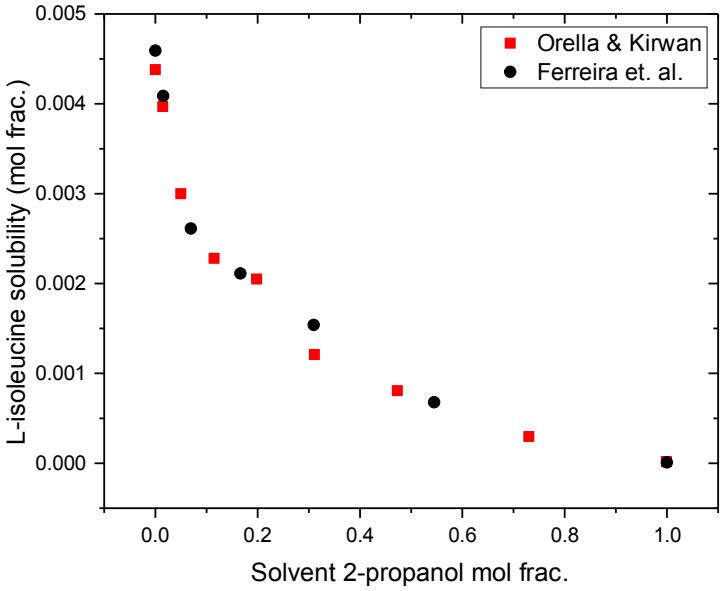

Figure 5.2. *L-isoleucine solubility in 2-propanol – water solvent mixture at 25 °C.*[134,135]

Figure 5.2 shows solubility of L-isoleucine at various solvent mixtures of water and 2-propanol at 25 °C from literature.[134,135] Similarly, Figure 5.3 shows the solubility of L-valine as a function of solvent composition at 25 °C.[136]

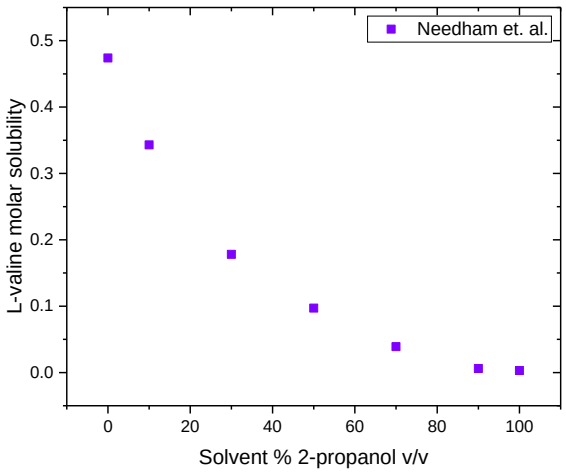

Figure 5.3. *L-valine solubility in 2-propanol – water mixtures at 25 °C*[136]

A ternary phase diagram of L-leucine and L-valine, one of the pairs of amino acids used here, determined by Kurosawa *et al*.[132] is shown in Figure 5.4.

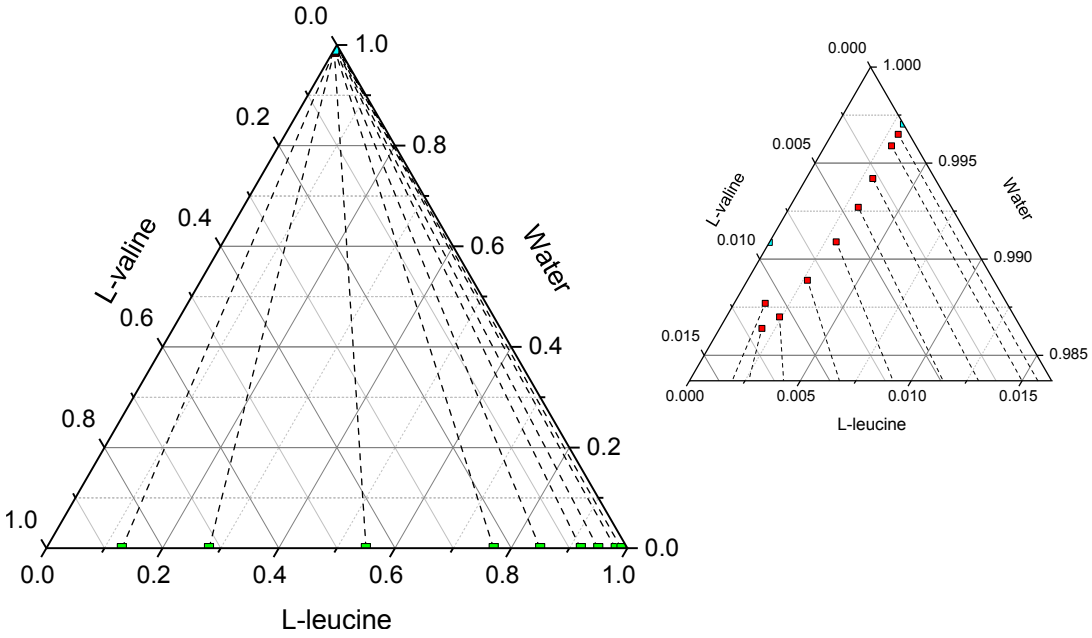

Figure 5.4. *L-leucine – L-valine ternary phase diagram plot in water at 25 °C. Data is from Kurosawa et al.*[132]

For clarity, each pair of the amino acid mixtures has been assigned a number shown in Table 5.1.

Table 5.1. *Amino acid pairs and label.*

Compound	Amino acid 1	Amino acid 2
1	L-leucine	L-isoleucine
2	L-leucine	L-valine
3	L-isoleucine	L-valine

5.2.3. BATCH ANTISOLVENT CRYSTALLIZATION

Solid solutions of each pair of amino acids were prepared using antisolvent crystallization on a 200 ml scale. An undersaturated aqueous solution was created by dissolving specific molar ratios of both amino acids in water. For each pair of amino acids at defined composition, chilled antisolvent was added to the aqueous solution under agitation by magnetic stirrer. The antisolvent was added all at once resulting in a 95% w/w 2-propanol solvent mixture. Resulting solid product was filtered and dried for analysis. The solid produced from these antisolvent crystallizations were used to determine the composition of the solid solutions and correlate it with the X-ray diffraction data. For each pair, starting compositions were chosen at the following ratios by mass: 90:10, 70:30, 50:50, 30:70 and 10:90. The resulting solid solution suspensions were filtered and dried. Dry powder was then analyzed by XRPD and HPLC.

5.2.4. CONTINUOUS ANTISOLVENT CRYSTALLIZATION

For the continuous process two different stoichiometric ratios were used to demonstrate the translation to a continuous antisolvent process. A diagram of the continuous antisolvent crystallization setup used here is shown in Figure 5.5.

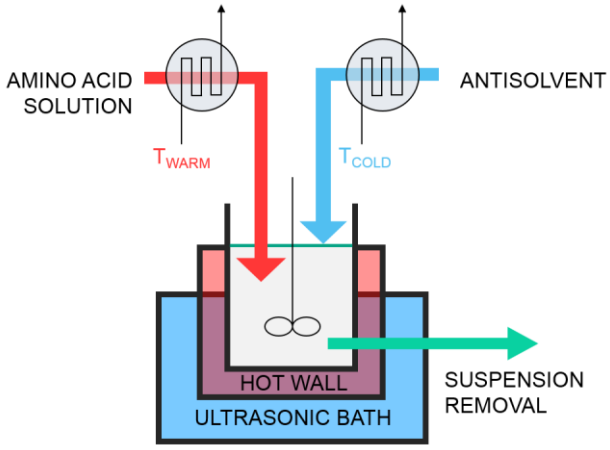

Figure 5.5. *MSMPR nucleator for antisolvent crystallization.*

In this process, a pre-heated aqueous solution of amino acids at the specific stoichiometric ratio at 45°C was continuously injected through a submerged stainless-steel nozzle (stream 1) into the stirred tank crystallizer vessel with operating volume of 50 mL. A flow rate (5 g/min) of stream 1 was delivered and controlled by an Ismatec external gear pumps (MCP-Z) with magnetically coupled pump head. The heat exchanger on stream 1 warmed the fluid to create an undersaturation of 0.4 - 0.5 with respect to the saturation concentration at crystallizer operating temperature. Nozzles with two different internal diameters (0.2 and 0.6 mm) in connection with stream 1 flow rates generated different jet injection velocities (1.1 – 8.0 m/s) into the solution. Cold antisolvent, 2-propanol, (stream 2) passed through a coil submerged in an ice bath with the flow rate of

95 g/min reaching temperatures between 3.4-4.5°C. After passing through the heat exchanger, stream 2 entered the stirred tank crystallizer through Marprene tubing falling from the top of the vessel onto the liquid surface. The flow rates of stream 2 were delivered by a Watson-Marlow 520S peristaltic pump to maintain a constant mixing ratio of the two inlet streams 1 and 2. The resulting temperature in the crystallizer was kept constant throughout the process (20 °C). This was achieved by balancing temperatures of colder inlet streams with an external jacket operating at a fixed higher temperature of 55 °C. Since the mean residence time in the crystallizer was very short, there was a significant temperature difference between the solution in the crystallizer and the vessel wall heated by the jacket. The reason for this was to minimize supersaturation at the vessel walls in order to decrease a propensity for fouling which would interfere with extended operation of the crystallizer in continuous mode. Due to the short residence time, the hot crystallizer wall did not severely hinder the overall product yield. Fouling was further prevented by immersing the crystallizer vessel in an ultrasonic bath (40 kHz, 50W), which was operated while the continuous crystallization was running. The mean residence time in the crystallizer was 30 seconds and the outlet stream was continuously withdrawn to a storage vessel where it was collected before subsequent filtration and drying. Aqueous solutions were fed at a fixed molar ratio of 50:50 or 40:60.

5.2.5. ANALYSIS

HPLC-MS

HPLC with mass spectrometric detection was used to analyze the composition of the complexes from the batch antisolvent crystallization where the initial feedstock compositions were altered. Stock solutions of each amino acid were prepared by dissolving suitable amounts in HPLC grade water (Waters Milli-Q). (Note, 2% v/v acetonitrile was added to each amino acid solution prior to making to volume to aid dissolution). Mixed working standards of the two required amino acids were prepared by diluting the stock solution with 80:20 acetonitrile:water such that the concentrations were in the range ~1-10 or 1-12 µg/ml. Two chromatographic systems were used for the analysis. Solid solutions of L-leucine – L-isoleucine and L-leucine – L-valine (Compounds 1 and 2) were analyzed using an isocratic HPLC system. This system consisted of an Agilent 1260 infinity HPLC (Agilent Technologies). The mobile phase was 20% 50 mM ammonium formate in water and 80% acetonitrile at a flow rate of 500 µL/min. A SeQuant ZIC-HILIC column (HiChrom) was used (150 x 4.6 mm, 5 µm particle size) at a temperature of 30 °C. The injection volume was 10 µL. Detection of the amino acids was achieved using an Agilent 6460 Triple Quad mass spectrometer (Agilent Technologies) equipped with an electrospray source. The electrospray needle was maintained at 2.5 kV. The gas temperature was 300 °C. Nebulizing gas and sheath gas flows were at 3 L/min and 4 L/min respectively. The mass spectrometer was operated under MRM mode with the fragmentor set at 135 V and the collision energy set at 20 V. The mass transitions (precursor → product) monitored were m/z 132 → 86 for L-leucine and L-isoleucine and 118 → 72 for

valine. The approximate retention times were 9.4 min (leucine), 10.0 min (isoleucine) and 12.5 min (valine). L-valine was well resolved (Rs > 4) from the other two components, and L-leucine and L-isoleucine also showed acceptable resolution (Rs = 1.56).

For compound 3 (containing L-isoleucine and L-valine), a gradient HPLC method was used for the analysis. This system consisted of a Thermo Finnigan Surveyor HPLC (ThermoFisher Scientific). The mobile phases for HPLC were: (A) 20 mM ammonium carbonate in water and (B) acetonitrile. Gradient runs were programmed using a linear gradient from 20% B to 50% B over 30 minutes at a flow of 300 µL/min. The equilibration time of the column between injections was 8 min. A SeQuant ZIC-pHILIC column (HiChrom) was used (150 x 4.6 mm, 5 µm particle size) at ambient temperature (approximately 20°C). The injection volume was 2 µL. Detection of the amino acids was achieved using a Finnegan LTQ Orbitrap Fourier-Transform mass spectrometer (ThermoFisher Scientific) equipped with an electrospray source. The electrospray needle was maintained at 4.5 kV and 275°C. Sheath and auxiliary gas flows were set at 50 and 15 arbitrary units respectively shown on the device. A full mass scan was performed in positive ion mode with a mass range of m/z 100 to 1200 and the resolution was 30000. Extracted ions at m/z 118.09 (valine) and m/z 132.1 isoleucine) were used for quantification purposes. The approximate retention times were 9.7 min (isoleucine) and 11.1 min (valine). L-valine and L-isoleucine were baseline resolved (Rs >2). Recoveries were confirmed using separately prepared standard solutions.

SINGLE CRYSTAL X-RAY DIFFRACTION ANALYSIS

A number of crystallizations have been performed to crystallize the novel complexes. Initially equimolar quantities of two amino acids (~0.05 g, 0.4 mmol) were placed in a vial together with water (5 ml) and heat was applied in order to complete dissolution. After a period of a week at 25°C colorless crystals, of sufficient quality for single crystal diffraction, appeared through evaporative crystallization. Many crystallizations with varying ratios of components, including saturated solutions of the components, were used. All these crystallizations appeared to yield crystals of the same stoichiometry except for compound 2 where one crystal (identified using the UK National Crystallography Service) showed a different composition to that observed in our home laboratory.

CRYSTAL STRUCTURE DETERMINATION

X-ray diffraction intensities for L-leucine: L-isoleucine (1), L-leucine: L-valine (2NCS), L-isoleucine: L-valine (3) were collected at I19 at Diamond Light Source (1)[137] and by the National Crystallography service (2NCS & 3).[138] X-ray diffraction intensities for compound 2 were collected with Mo-Kα radiation on a Bruker KAPPA Apex II CCD diffractometer equipped with an Oxford Cryosystems Cryostream-Plus variable-temperature device operating at -150 °C.[139] Absorption corrections were carried out using the multiscan procedure SADABS (Sheldrick, based on the procedure described by Blessing).[140,141] The structures were solved by direct methods (SIR-92)[142] and refined by full-matrix least-squares against F ($I > 3\sigma$) using all data (CRYSTALS).[143] Due to the wavelength of the source (0.71073 Å) the chirality of the amino acids was assumed to be as stated by the

manufacturer however the molecules were consistent with each other in the model i.e. both molecules were in the L-enantiomer.

The basic amino acid backbone (COO-C-N) and the first carbon of the chain was easily observed and used as the basic starting model for the refinements. From the difference map extra peaks were observed that were of the correct geometry to be assigned to be the components of a specific amino acid. Once the two molecules were identified further difference maps were used to find subsequent atoms that could only be assigned to a second component. These different components were assigned part numbers. The bond distances of the carbon side-chains (for compounds 1 and 2) were restrained to be similar to those found in the Cambridge Structural Database[117] (1.54 Å for bonds between secondary carbons and 1.51 Å for bonds to primary carbons). Thermal similarity and vibrational restraints were also applied. The parts were given values of 50% occupancy and allowed to refine. Compounds 1 and 2 gave occupancy values that differed slightly, and the values quoted here are average values with a standard deviation. Compound 3 was more straight forward with the occupancy remaining at 50% for one of the molecules in the asymmetric unit. In this case once the occupancy was established the parts were not competitively refined. All hydrogen atoms attached to carbon atoms were geometrically placed and those participating in hydrogen bonding *i.e*. hydroxyl hydrogens were found in the difference map. All non-H atoms were modeled with anisotropic displacement parameters.

PHASE ANALYSIS- X-RAY POWDER DIFFRACTION

Laboratory powder diffraction

A small quantity (1-50 mg) of each sample from the antisolvent process was analyzed using XRPD data collected on a Bruker AXS D2-Phaser equipped with primary monochromated radiation (Cu-Kα1 λ = 1.54056 Å; 30kV and 10mA), a LYNXEYE Scintillation counter and rotating sample mount. Samples were ground lightly before being mounted on a 6 position sample holder. Data were collected from each sample in the range 4 – 35 ° 2θ with a 0.01° 2θ step size and 1 sec. step-1 count time.

Synchrotron powder X-ray diffraction

Powder X-ray diffraction (PXRD) data were collected at -150°C for the powder produced from the initial equimolar (50:50) anti-solvent crystallization for all three pairs of amino acids as solid solutions using Beamline I11 (HRPD) at the Diamond Light Source, Didcot, UK (λ = 0.826136(2) Å).[144,145] Samples were densely packed into 0.7 mm diameter thin-walled glass capillaries.

PARTICLE SIZE ANALYSIS

A Malvern Mastersizer 2000 (Malvern Instruments) laser diffraction instrument was used to determine the particle size distribution of solid powder samples. Sample crystal slurries from the crystallizer outlet tube were dispersed in mother-liquor from the crystallization experiment. A refractive index of 1.65 was used for the measurement and data analysis.

5.3. RESULTS

5.3.1. IDENTIFICATION OF THE SOLID SOLUTION

Previous work by Kurosawa *et al*.[132,133] and Isakov *et al*.[130] have shown that the three amino acids, L-leucine, L-isoleucine and L-valine, formed solid solutions via the interpretation of the (0 0 1) reflection from the X-ray powder diffraction patterns and HPLC methods. One of the limitations of the Kurosawa was that they assumed that the crystal structure of the materials remained the same at each composition. This was rectified for the L-isoleucine – L-valine system where Isakov and co-workers identified a new crystal form; a C-centered cell related to the basic amino acid unit cells. At the same time, through small scale batch evaporative crystallizations, we have been able to isolate crystals of the solid solutions of L-leucine – L-isoleucine, L-leucine – L-valine and L-isoleucine – L-valine with unit cell lengths close to the original phases but with a different β-angle. The structures were initially elucidated using single crystal X-ray diffraction using data collected by the National Crystallography Service (NCS)[138] and Diamond Light Source Rapid Access Service (RAS) at beamline I19.[146] After a period of two months in solution the crystal quality improved through annealing processes such that in-house data could be used to help verify the quantities of each component and confirm the NCS and RAS data. The proportion of each constituent is not stoichiometric and therefore five datasets were collected for each sample in order to be sure of the proportion of each amino acid within the crystals in each batch. The percentage composition in L-leucine – L-isoleucine is 59% L-isoleucine; L-leucine – L-valine is 61% L-leucine; L-isoleucine – L-valine is 75% L-valine. The composition of the latter did not show any variation between

datasets and was fixed hence no error. Interestingly, for L-leucine – L-valine, the extent of this disorder altered slightly over time. Analysis of small less mature crystals using NCS showed that the percentage occupancy for leucine-valine was 73:27 L-leucine – L-valine cf. 61:39 from more mature crystals indicating the change in the composition of the solution. The reported structures can be found in the CSD under the following reference codes: LENFUI, LENGAP/01, LENGIX.

The unit cells of all three solid solutions are different to their parent compounds with a significant change in the β-angle of the cell for compounds 1 & 2 and there is an addition of C-centring in compound 3 so whilst the unit cell dimensions are similar the packing of the molecules has been altered by the addition of a second component in line with the observations of Isakov *et al*.[130] These observations are contrary to the assumptions made by Kurosawa *et al.*[132] that the crystal structure was the same as the pure phases; nevertheless we do observe the non-stoichiometric quantities of materials indicating the solid solutions have been formed. Solid solutions from L-leucine – L-valine and L-leucine – L-isoleucine crystallize in $P2_1$ whilst solid solutions from L-valine – L-isoleucine crystallize in C2 with all forms possessing two molecules in the asymmetric unit. The basic amino acid hydrogen bonded chains exist in all three complexes and have a consistent geometry compared with the hydrogen bonding observed in the pure amino acid structures i.e. the disorder that has arisen due to the co-crystallization process has not affected these stronger intermolecular interactions.[147–149] The overall structure of the materials remains as a bilayer where head groups interact via hydrogen bonding with those of neighboring chains and the hydrophobic tail

groups of the amino acids interact with those of a different chain. The crystallographic information can be found in the associated publication.

5.3.2. BATCH ANTISOLVENT CRYSTALLIZATION

Results from analysis of the solid solutions from batch crystallization experiments carried out using XPRD for phase verification are presented here. XRPD patterns produced by solid solutions from L-leucine and L-valine are shown in Figure 5.6, solid solutions from L-isoleucine and L-valine in Figure 5.7 and L-leucine and L-isoleucine in Figure 5.8.

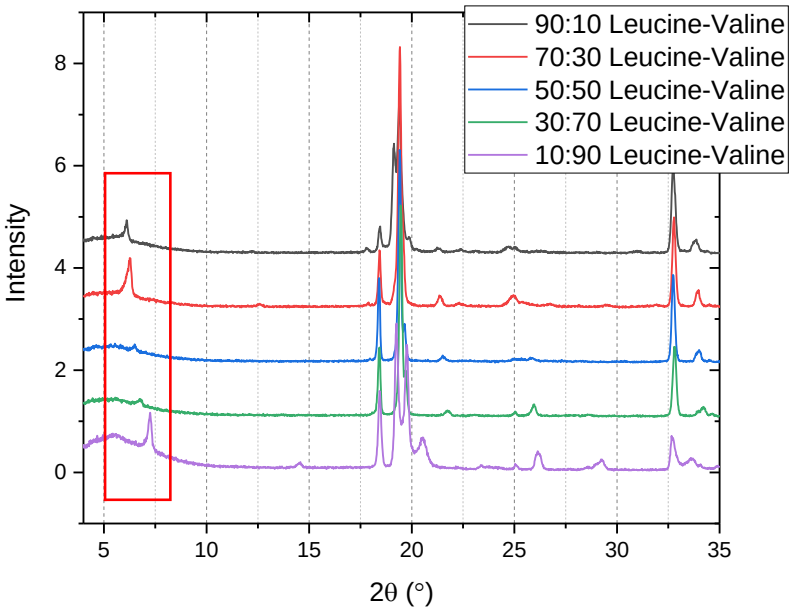

Figure 5.6. *XRPD of solids from batch crystallizations at various initial mass ratios of L-leucine and L-valine. For exact solid composition, see HPLC results. Red box highlights peak corresponding to the 001 plane.*

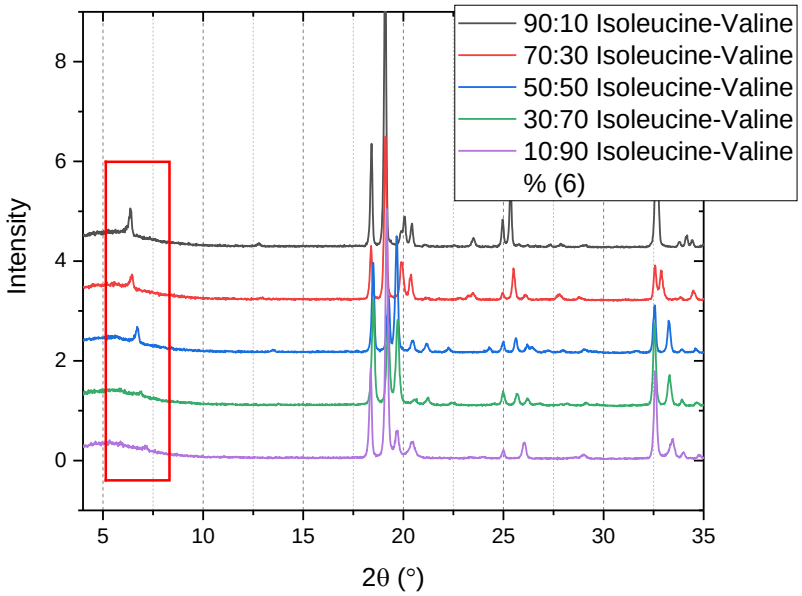

Figure 5.7. *XRPD of solids from batch crystallizations at various initial mass ratios of L-isoleucine and L-valine. For exact solid composition, see HPLC results. Red box highlights peak corresponding to the 200 plane.*

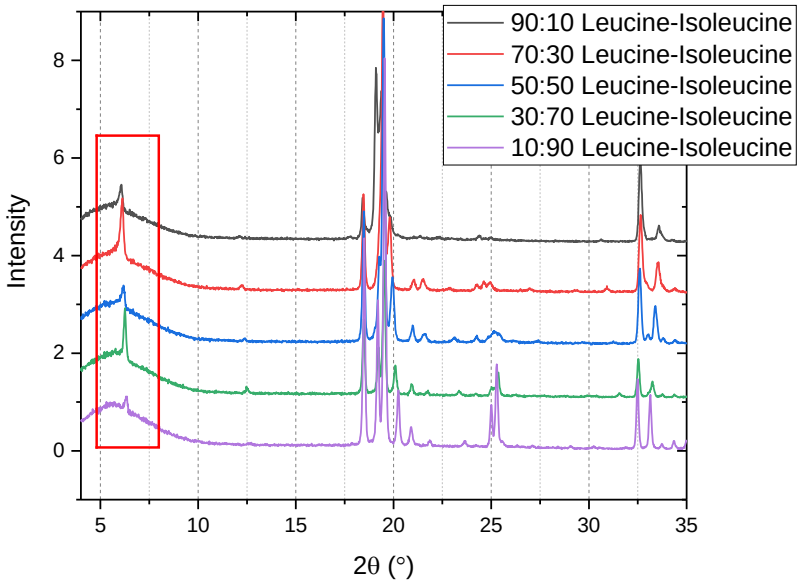

Figure 5.8. *XRPD of solids from batch crystallizations at various initial mass ratios of L-leucine and L-isoleucine. For exact solid composition, see HPLC results. Red box highlights peak corresponding to the 001 plane.*

Composition of each solid phase was determined by HPLC with calibration. The results giving the initial solute ratios and final solid solution compositions are presented in Table 5.2, Table 5.3 and Table 5.4 for L-leucine – L-isoleucine, L-leucine – L-valine and L-valine – L-isoleucine respectively.

Table 5.2. *HPLC composition analysis of Leucine-Isoleucine solid solutions.*

Leucine-Isoleucine starting ratio	Peak area leucine	Peak area isoleucine	Conc. leucine (µg/ml)	Conc. isoleucine (µg/ml)	Solid leucine content wt%
90:10	207065	71121	**4.74**	**0.41**	92.05
70:30	281044	290291	**6.60**	**3.01**	68.67
50:50	213543	431209	**4.91**	**4.69**	51.15
30:70	139692	597768	**3.05**	**6.66**	31.40
10:90	53574	699837	**0.89**	**7.88**	10.12

Table 5.3. *HPLC composition analysis of Leucine-Valine solid solutions.*

Leucine-Valine starting ratio	Peak area leucine	Peak area valine	Conc. leucine (µg/ml)	Conc. valine (µg/ml)	Solid leucine content wt%
90:10	335856	152825	**7.98**	**0.50**	94.14
70:30	318546	545529	**7.54**	**2.60**	74.34
50:50	204171	861695	**4.67**	**4.30**	52.06
30:70	148269	1239501	**3.27**	**6.33**	34.04
10:90	41621	1420527	**0.59**	**7.30**	7.43

From the determined solid solution compositions, the starting composition and the solid composition can be plotted on a ternary phase diagram with tie-lines passing through. Example ternary plots of solid solutions of L-leucine – L-valine and L-valine – L-isoleucine are in Figure 5.9 and Figure 5.10. However, as the batch crystallization experiments were not allowed to equilibrate for extended

period of time to determine equilibrium liquid composition, the liquid phase composition is not shown on the phase diagram.

Table 5.4. *HPLC composition analysis of Isoeucine-Valine solid solutions.*

Isoleucine-Valine starting ratio	Peak area isoleucine	Peak area valine	Conc. isoleucine (µg/ml)	Conc. valine (µg/ml)	Solid isoleucine content wt%
90:10	149925681	12338673	**11.88**	**1.69**	87.56
70:30	89688452	16564603	**7.08**	**2.25**	75.87
50:50	66964579	36877953	**5.27**	**4.97**	51.50
30:70	38643834	40597204	**3.02**	**5.46**	35.59
10:90	12873112	58770287	**0.97**	**7.89**	10.90

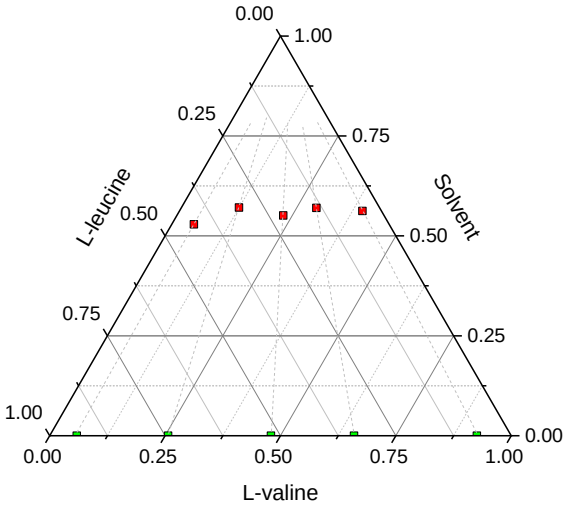

Figure 5.9. *Ternary phase diagram with tie-lines between starting composition (red squares) and solid phase composition (green squares) from batch experiments with L-leucine and L-valine.*

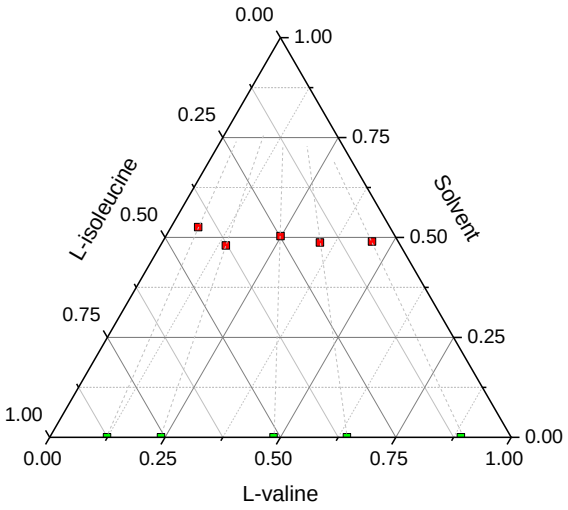

Figure 5.10. *Ternary phase diagram with tie-lines between starting composition (red squares) and solid phase composition (green squares) from batch experiments with L-isoleucine and L-valine.*

The interplanar spacing of each structure varies depending on its composition. d-spacing was calculated from XRPD measurement for each solid solution pair at all produced ratios. d-spacing of pure components was taken from literature. The calculated d-spacing (20 °C) and all solid solution compositions as identified by HPLC are shown in Table 5.5, Table 5.6 and Table 5.7 for L-leucine – L-isoleucine, L-leucine – L-valine and L-isoleucine – L-valine respectively. These data are also compared with those of Kurosawa.

Table 5.5. *d-spacing and structure of various compositions of Leucine-Isoleucine solid solutions.*

Wt% leucine content	**d-spacing observed Å**	**Structure**
0	13.94[41]	IL
10.12	13.98	SS
31.40	14.16	SS
51.15	14.29	SS
68.67	14.39	SS
92.05	14.55	SS
100	14.62[60]	L

Table 5.6. *d-spacing and structure of various compositions of Leucine-Valine solid solutions.*

Wt% leucine content	**d-spacing observed Å**	**Structure**
0	12.06[61]	V
7.43	12.15	V
34.04	13.03	SS
52.06	13.47	SS
74.34	14.04	SS
94.14	14.41	SS
100	14.62[60]	L

Table 5.7. *d-spacing and structure of various compositions of Valine-Isoleucine solid solutions.*

Wt% isoleucine content	d-spacing observed Å	Structure
0	12.06[61]	V
10.90	12.35	V
35.59	12.83	SS
51.50	13.08	SS
75.87	13.62	SS
75.87	14.08	IL
87.56	13.80	SS
87.56	14.03	IL
100	13.94[41]	IL

For L-leucine – L-isoleucine, we observe that the solid solution phase can be fit to all our data at various compositions. In comparison with data from Kurosawa *et al.*[132] our data shows more linear change with composition as seen in Figure 5.11.

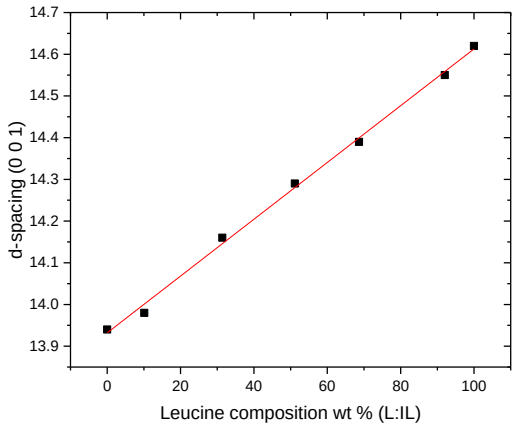

Figure 5.11*. d-spacing at various L-leucine – L-isoleucine solid compositions.*

Both studies observe only one peak which suggests that the phases that were produced were pure. This reflects the subtle differences in the molecular structure of the two components. Isoleucine and leucine are the same size of molecule with a difference in the connectivity of the tail group. Substitution of isoleucine into the leucine structure has caused a change in the unit cell parameters mainly in the β-angle, 104° cf. 94.06°.[150]

The diffraction and composition data for L-leucine – L-valine mixtures from our study fits well with previous work showing a linear change of the d-spacing with the composition of the solid however at 10 % leucine the structure reverts to the valine structure as identified by the unit cell parameters. Again, there is a shift in the β-angle to 109° from ~94° & 90° for leucine and valine unit cell parameters respectively.

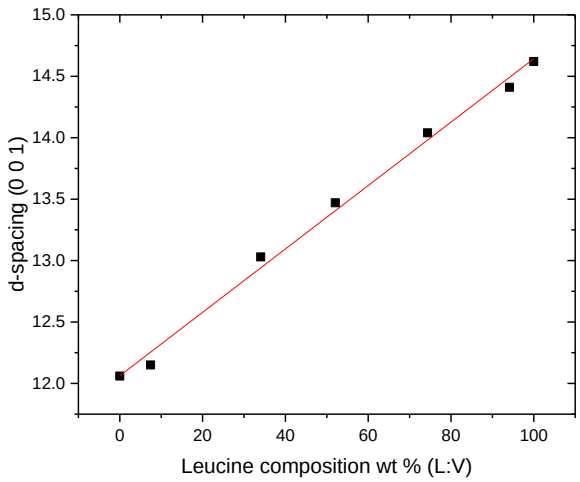

***Figure 5.12**. d-spacing at various L-leucine – L-valine solid compositions.*

L-isoleucine – L-valine starting mixtures show some indication that towards 100% composition of isoleucine there is a mixed phase with the solid solution and the

pure isoleucine solids; this is in line with the observations of Isakov *et al*.[130] The HPLC reveals in tables 5.3 to 5.5 that our composition is a close to the starting composition values i.e. 10, 30, 50 70, 90%. We also observe a biphasic nature down to 75% isoleucine with the second phase fitting the unit cell parameters of pure isoleucine Form I. Our data for Compound 3 follows that of Kurosawa[132] until there is a greater quantity of L-isoleucine (89 and 95 %) shown in Figure 5.13. At this point their data deviate from the projected linear cell expansion whilst our data remains in line with what one would suspect for a solid solution. In terms of the composition of the solid we have identified it is a 3:1 L-valine – L-isoleucine solid solution which is at the extremity of the V_2I phase that Isakov *et.al*.[130] highlighted in their study however interestingly the unit cell is larger in our case (both studies were collected at -173°C) which is counterintuitive given there is a greater portion of the smaller constituent. The packing is similar, bearing in mind the discrepancy of chirality from the structure in the CSD (ALIHUA), with no particular features that are different to guide any reasonable argument as to the differences. The previous determination has both molecules substituted with isoleucine contrary to our determination but despite this the a-axis (where the tails group interact) is longer.

One methodological note to make, that may impact our results compared with that of Isakov *et al.,*[130] is that the resulting solid from our experiment was harvested in a continuous manner and the from solution and was not ever subject to complete evaporation unlike the previous study hence the solubility of the initial components during the antisolvent crystallization will have an impact on the resulting solid collected. The solubility of the solid solution was shown by Isakov

to be higher than the isoleucine solubility hence the reason that we observe the mixed phase in the solid. This suggests that unlike the fully miscible case shown in Figure 1.2, there is a miscibility limit between the two components at the isoleucine rich side of the phase diagram.

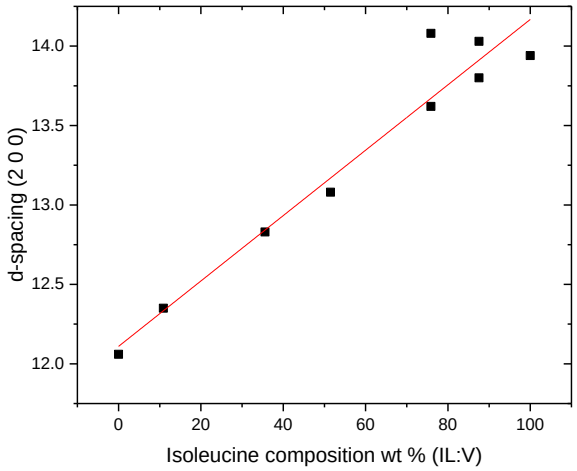

Figure 5.13. *d-spacing at various L-isoleucine – L-valine solid compositions.*

5.3.3. CONTINUOUS ANTISOLVENT CRYSTALLIZATION

After relatively short transition times (up to 20 minutes), steady state operation of the crystallizer was achieved, where a crystal slurry was present in the crystallizer and solid mass and crystallinity was not changing with time anymore during the subsequent steady state operation. Therefore, a consistent quality of the solid phase product was achieved under steady state conditions in the continuous operating mode. The percentage yield for each compound can be found in Figure 5.14. The figure also contains particle size evolution of solid solutions up to 100 minutes.

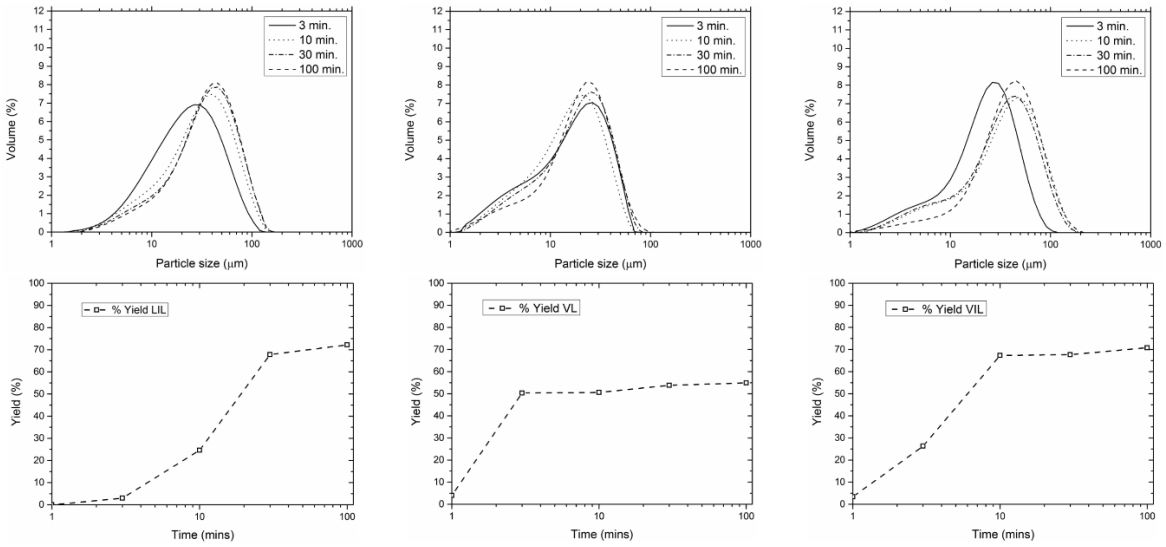

Figure 5.14. *Yield and PSD evolution in continuous runs.*

Due to the relatively high throughput of the 50 ml vessel (100 g/min), runs were not operated for longer than 2-3 hours. This demonstrates one of the advantages of continuous manufacturing, where lab scale equipment can have a significantly larger throughput than similarly sized batch counterpart. During this time, the process operated smoothly without any significant encrustation on the vessel walls as the antifouling measures implemented were effective. Without ultrasound and heated crystallizer walls, encrustation develops around the liquid surface. However, minor fouling occurred at the submerged inlet nozzle where amino acid solution enters the MSMPR nucleator. Due to the small nozzle diameter, fouling on the inlet can significantly increase the pressure drop and could eventually lead to blockage. There are many configuration options which would alleviate this issue and optimize the system for extended operation. For example, having the nozzle above the liquid layer or dividing antisolvent addition across multiple MSMPR stages.

As the relationship between d-spacing and solid solution composition has been established in batch crystallization, the composition of the solid solutions produced in the continuous crystallizer can be determined from XRPD data. For the continuous runs with amino acids in fed in 50:50 ratio, XRPD data collected on a synchrotron is shown in Figure 5.15. The XRD data was Pawley fitted with unit cell parameters from structures solved in batch crystallization section. From the d-spacing, the determined composition of each solid phase is very close to the feed ratio. This was the case in batch crystallizations as well at 50:50 amino acid ratio.

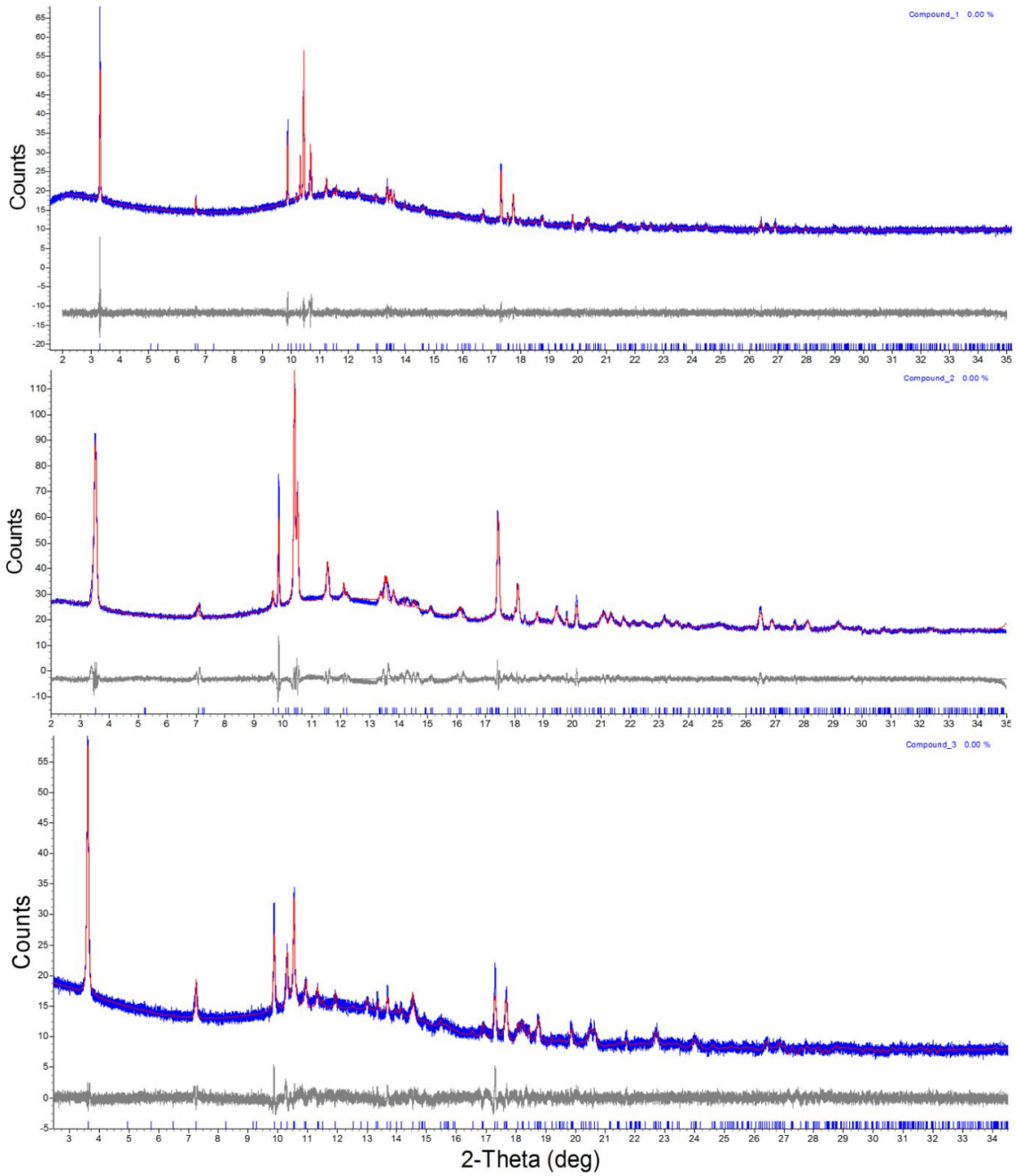

Figure 5.15. *Pawley fits of the diffraction data from I11 for compounds 1 (top), 2 (middle) and 3 (bottom) obtained from continuous process (50:50 molar ratio) using the unit cell parameters from our single crystal work.*

5.4. CONCLUSIONS

This chapter has shown that tunable solid solutions of hydrophobic amino acids can be formed easily using a novel rapid, scalable and reproducible approach through continuous antisolvent crystallization. It is rapid, since the mean residence time in the crystallizer is only 30 seconds. The process is scalable as continuous processes typically do not require a large operating volume for the same throughput as batch. Often laboratory sized equipment can be used for manufacturing scale, offering considerable advantages over traditional batch-based scale up approaches. Fouling issues in a single MSMPR have also been addressed without significantly compromising yield.

We have shown that we are able to control the formation of solid solutions easily using this method. In high value chemicals manufacture, reproducibility is a key attribute and can be achieved through continuous operation at steady state. The process reported in this chapter can be adapted to fully continuous operation with the crystal growth step being controlled in a continuous crystallization platform. The development, testing and implementation of continuous crystallization approaches are of particular importance in light of increased interest in continuous manufacturing processes by which pharmaceutical and other high value chemical products can be formed routinely using continuous antisolvent crystallization.

CHAPTER 6

FINAL CONCLUSIONS

This thesis has addressed the challenges of developing consistent, continuous crystallization processes of multicomponent crystals. Crystallization of multicomponent materials introduces several new challenges compared to single components, most notably the increase in complexity of phase diagrams. However, there are also new opportunities for mixing induced supersaturation combining antisolvent and reactive crystallization. The challenges addressed have been divided by chapters into predictive tools and semi-empirical phase diagram modeling, new phase diagram measurement methods for ternary multicomponent systems, development of a selective crystallization processes for co-crystals and solid solutions and their translation to continuous.

An activity coefficient model has been used to predict phase diagrams of related solid phases and of increasing number of components. The model works by building on existing data as *ab initio* models do not deliver the accuracy required, while determining all features of a phase diagram experimentally is time consuming. The model has been applied to paracetamol, lovastatin and 4-aminobenzoic acid. The methodology has been used to predict solubility of polymorphs and solubility in mixed solvent compositions. The application of this methodology has provided mixed results, indicating that activity coefficient models can reduce solvent screening time, however, measurement is still required for accuracy and reliability required for process development.

Two novel experimental methods for determining ternary multicomponent phase diagrams with focus on eutectic points have been demonstrated on the co-crystal system of benzoic acid and isonicotinamide in ethanol. One method uses more traditional equilibration and analysis approach, while the other uses Process

Analytical Technology and shift in composition to detect phase boundaries. However, both methods reduce the number of points required by focusing on the eutectic points of the phase diagrams and use thermodynamic theory to estimate the solid-liquid line. Both methods have the potential to be applied to other multicomponent systems with some modifications.

The same model co-crystal system has been used to develop a continuous crystallization process and demonstrate the reproducibility and selectivity of a process relying on mixing induced supersaturation. Process has been developed using a DoE in batch and translation to continuous in two different mixer geometries. The process has been used to produce both pure 2:1 and 1:1 by adjusting the feed composition. The combined mixing approach of reactive and antisolvent crystallization can be used to reach regions of the phase diagram not possible with each method on their own. The method can be also useful in crystallization of metastable forms due to the short residence time in mixing platforms.

In Chapter 5, an antisolvent crystallization of solid solutions of amino acids was implemented. And the crystal structure properties (determined by collaborators[43]) were related to the solid phase composition. The antisolvent crystallization process was also translated to continuous within a short residence time MSMPR. Challenges with encrustation were mitigated by using antifouling measures such as using an ultrasonic bath and heated crystallizer wall.

The translation from a batch to a continuous process has been successfully implemented for both co-crystals and solid solutions in static mixers. The

processes translate well to continuous mixers in terms of solid phase produced, however, the processes could be further optimized for yield, particle properties and for extended operation. Future work could also implement real time inline solutions for process monitoring for concentration, particle properties and solid form.

To accelerate process development of a crystallization of multicomponent materials, further work and implementation of phase diagram modeling and measurements is required. Screening for a suitable solvent matrix to carry out the process using traditional approaches of measuring entire phase diagrams is too time consuming. Automation and focus on key parts of a phase diagram, particularly the eutectic points, can reduce this time.

Activity coefficient models are constantly being developed with new models or modifications improving accuracy over the model tested in Chapter 2. Thermodynamic modeling is also a promising area for application of data driven models as there is a large pool of equilibrium data available while mechanistic models struggle to predict phase equilibrium consistently.

More research is expected both in the field of continuous crystallization as well as multicomponent forms of APIs as co-crystals and solid solutions become more common in the industry. As more products with co-crystals or solid solutions are investigated and approved, research into process development and screening methods is bound to follow.

REFERENCES

1. Davey, R. & Garside, J. *From Molecules to Crystallizers*. (Oxford University Press, 2000).
2. Coquerel, G. Crystallization of molecular systems from solution: phase diagrams, supersaturation and other basic concepts. *Chem. Soc. Rev.* **43**, 2286 (2014).
3. Braun, D. E. *et al.* Unraveling Complexity in the Solid Form Screening of a Pharmaceutical Salt: Why so Many Forms? Why so Few? *Cryst. Growth Des.* **17**, 5349–5365 (2017).
4. Bauer, J. F. Polymorphism—A Critical Consideration in Pharmaceutical Development, Manufacturing, and Stability. 9
5. Nývlt, J. The Ostwald Rule of Stages. *Cryst. Res. Technol.* **30**, 443–449 (1995).
6. Alvarez, A. J., Singh, A. & Myerson, A. S. Crystallization of Cyclosporine in a Multistage Continuous MSMPR Crystallizer. *Cryst. Growth Des.* **11**, 4392–4400 (2011).
7. McGlone, T. *et al.* Oscillatory Flow Reactors (OFRs) for Continuous Manufacturing and Crystallization. *Org. Process Res. Dev.* **19**, 1186–1202 (2015).
8. Ferguson, S., Morris, G., Hao, H., Barrett, M. & Glennon, B. In-situ monitoring and characterization of plug flow crystallizers. *18th Int. Symp. Ind. Cryst.* **77**, 105–111 (2012).
9. Vishweshwar, P., McMahon, J. A., Bis, J. A. & Zaworotko, M. J. Pharmaceutical Co-Crystals. *J. Pharm. Sci.* **95**, 499–516 (2006).

10. Cao, F., Amidon, G. L., Rodríguez-Hornedo, N. & Amidon, G. E. Mechanistic Basis of Cocrystal Dissolution Advantage. *J. Pharm. Sci.* **107**, 380–389 (2018).
11. Millar, D. I. A. *et al.* Crystal engineering of energetic materials: Co-crystals of CL-20. *CrystEngComm* **14**, 3742 (2012).
12. Landenberger, K. B. & Matzger, A. J. Cocrystal Engineering of a Prototype Energetic Material: Supramolecular Chemistry of 2,4,6-Trinitrotoluene. *Cryst. Growth Des.* **10**, 5341–5347 (2010).
13. Zhen, Y. *et al.* Organic Solid Solution Composed of Two Structurally Similar Porphyrins for Organic Solar Cells. *J. Am. Chem. Soc.* **137**, 2247–2252 (2015).
14. Domingos, S. *et al.* New forms of old drugs: improving without changing: New forms of old drugs. *J. Pharm. Pharmacol.* **67**, 830–846 (2015).
15. Aitipamula, S. *et al.* Polymorphs, Salts, and Cocrystals: What's in a Name? *Cryst. Growth Des.* **12**, 2147–2152 (2012).
16. Reus, M. A., van der Heijden, A. E. D. M. & ter Horst, J. H. Solubility Determination from Clear Points upon Solvent Addition. *Org. Process Res. Dev.* **19**, 1004–1011 (2015).
17. Lohmann, J., Joh, R. & Gmehling, J. From UNIFAC to Modified UNIFAC (Dortmund) †. *Ind. Eng. Chem. Res.* **40**, 957–964 (2001).
18. Anderson, T. F. & Prausnitz, J. M. Application of the UNIQUAC equation to calculation of multicomponent phase equilibria. 1. Vapor-liquid equilibria. *Ind. Eng. Chem. Process Des. Dev.* **17**, 552–561 (1978).

19. Chen, C.-C. & Crafts, P. A. Correlation and prediction of drug molecule solubility with the NRTL-SAC model. in *Computer Aided Chemical Engineering* (eds. Marquardt, W. & Pantelides, C.) **21**, 859–864 (Elsevier, 2006).
20. Klamt, A. Conductor-like Screening Model for Real Solvents: A New Approach to the Quantitative Calculation of Solvation Phenomena. *J. Phys. Chem.* **99**, 2224–2235 (1995).
21. Chapman, W. G., Gubbins, K. E., Jackson, G. & Radosz, M. SAFT: Equation-of-state solution model for associating fluids. *Fluid Phase Equilibria* **52**, 31–38 (1989).
22. Mascia, S. *et al.* End-to-End Continuous Manufacturing of Pharmaceuticals: Integrated Synthesis, Purification, and Final Dosage Formation. *Angew. Chem.* **125**, 12585–12589 (2013).
23. Kleinnebudde, P., Khinast, J. & Rantanen, J. *Continuous manufacturing of pharmaceuticals*. (2017).
24. May, S. A. Flow chemistry, continuous processing, and continuous manufacturing: A pharmaceutical perspective. *J. Flow Chem.* **7**, 137–145 (2017).
25. Baxendale, I. R. *et al.* Achieving Continuous Manufacturing: Technologies and Approaches for Synthesis, Workup, and Isolation of Drug Substance May 20–21, 2014 Continuous Manufacturing Symposium. *J. Pharm. Sci.* **104**, 781–791 (2015).

26. Burcham, C. L., Florence, A. J. & Johnson, M. D. Continuous Manufacturing in Pharmaceutical Process Development and Manufacturing. *Annu. Rev. Chem. Biomol. Eng.* **9**, 253–281 (2018).
27. Srai, J. S., Badman, C., Krumme, M., Futran, M. & Johnston, C. Future Supply Chains Enabled by Continuous Processing-Opportunities and Challenges. May 20-21, 2014 Continuous Manufacturing Symposium. *J. Pharm. Sci.* **104**, 840–849 (2015).
28. Su, Q., Nagy, Z. K. & Rielly, C. D. Pharmaceutical crystallisation processes from batch to continuous operation using MSMPR stages: Modelling, design, and control. *Chem. Eng. Process. Process Intensif.* **89**, 41–53 (2015).
29. Powell, K. A., Saleemi, A. N., Rielly, C. D. & Nagy, Z. K. Monitoring Continuous Crystallization of Paracetamol in the Presence of an Additive Using an Integrated PAT Array and Multivariate Methods. *Org. Process Res. Dev.* **20**, 626–636 (2016).
30. Agimelen, O. S. *et al.* Multi-sensor inline measurements of crystal size and shape distributions during high shear wet milling of crystal slurries. *Adv. Powder Technol.* (2018). doi:10.1016/j.apt.2018.09.003
31. Myerson, A. S., Krumme, M., Nasr, M., Thomas, H. & Braatz, R. D. Control Systems Engineering in Continuous Pharmaceutical Manufacturing. May 20–21, 2014 Continuous Manufacturing Symposium. *J. Pharm. Sci.* **104**, 832–839 (2014).
32. Lakerveld, R., Benyahia, B., Braatz, R. D. & Barton, P. I. Model-based design of a plant-wide control strategy for a continuous pharmaceutical plant. *AIChE J.* **59**, 3671–3685 (2013).

33. Nagy, Z. K., Fevotte, G., Kramer, H. & Simon, L. L. Recent advances in the monitoring, modelling and control of crystallization systems. *Chem. Eng. Res. Des.* **91**, 1903–1922 (2013).
34. Majumder, A. & Nagy, Z. K. Dynamic Modeling of Encrust Formation and Mitigation Strategy in a Continuous Plug Flow Crystallizer. *Cryst. Growth Des.* **15**, 1129–1140 (2015).
35. Koswara, A. & Nagy, Z. K. Anti-Fouling Control of Plug-Flow Crystallization via Heating and Cooling Cycle. *9th IFAC Symp. Adv. Control Chem. Process. ADCHEM 2015* **48**, 193–198 (2015).
36. Sim, G. A., Robertson, J. M. & Goodwin, T. H. The crystal and molecular structure of benzoic acid. *Acta Crystallogr.* **8**, 157–164 (1955).
37. Li, J., Bourne, S. A. & Caira, M. R. New polymorphs of isonicotinamide and nicotinamide. *Chem Commun* **47**, 1530–1532 (2011).
38. Aakeröy, C. B., Beatty, A. M., Helfrich, B. A. & Nieuwenhuyzen, M. Do Polymorphic Compounds Make Good Cocrystallizing Agents? A Structural Case Study that Demonstrates the Importance of Synthon Flexibility. *Cryst. Growth Des.* **3**, 159–165 (2003).
39. Eccles, K. S. *et al.* Expanding the crystal landscape of isonicotinamide: concomitant polymorphism and co-crystallisation. *CrystEngComm* **13**, 6923–6925 (2011).
40. Vicatos, A. I. & Caira, M. R. A new polymorph of the common coformer isonicotinamide. *CrystEngComm* **21**, 843–849 (2019).

41. Seaton, C. C., Parkin, A., Wilson, C. C. & Blagden, N. Controlling the formation of benzoic acid: isonicotinamide molecular complexes. *Cryst. Growth Des.* **9**, 47–56 (2008).
42. Aakeröy, C. B., Beatty, A. M. & Helfrich, B. A. “Total Synthesis” Supramolecular Style: Design and Hydrogen-Bond-Directed Assembly of Ternary Supermolecules. *Angew. Chem. Int. Ed.* **40**, 3240–3242 (2001).
43. Raza, S. A. *et al.* Rapid Continuous Antisolvent Crystallization of Multicomponent Systems. *Cryst. Growth Des.* **18**, 210–218 (2018).
44. Torres-Marchal, C., Cantalino, A. L. & de Brito, R. M. Prediction of vapor-liquid equilibria (VLE) from dilute systems data using the SRK equation of state: Industrial applications. *Fluid Phase Equilibria* **52**, 111–117 (1989).
45. Loschen, C. & Klamt, A. Solubility prediction, solvate and cocrystal screening as tools for rational crystal engineering. *J. Pharm. Pharmacol.* **67**, 803–811 (2015).
46. Caminos, A. A., Gani, R. & Brignole, E. A. A liquid-liquid extractor model based on UNIFAC. *Comput. Chem. Eng.* **8**, 127–136 (1984).
47. Gracin, S., Brinck, T. & Rasmuson, Å. C. Prediction of Solubility of Solid Organic Compounds in Solvents by UNIFAC. *Ind. Eng. Chem. Res.* **41**, 5114–5124 (2002).
48. Renon, H. & Prausnitz, J. M. Local compositions in thermodynamic excess functions for liquid mixtures. *AIChE J.* **14**, 135–144 (1968).
49. Klamt, A., Eckert, F., Hornig, M., Beck, M. E. & Bürger, T. Prediction of aqueous solubility of drugs and pesticides with COSMO-RS. *J. Comput. Chem.* **23**, 275–281 (2001).

50. Tung, H.-H., Tabora, J., Variankaval, N., Bakken, D. & Chen, C.-C. Prediction of Pharmaceutical Solubility Via NRTL-SAC and COSMO-SAC. *J. Pharm. Sci.* **97**, 1813–1820 (2008).
51. Bouillot, B., Spyriouni, T., Teychené, S. & Biscans, B. Solubility of pharmaceuticals: A comparison between SciPharma, a PC-SAFT-based approach, and NRTL-SAC. *Eur. Phys. J. Spec. Top.* **226**, 913–929 (2017).
52. Debye, P. & Hückel, E. The theory of electrolytes. I. Lowering of freezing point and related phenomena. *Phys. Z.* **9**, 185–206 (1923).
53. Cameretti, L. F., Sadowski, G. & Mollerup, J. M. Modeling of Aqueous Electrolyte Solutions with Perturbed-Chain Statistical Associated Fluid Theory. *Ind. Eng. Chem. Res.* **44**, 3355–3362 (2005).
54. Lange, L., Lehmkemper, K. & Sadowski, G. Predicting the Aqueous Solubility of Pharmaceutical Cocrystals As a Function of pH and Temperature. *Cryst. Growth Des.* **16**, 2726–2740 (2016).
55. Prausnitz, J. M., Lichtenthaler, R. N. & de Azevedo, E. G. *Molecular thermodynamics of fluid-phase equilibria*. (Prentice-Hall, 1986).
56. Lue, L. *Chemical Thermodynamics*. (Ventus Publishing, 2009).
57. Lorenz, H. Solubility and Solution Equilibria in Crystallization. in *Crystallization* 35–74 (John Wiley & Sons, Ltd, 2013). doi:10.1002/9783527650323.ch3
58. Pappa, G. D., Voutsas, E. C., Magoulas, K. & Tassios, D. P. Estimation of the Differential Molar Heat Capacities of Organic Compounds at Their Melting Point. *Ind. Eng. Chem. Res.* **44**, 3799–3806 (2005).

59. Gmehling, J., Rasmussen, P. & Fredenslund, A. Vapor-liquid equilibriums by UNIFAC group contribution. Revision and extension. 2. *Ind. Eng. Chem. Process Des. Dev.* **21**, 118–127 (1982).
60. Al-fnaish, H. & Lue, L. Modelling the solubility of H2S and CO2 in ionic liquids using PC-SAFT equation of state. *Fluid Phase Equilibria* **450**, 30–41 (2017).
61. Magnussen, T., Rasmussen, P. & Fredenslund, A. UNIFAC parameter table for prediction of liquid-liquid equilibriums. *Ind. Eng. Chem. Process Des. Dev.* **20**, 331–339 (1981).
62. Agnew, L. R., Cruickshank, D. L., McGlone, T. & Wilson, C. C. Controlled production of the elusive metastable form II of acetaminophen (paracetamol): a fully scalable templating approach in a cooling environment. *Chem Commun* **52**, 7368–7371 (2016).
63. Granberg, R. A. & Rasmuson, Å. C. Solubility of Paracetamol in Pure Solvents. *J. Chem. Eng. Data* **44**, 1391–1395 (1999).
64. Rengarajan, G. T., Enke, D., Steinhart, M. & Beiner, M. Size-dependent growth of polymorphs in nanopores and Ostwald's step rule of stages. *Phys. Chem. Chem. Phys.* **13**, 21367 (2011).
65. Gracin, S. & Rasmuson, Å. C. Polymorphism and Crystallization of *p* -Aminobenzoic Acid. *Cryst. Growth Des.* **4**, 1013–1023 (2004).
66. Svärd, M., Nordström, F. L., Hoffmann, E.-M., Aziz, B. & Rasmuson, Å. C. Thermodynamics and nucleation of the enantiotropic compound p-aminobenzoic acid. *CrystEngComm* **15**, 5020 (2013).

67. Mirmehrabi, M., Rohani, S. & Perry, L. Thermodynamic modeling of activity coefficient and prediction of solubility: Part 2. Semipredictive or semiempirical models. *J. Pharm. Sci.* **95**, 798–809 (2006).

68. Granberg, R. A. & Rasmuson, Å. C. Solubility of Paracetamol in Binary and Ternary Mixtures of Water + Acetone + Toluene. *J. Chem. Eng. Data* **45**, 478–483 (2000).

69. Hojjati, H. & Rohani, S. Measurement and Prediction of Solubility of Paracetamol in Water−Isopropanol Solution. Part 2. Prediction. *Org. Process Res. Dev.* **10**, 1110–1118 (2006).

70. Nti-Gyabaah, J., Chmielowski, R., Chan, V. & Chiew, Y. C. Solubility of lovastatin in a family of six alcohols: Ethanol, 1-propanol, 1-butanol, 1-pentanol, 1-hexanol, and 1-octanol. *Int. J. Pharm.* **359**, 111–117 (2008).

71. Nti-Gyabaah, J. & Chiew, Y. C. Solubility of Lovastatin in Ethyl Acetate, Propyl Acetate, Isopropyl Acetate, Butyl Acetate, *sec* -Butyl Acetate, Isobutyl Acetate, *tert* -Butyl Acetate, and 2-Butanone, between (285 and 313) K. *J. Chem. Eng. Data* **53**, 2060–2065 (2008).

72. Sun, H., Gong, J. & Wang, J. Solubility of Lovastatin in Acetone, Methanol, Ethanol, Ethyl Acetate, and Butyl Acetate between 283 K and 323 K. *J. Chem. Eng. Data* **50**, 1389–1391 (2005).

73. Gironi, F. & Lamberti, L. Vapour-liquid equilibrium data for the water-2-propanol system in the presence of dissolved salts. *Fluid Phase Equilibria* **105**, 273–286 (1995).

74. Burman, Å. U. & Ström, K. H. U. CALCULATION OF VAPOR LIQUID EQUILIBRIUM AND EXCESS ENTHALPY WITH THE UNIQUAC EQUATION. *Chem. Eng. Commun.* **194**, 1029–1052 (2007).
75. Voutsas, E. C., Pamouktsis, C., Argyris, D. & Pappa, G. D. Measurements and thermodynamic modeling of the ethanol–water system with emphasis to the azeotropic region. *Fluid Phase Equilibria* **308**, 135–141 (2011).
76. Hojjati, H. & Rohani, S. Measurement and Prediction of Solubility of Paracetamol in Water−Isopropanol Solution. Part 1. Measurement and Data Analysis. *Org. Process Res. Dev.* **10**, 1101–1109 (2006).
77. Garg, R. K. & Sarkar, D. Polymorphism control of p-aminobenzoic acid by isothermal anti-solvent crystallization. *J. Cryst. Growth* **454**, 180–185 (2016).
78. Chiarella, R. A., Davey, R. J. & Peterson, M. L. Making Co-CrystalsThe Utility of Ternary Phase Diagrams. *Cryst. Growth Des.* **7**, 1223–1226 (2007).
79. Springuel, G., Collard, L. & Leyssens, T. Ternary and quaternary phase diagrams: key tools for chiral resolution through solution cocrystallization. *CrystEngComm* **15**, 7951 (2013).
80. Ainouz, A., Authelin, J.-R., Billot, P. & Lieberman, H. Modeling and prediction of cocrystal phase diagrams. *Int. J. Pharm.* **374**, 82–89 (2009).
81. Holaň, J., Štěpánek, F., Billot, P. & Ridvan, L. The construction, prediction and measurement of co-crystal ternary phase diagrams as a tool for solvent selection. *Eur. J. Pharm. Sci.* **63**, 124–131 (2014).
82. Chadwick, K. *et al.* Cocrystallization: A Solution Chemistry Perspective and the Case of Benzophenone and Diphenylamine. *Cryst. Growth Des.* **9**, 1990–1999 (2009).

83. Boyd, S., Back, K., Chadwick, K., Davey, R. J. & Seaton, C. C. Solubility, metastable zone width measurement and crystal growth of the 1:1 benzoic acid/isonicotinamide cocrystal in solutions of variable stoichiometry. *J. Pharm. Sci.* **99**, 3779–3786 (2010).

84. Balawejder, M. *et al.* Multi-stage crystallization for resolution of enantiomeric mixtures in a solid solution forming system. *Chem. Eng. Sci.* **66**, 5638–5647 (2011).

85. Thati, J., Nordström, F. L. & Rasmuson, Å. C. Solubility of Benzoic Acid in Pure Solvents and Binary Mixtures. *J. Chem. Eng. Data* **55**, 5124–5127 (2010).

86. Friščić, T. & Jones, W. Recent Advances in Understanding the Mechanism of Cocrystal Formation via Grinding. *Cryst. Growth Des.* **9**, 1621–1637 (2009).

87. Macfhionnghaile, P. *et al.* Effects of Ball-Milling and Cryomilling on Sulfamerazine Polymorphs: A Quantitative Study. *J. Pharm. Sci.* **103**, 1766–1778 (2014).

88. Hasa, D., Carlino, E. & Jones, W. Polymer-Assisted Grinding, a Versatile Method for Polymorph Control of Cocrystallization. *Cryst. Growth Des.* **16**, 1772–1779 (2016).

89. Rehder, S., Christensen, N. P. A., Rantanen, J., Rades, T. & Leopold, C. S. High-shear granulation as a manufacturing method for cocrystal granules. *Eur. J. Pharm. Biopharm.* **85**, 1019–1030 (2013).

90. Moradiya, H. G. *et al.* Continuous cocrystallisation of carbamazepine and trans-cinnamic acid via melt extrusion processing. *CrystEngComm* **16**, 3573 (2014).

91. Wittering, K., King, J., Thomas, L. & Wilson, C. From Evaporative to Cooling Crystallisation: An Initial Co-Crystallisation Study of Cytosine and Its Fluorinated Derivative with 4-chloro-3,5-dinitrobenzoic Acid. *Crystals* **4**, 123–140 (2014).
92. Lee, M.-J. *et al.* Understanding the Formation of Indomethacin–Saccharin Cocrystals by Anti-Solvent Crystallization. *Cryst. Growth Des.* **13**, 2067–2074 (2013).
93. Rodríguez-Hornedo, N., Nehm, S. J., Seefeldt, K. F., Pagán-Torres, Y. & Falkiewicz, C. J. Reaction Crystallization of Pharmaceutical Molecular Complexes. *Mol. Pharm.* **3**, 362–367 (2006).
94. Zhao, L. *et al.* From discovery to scale-up: α-lipoic acid : nicotinamide co-crystals in a continuous oscillatory baffled crystalliser. *CrystEngComm* **16**, 5769 (2014).
95. Powell, K. A. *et al.* Toward Continuous Crystallization of Urea-Barbituric Acid: A Polymorphic Co-Crystal System. *Cryst. Growth Des.* **15**, 4821–4836 (2015).
96. Alvarez, A. J. & Myerson, A. S. Continuous Plug Flow Crystallization of Pharmaceutical Compounds. *Cryst. Growth Des.* **10**, 2219–2228 (2010).
97. Brown, C. J., Adelakun, J. A. & Ni, X. Characterization and modelling of antisolvent crystallization of salicylic acid in a continuous oscillatory baffled crystallizer. *Chem. Eng. Process. Process Intensif.* **97**, 180–186 (2015).
98. Ferguson, S., Morris, G., Hao, H., Barrett, M. & Glennon, B. Characterization of the anti-solvent batch, plug flow and MSMPR crystallization of benzoic acid. *Chem. Eng. Sci.* **104**, 44–54 (2013).

99. Lindenberg, C., Schöll, J., Vicum, L., Mazzotti, M. & Brozio, J. Experimental characterization and multi-scale modeling of mixing in static mixers. *Chem. Eng. Sci.* **63**, 4135–4149 (2008).

100. Bałdyga, J., Makowski, ł. & Orciuch, W. Double-Feed Semibatch Precipitation Effects of Mixing. *Chem. Eng. Res. Des.* **85**, 745–752 (2007).

101. Leyssens, T., Springuel, G., Montis, R., Candoni, N. & Veesler, S. Importance of Solvent Selection for Stoichiometrically Diverse Cocrystal Systems: Caffeine/Maleic Acid 1:1 and 2:1 Cocrystals. *Cryst. Growth Des.* **12**, 1520–1530 (2012).

102. Munshi, T., Redha, B., Feeder, N., Meenan, P. & Blagden, N. Impact of Mixed Solvent on Co-Crystal Solubility, Ternary Phase Diagram, and Crystallization Scale Up. *Cryst. Growth Des.* **16**, 1817–1823 (2016).

103. Redha, B. H. Impact of mixed solvent on co-crystal solubility, ternary diagrams and crystallisation scale-up. Crystallisations of Isonicotinamide?` Benzoic Acid Co-crystals from Ethanol?` Water Co-solvent System. (University of Bradford, 2013).

104. Al Nasser, W. N., Pitt, K., Hounslow, M. J. & Salman, A. D. Monitoring of aggregation and scaling of calcium carbonate in the presence of ultrasound irradiation using focused beam reflectance measurement. *Powder Technol.* **238**, 151–160 (2013).

105. Buanz, A. *et al.* Thermal Behavior of Benzoic Acid/Isonicotinamide Binary Cocrystals. *Cryst. Growth Des.* **15**, 3249–3256 (2015).

106. Kobayashi, H. *et al.* Changes in the structure and physical properties of the solid solution LiNi1−xMnxO2 with variation in its composition. *J. Mater. Chem.* **13**, 590–595 (2003).

107. Chung, I., Lee, B., He, J., Chang, R. P. H. & Kanatzidis, M. G. All-solid-state dye-sensitized solar cells with high efficiency. *Nature* **485**, 486 (2012).

108. Patel, M. A., AbouGhaly, M. H. H. & Chadwick, K. The discovery and investigation of a crystalline solid solution of an active pharmaceutical ingredient. *Int. J. Pharm.* **532**, 166–176 (2017).

109. Descamps, G. *et al.* Structural and Physicochemical Characterization of a Solid Solution Produced by Antisolvent Crystallization of a New Phosphoantigen. *Cryst. Growth Des.* **9**, 3910–3917 (2009).

110. Dittrich, B., Pfitzenreuter, S. & Hübschle, C. B. On QM/MM and MO/MO cluster calculations of all-atom anisotropic displacement parameters for molecules in crystal structures. *Acta Crystallogr. A* **68**, 110–116 (2012).

111. Funnell, N. P., Dawson, A., Marshall, W. G. & Parsons, S. Destabilisation of hydrogen bonding and the phase stability of aniline at high pressure. *CrystEngComm* **15**, 1047–1060 (2013).

112. Johnstone, R. D. L. *et al.* High-pressure polymorphism in L-serine monohydrate: identification of driving forces in high pressure phase transitions and possible implications for pressure-induced protein denaturation. *CrystEngComm* **10**, 1758 (2008).

113. Abagaro, B. T. O. *et al.* High pressure Raman scattering of dl-leucine crystals. *Vib. Spectrosc.* **66**, 119–122 (2013).

114. Minkov, V. S., Boldyreva, E. V., Drebushchak, T. N. & Görbitz, C. H. Stabilizing structures of cysteine-containing crystals with respect to variations of temperature and pressure by immobilizing amino acid side chains. *CrystEngComm* **14**, 5943 (2012).

115. Paukov, I. E., Kovalevskaya, Y. A. & Boldyreva, E. V. Low-temperature heat capacity and thermodynamic parameters of γ-aminobutyric acid. *J. Therm. Anal. Calorim.* **111**, 2059–2062 (2013).

116. Trabattoni, S., Moret, M., Campione, M., Raimondo, L. & Sassella, A. Epitaxial Growth of Organic Semiconductor Polymorphs on Natural Amino Acid Single Crystals. *Cryst. Growth Des.* **13**, 4268–4278 (2013).

117. Allen, F. H. The Cambridge Structural Database: a quarter of a million crystal structures and rising. *Acta Crystallogr. B* **58**, 380–388 (2002).

118. Görbitz, C. H. Crystal structures of amino acids: from bond lengths in glycine to metal complexes and high-pressure polymorphs. *Crystallogr. Rev.* **21**, 160–212 (2015).

119. Görbitz, C. H. Nanotubes of L -isoleucyl- L -leucine 0.91-hydrate. *Acta Crystallogr. Sect. E Struct. Rep. Online* **60**, o626–o628 (2004).

120. Soldatov, D. V., Moudrakovski, I. L., Grachev, E. V. & Ripmeester, J. A. Micropores in Crystalline Dipeptides as Seen from the Crystal Structure, He Pycnometry, and ^{129} Xe NMR Spectroscopy. *J. Am. Chem. Soc.* **128**, 6737–6744 (2006).

121. Henrik Görbitz, C. Nanotubes from hydrophobic dipeptides: pore size regulation through side chain substitution. *New J Chem* **27**, 1789–1793 (2003).

122. Dalhus, B. & Görbitz, C. H. Structural relationships in crystals accommodating different stereoisomers of 2-amino-3-methylpentanoic acid. *Acta Crystallogr. B* **56**, 720–727 (2000).

123. Dalhus, B. & Görbitz, C. H. Molecular aggregation in crystalline 1:1 complexes of hydrophobic D - and L -amino acids. I. The L -isoleucine series. *Acta Crystallogr. B* **55**, 424–431 (1999).

124. Dalhus, B. & Görbitz, C. H. Molecular aggregation in selected crystalline 1:1 complexes of hydrophobic D - and L -amino acids. III. The L -leucine and L -valine series. *Acta Crystallogr. C* **55**, 1547–1555 (1999).

125. Fábián, L., Chisholm, J. A., Galek, P. T. A., Motherwell, W. D. S. & Feeder, N. Hydrogen-bond motifs in the crystals of hydrophobic amino acids. *Acta Crystallogr. B* **64**, 504–514 (2008).

126. Kamei, T. *et al.* Solid−Liquid Equilibria in an L -Isoleucine + L -Alanine + Water System. *J. Chem. Eng. Data* **53**, 2801–2806 (2008).

127. Kamei, T. *et al.* Solid−Liquid Equilibria in an L -Isoleucine + L -Norleucine + Water System. *J. Chem. Eng. Data* **53**, 1338–1341 (2008).

128. Koolman, H. C. & Rousseau, R. W. Effects of isomorphic compounds on the purity and morphology of L-isoleucine crystals. *AIChE J.* **42**, 147–153 (1996).

129. Kurosawa, I., Teja, A. S. & Rousseau, R. W. Solid–liquid equilibria in l-leucine + l-valine + water&. *Fluid Phase Equilibria* 5 (2005).

130. Isakov, A. I., Kotelnikova, E. N., Muenzberg, S., Bocharov, S. N. & Lorenz, H. Solid Phases in the System L -Valine— L -Isoleucine. *Cryst. Growth Des.* **16**, 2653–2661 (2016).

131. Needham, T. E., Jr, Paruta, A. N. & Gerraughty, R. J. Solubility of Amino Acids in Pure Solvent Systems. *J. Pharm. Sci.* **60**, 565–567 (1971).

132. Kurosawa, I., Teja, A. S. & Rousseau, R. W. Solid–liquid equilibria in l-leucine + l-valine + water. *Fluid Phase Equilibria* **224**, 245–249 (2005).

133. Kurosawa, I. Solid-Liquid Equilibrium in multi solute systems. (2004).

134. Ferreira, L. A., Pinho, S. P. & Macedo, E. A. Solubility of l-serine, l-threonine and l-isoleucine in aqueous aliphatic alcohol solutions. *Fluid Phase Equilibria* **270**, 1–9 (2008).

135. Orella, C. J. & Kirwan, D. J. Correlation of amino acid solubilities in aqueous aliphatic alcohol solutions. *Ind. Eng. Chem. Res.* **30**, 1040–1045 (1991).

136. Needham, T. E. The Solubility of Amino Acids in Various Solvent Systems. 95

137. Collected via the I19 Rapid access service at Diamond Light Source (Project MT7150).

138. Coles, S. J. & Gale, P. A. Changing and challenging times for service crystallography. *Chem Sci* **3**, 683–689 (2012).

139. Cosier, J. & Glazer, A. M. A nitrogen-gas-stream cryostat for general X-ray diffraction studies. *J. Appl. Crystallogr.* **19**, 105–107 (1986).

140. Sheldrick, G. M. Sadabs. *Univ. Gött. Ger.* (1996).

141. Blessing, R. H. An empirical correction for absorption anisotropy. *Acta Crystallogr. A* **51**, 33–38 (1995).

142. Altomare, A., Cascarano, G., Giacovazzo, C. & Guagliardi, A. Completion and refinement of crystal structures with *SIR* 92. *J. Appl. Crystallogr.* **26**, 343–350 (1993).

143. Betteridge, P. W., Carruthers, J. R., Cooper, R. I., Prout, K. & Watkin, D. J. *CRYSTALS* version 12: software for guided crystal structure analysis. *J. Appl. Crystallogr.* **36**, 1487–1487 (2003).

144. Tang, C. C., Thompson, S. P., Hill, T. P. & Wilkin, G. R. Design of powder diffraction beamline (BL-I11) at Diamond. 6 (2007).

145. Thompson, S. P. *et al.* Beamline I11 at Diamond: A new instrument for high resolution powder diffraction. *Rev. Sci. Instrum.* **80**, 075107 (2009).

146. Nowell, H., Barnett, S. A., Christensen, K. E., Teat, S. J. & Allan, D. R. I19, the small-molecule single-crystal diffraction beamline at Diamond Light Source. *J. Synchrotron Radiat.* **19**, 435–441 (2012).

147. Görbitz, C. H. & Dalhus, B. Redetermination of L-Leucine at 120K. *Acta Crystallogr. C* **52**, 1754–1756 (1996).

148. Görbitz, C. H. & Dalhus, B. L-Isoleucine, Redetermination at 120K. *Acta Crystallogr. C* **52**, 1464–1466 (1996).

149. Dalhus, B. & Görbitz, C. H. Crystal structures of hydrophobic amino acids 1. redeterminations of L-methionine and L-valine at 120 K. *Acta Chem. Scand.* **50**, 544–548 (1996).

150. Coll, M., Solans, X., Font-Altaba, M. & Subirana, J. A. Structure of \sc l-leucine: a redetermination. *Acta Crystallogr. Sect. C* **42**, 599–601 (1986).